INFORMATION TO USERS

This manuscript has been reproduced from the microfilm master. UMI films the text directly from the original or copy submitted. Thus, some thesis and dissertation copies are in typewriter face, while others may be from any type of computer printer.

The quality of this reproduction is dependent upon the quality of the copy submitted. Broken or indistinct print, colored or poor quality illustrations and photographs, print bleedthrough, substandard margins, and improper alignment can adversely affect reproduction.

In the unlikely event that the author did not send UMI a complete manuscript and there are missing pages, these will be noted. Also, if unauthorized copyright material had to be removed, a note will indicate the deletion.

Oversize materials (e.g., maps, drawings, charts) are reproduced by sectioning the original, beginning at the upper left-hand corner and continuing from left to right in equal sections with small overlaps.

Photographs included in the original manuscript have been reproduced xerographically in this copy. Higher quality 6" x 9" black and white photographic prints are available for any photographs or illustrations appearing in this copy for an additional charge. Contact UMI directly to order.

ProQuest Information and Learning
300 North Zeeb Road, Ann Arbor, MI 48106-1346 USA
800-521-0600

UMI®

UNIVERSITY of CALIFORNIA
SANTA BARBARA

Terahertz Electro-Optics of Excitonic Intersubband Excitations in Double Quantum Wells

A dissertation submitted in partial satisfaction of the
requirements for the degree of

Doctor of Philosophy

in

Physics

by

Mark Y. Su

Committee in charge:

Professor Mark Sherwin, Chair
Professor David Awschalom
Professor Horia Metiu

September 2001

Bell & Howell Information and Learning Company
300 North Zeeb Road
P.O. Box 1346
Ann Arbor, MI 48106-1346

The dissertation of Mark Y. Su is approved:

Chair

September 2001

Terahertz Electro-Optics of Excitonic Intersubband Excitations in Double Quantum Wells

For Ralph Bunday,

my high school physics teacher.

Acknowledgements

Dave Enyeart, **Dean White**, and **Jerry Ramian** for running and tuning the best FEL in the world. **Jack Whaley** and **Bob Hill** for running an amazing research cleanroom. **Mike Wroklage** and **Rudi Stuber** for running an amazing machine shop, and for invaluable help in machining and cryogenic design. **Sam Carter** for his enthusiastic help in the last year's mega-push to wrap this beast up. **Jun Kono** for his infectious hard-core enthusiasm and drive, and for supporting my ideas early in my graduate research career. **Dan Schmidt** for his sound experimental advice, cool lab to hang out in, and solid belay. **Mark Sherwin** for his unflagging enthusiasm for the physics, and for giving me intellectual freedom. **Jim Allen** for his depth of semiconductor knowledge, constant willingness to help out, and for making the Applied Physics Seminar the best talk in town.

Curriculum Vitæ

Mark Y. Su

Personal

[Born] May 2, 1973 Columbus, Ohio

Education

[1991–1995] University of Rochester, Rochester NY

B.S. Physics

B.A. Mathematics

Publications

Direct and indirect tunnelling of excitons in tilted double quantum wells M.Y. Su, S. Carter, A. Huntington, C. Kadow, L.A. Coldren, A.C. Gossard, M.S. Sherwin, in preparation.

Voltage-tunable terahertz electro-optic modulation by excitonic intersubband excitation M.Y. Su, S. Carter, A. Huntington, C. Kadow, L.A. Coldren, A.C. Gossard, M.S. Sherwin, in preparation, Sep. 2001.

Nonperturbative Terahertz Nonlinear Optics of Double Quantum Well Excitons M.Y. Su, S. Carter, A. Huntington, C. Kadow, L.A. Coldren, A.C. Gossard, M.S. Sherwin, in preparation, Sep. 2001.

Odd terahertz optical sidebands from asymmetric excitonic intersubband excitation M.Y. Su, C. Phillips, J. Ko, L. Coldren, M.S. Sherwin, Physica B, v. 272, p. 438 1999.

Generation of First-Order Terahertz Optical Sidebands in Asymmetric Coupled Quantum Wells C. Phillips, M.Y. Su, M.S. Sherwin, J. Ko, L. Coldren, Applied

Physics Letters v. 75, p.2728 Nov. 1, 1999.

Coherent terahertz mixing spectroscopy of asymmetric quantum well intersubband transitions M.Y. Su, C. Phillips, C. Kadow, J. Ko, L.A. Coldren, A.C. Gossard, M.S. Sherwin, Proceedings of the SPIE (Terahertz Spectroscopy and Applications) vol. 3617, p.106 1999.

Resonant Terahertz Optical Sideband Generation from Confined Magnetoexcitons J. Kono, M.Y. Su, T. Inoshita, T. Noda, M.S. Sherwin, S.J. Allen, Jr., H. Sakaki, Physical Review Letters v. 79, p. 1758 Sep. 1, 1997.

Abstract

Terahertz Electro-Optics of
Excitonic Intersubband Excitations
in Double Quantum Wells

by

Mark Y. Su

In experiments using the UCSB Free Electron Lasers (FEL), I studied how intense terahertz (THz) electric fields modulate the interband refractive index in gated, undoped, GaAs/AlGaAs double quantum wells (DQW) subject to an applied DC voltage. The DQW structures were designed to have tunnel-split energy levels in the THz frequency range. When the THz field resonantly couples to an intersubband excitation of excitons confined to the wells, a weak near-infrared (NIR) probe beam is modulated at THz frequencies. This results in the emission of optical sidebands which appear at frequencies $\omega_{sideband} = \omega_{NIR} + n\omega_{THz}$ where ω_{NIR} (ω_{THz}) is the frequency of the NIR (THz) beam and $n = 1, 2, \ldots$.

The *excitonic* intersubband excitations studied here are distinct from the well-known intersubband transitions of electrons in a doped quantum well. The Coulomb interaction between electron and hole drastically modifies the single-particle states and their dipole moments. In particular, the excitonic states in an undoped DQW are both direct (electron and hole on the same side of the tunnel barrier) and indirect (electron and hole on opposite sides of the tunnel barrier). A DC voltage applied to the gates tunes indirect excitons into tunnel resonance with direct excitons.

During THz modulation, the terahertz field couples between tunnel-split exciton states. At low terahertz intensities, the sideband intensity as a function of gate bias,

ω_{NIR}, and ω_{THz} was measured and modelled by a nonlinear susceptibility $\chi^{(2)}$ for three-wave mixing between THz and NIR fields.

At high terahertz intensities, the electric dipole energy is comparable to the photon energy. The sideband intensity displayed an unusual non-monotonic dependence on the THz field strength. In this strong-field regime, the oscillating refractive index may be understood by the formation of *Floquet states*, which oscillate with the same periodicity as the driving terahertz field.

Contents

List of Figures

List of Tables

Chapter 1

Introduction

1.1 A terahertz gap

The past few decades of advances in solid-state physics has resulted in a huge array of compact and inexpensive electronic devices that work at very high frequencies. Indeed, the astonishing validity of Moore's Law continues to be a driving principle in the semiconductor industry. As of this writing I can buy a laptop computer with a microprocessor running 1.5 GHz, plugged into a wireless modem operating at tens of GHz.

At the same time advances in photonics has resulted in optically networking these fast electronic devices. The laptop I mentioned can be connected to an internet backbone with hundreds of gigabits/s of cheap bandwidth, thanks to the advent of semiconductor lasers, amplifiers, and modulators sending optical signals down nearly dispersion-free optical fibers.

Laser physics has been progressing at a fabulous rate as well, especially nonlinear oscillators driven by that trusty workhorse of optical physics, the Ti:Sapphire laser. It is possible to purchase turnkey, tabletop sources of coherent light tunable from ultraviolet all the way down to mid-infrared. The basic physics made accessible by these technologies directly feeds back to generate new technologies.

Meanwhile, at of the turn of the century, the availability of useful devices that operate in the region of the electromagnetic spectrum between 500 GHz and 10 THz is abysmal.

The practical problem comes from two directions.

Firstly, electronic techniques rapidly roll off at these super-high frequencies, as semiconductor electron relaxation rates are approached and parasitics dominate the behavior of electronic devices.

Secondly, photonic techniques fail at these low frequencies, partly because relative linewidths which are narrow in the optical part of the spectrum become huge down in the THz. Solid state systems also bear many resonances in this region which render most materials opaque to THz radiation.

Stuck between the divide between high-frequency electronics and mm-wave photonics, terahertz is the runt of the technology litter.

1.2 Optical switching and other wish-lists

The motivations for the current push to beef up terahertz technologies range from pure science to pure commerce. Cosmologists wish to spatially and spectrally resolve the THz radiation emanating from distant dust-enshrouded early galaxies. Atmospheric chemists wish to spectroscopically monitor airborne pollutants whose molecular vibrational modes lie in the THz range.

An application particularly addressed by this dissertation is in the field of optical networking. Network engineers want to be able to fully utilize the 50 THz of low-loss bandwidth in optical fiber. To do so, traffic is wavelength-division multiplexed (WDM) with separate wavelengths for separate channels (Fig 1.1). A basic

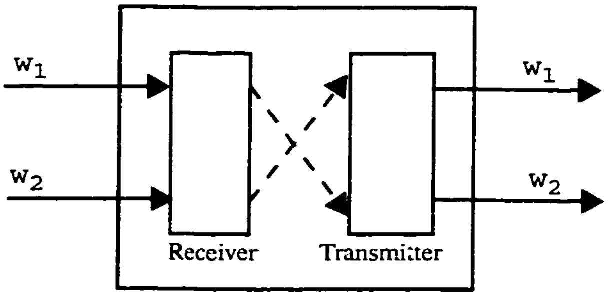

Opto-electronic switch

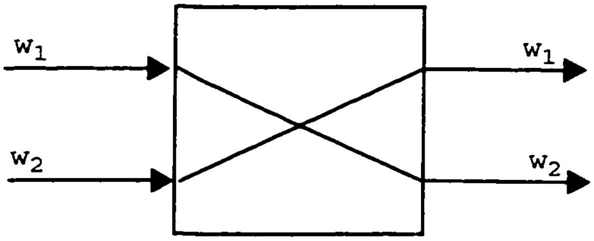

All-optical (electro-optic) switch

Figure 1.1: In a wavelength division multiplexed (WDM) optical communications network, two channels may be separated by up to $\Delta f \approx 2Bn + 6B(n-1)$ GHz where B is the individual channel bit rate in bits/s (bps), and n is the total number of channels[1]. The factor of 2 assumes a modulation efficiency of 2 Hz/bps. The factor of 6 is the conventional spacing to minimize crosstalk. For $B = 10Gbps$ and $n = 20$,$\Delta f = 1.5$ THz. TOP: Switching between channels currently requires demodulation of the optical signal to an electrical one, and then a remodulation on the new wavelength channel. BOTTOM: the widely sought-after goal of all-optical wavelength shifting requires modulating a NIR carrier at THz frequencies.

WDM network function is to convert the data coming in on one channel to a different channel in order to forward it onto the next node[1]. A holy grail within the optical networking community is to be able to perform the wavelength conversion all-optically; that is, to not have to decode the optical signal into an electronic signal and resend it on the new wavelength channel. All-optical switching in a WDM requires shifting the frequency of a NIR carrier to another frequency separated by the order of a few THz. This application requires the ability to modulate a NIR carrier beam at THz frequencies, a process which generates an optical sideband at the new frequency. The sideband can subsequently be amplified and sent on its way.

1.3 Terahertz electro-optics in double quantum wells

The advent of semiconductor heterostructures paved the way for practical terahertz photonic devices, since the electronic band structure can be tuned through careful epitaxial crystal growth and the application of external electric and magnetic fields. Semiconductor quantum wells can be engineered to have narrow electronic intersubband resonances in the THz regime. Double quantum wells (DQW), in which two quantum wells are separated by a thin tunnel barrier, are particularly attractive in this regard for several reasons: the optical band-gap can be tuned by the width of the individual wells while the THz resonance can be separately tuned by the dimensions of the tunnel barrier (Fig. 1.2). Furthermore, large optical nonlinearities can be engineered[3] into the DQW by making the two wells different widths, creating an asymmetric DQW (ADQW, see Fig. 1.3). The nonlinearities arise because the electrons feel a non-centrosymmetric confinement potential.

This dissertation will describe THz electro-optic experiments in which a NIR probe laser beam is modulated at THz frequencies in asymmetric double quantum wells. The THz field couples to an *intersubband* excitation while the NIR field

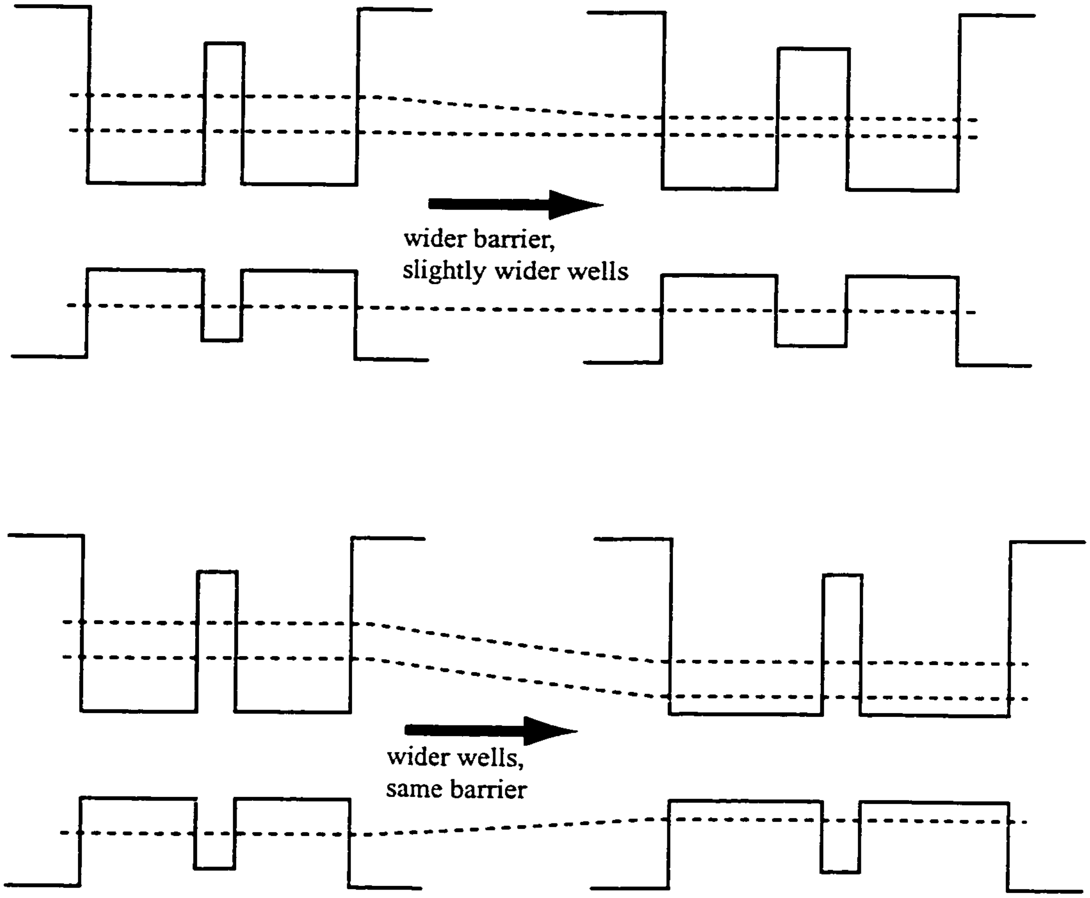

Figure 1.2: Double quantum well (DQW) structure allows one to tune the intersubband spacing and the interband spacing by varying the tunnel barrier and well width independently. The intersubband spacing can be designed to lie in the THz regime, while the interband spacing in GaAs systems is in the NIR.

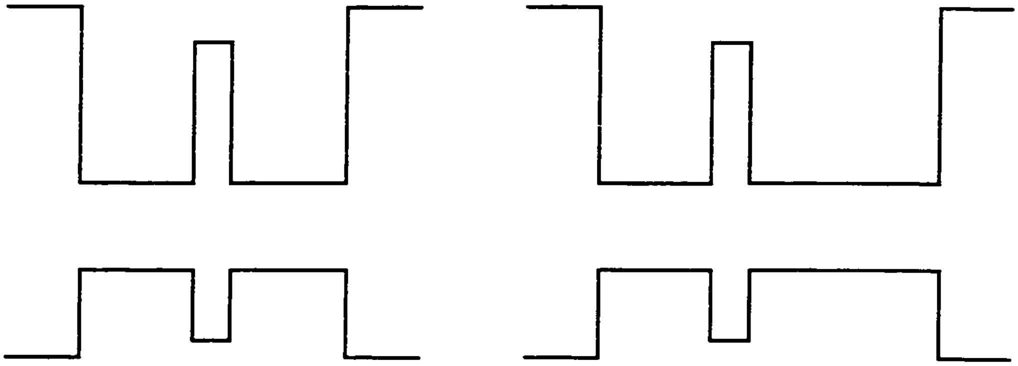

Figure 1.3: LEFT: Symmetric DQW has no second-order nonlinearities. RIGHT: Asymmetric DQW can have extremely large THz second-order optical nonlinearities.

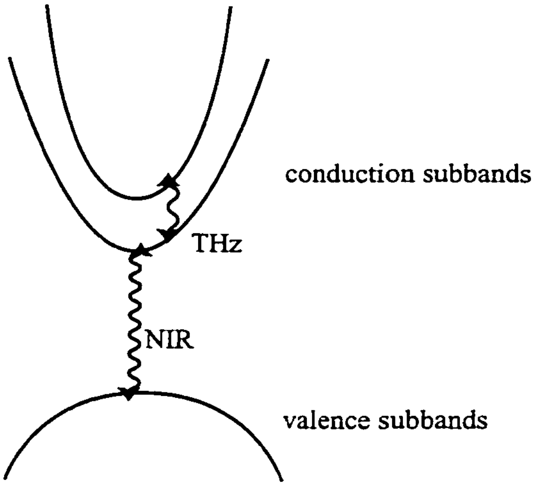

Figure 1.4: The THz field couples to an *intersubband* excitation, while the NIR field couples to an *interband* excitation.

couples to an *interband* excitation (Fig. 1.4). When certain resonance conditions are met the NIR probe is modulated resulting in the emission of optical sidebands which appear at frequencies

$$\omega_{sideband} = \omega_{NIR} + n\omega_{THz} \tag{1.3.1}$$

where ω_{NIR} (ω_{THz}) is the frequency of the NIR (THz) beam and $n = \pm 1, 2, \ldots$ (Fig. 1.5).

The optically active ADQW region was sandwiched between two gates. Applying a DC voltage to the gates tunes the active region into resonances with the THz and NIR beams. I studied in detail the strength of the $n = +1$ sideband (hereafter referred to as "the sideband") as a function of gate bias, NIR frequency, THz frequency, and THz field strength.

1.4 Strong-field physics

A major basic physics perk for studying the THz field strength dependence of sideband generation in quantum wells is the chance to experimentally probe the effect of a very strong resonant laser field on a quantum system. By "very strong" I mean that the electric dipole energy, or *Rabi* energy $\mu \cdot E$ is comparable to the photon energy $\hbar\omega$:

$$\frac{\mu \cdot E}{\hbar\omega} \geq 1 \tag{1.4.1}$$

Where μ is the dipole moment, E is the electric field strength, and ω is the radiation frequency. This is the *strong-field* regime.

At optical frequencies $\hbar\omega$ is very high so it is generally hard to satisfy (1.4.1). Previous studies into this regime have looked at atoms in microwave cavities[4, 5]. The atoms are prepared in excited states where the level separation is in the microwave range. Since atomic excited states are near the continuum, strong-field ef-

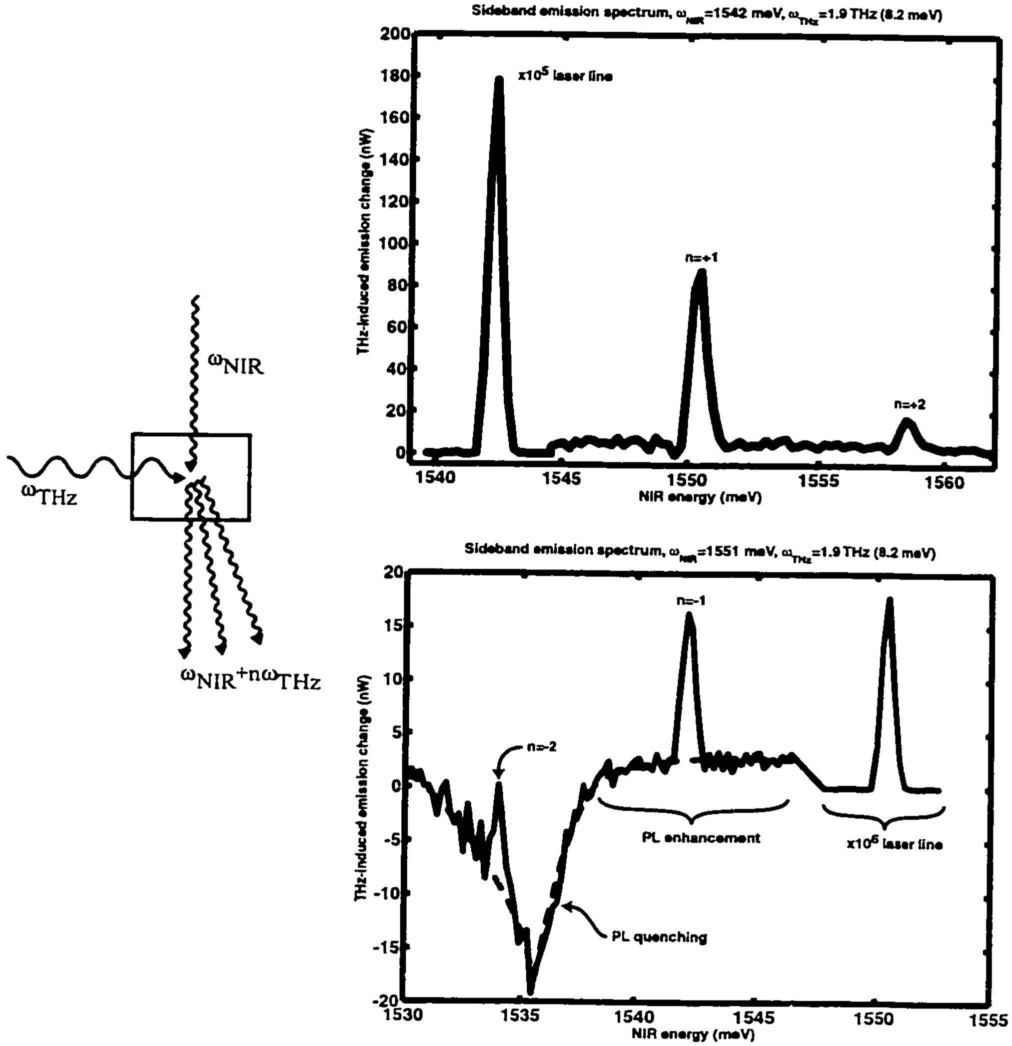

Figure 1.5: THz modulation of a NIR probe generates THz optical sidebands on the probe beam. In this dissertation the terms "modulation","sideband generation", and "mixing" will be used interchangeably.

fects manifest themselves as unexpected ionization rates as a function of microwave field strength. There exist beautiful and profound links between the ionization rates in the atomic system and the stability of KAM tori in the analogous chaotic classical system.

However, the atoms are ionized, meaning the bound states don't exist anymore after the microwave field is turned on! This is an inescapable consequence of the distribution of level spacings in an atom. The upper states get closer and closer together, so ionization is inevitable when resonantly driving upper states at microwave frequencies (Fig. 1.6).

There is a rich body of theoretical predictions on the effect of strong fields on the *bound* states of a quantum system[6, 7]. In quantum wells, upper states get farther and farther apart. Thus (1.4.1) can be satisfied by resonantly driving the lowest subbands of a quantum well at THz frequencies. Yet the well is still far deeper than the Rabi energy, so the bound states still survive.

The strong field effects on the bound quantum well states manifest themselves as unexpected sideband intensities as a function of THz field strength. There are technological consequences, as these effects place an upper-bound on the modulation efficiency in electro-optical devices.

1.5 Quantum well optical properties

This section reviews some key concepts of quantum well optical properties necessary to develop the rest of the dissertation. For more detail please refer to numerous excellent reviews on the subject[8, 9].

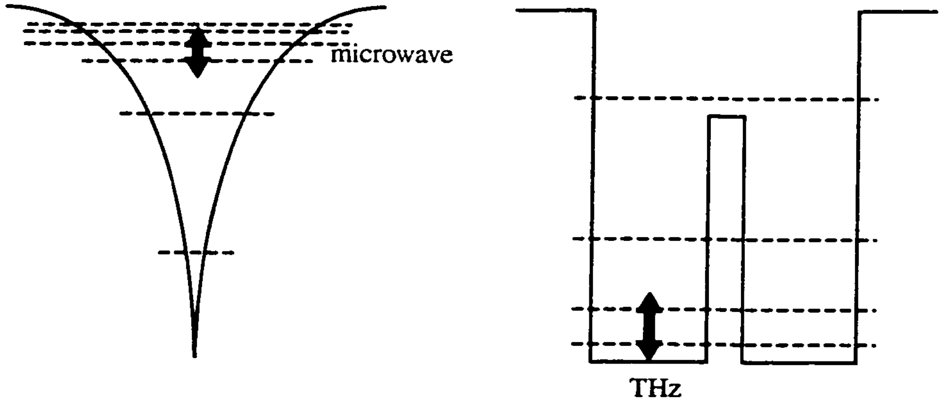

Figure 1.6: In atoms, the strong-field condition (1.4.1) can only be satisfied for excited states, which are near the continuum and easily ionized. In a QW, the excited states get farther apart, so even in a strong-field limit the bottom states stay bound.

1.5.1 Electron-hole states

Molecular-beam epitaxial crystal growth of alternating layers of GaAs and AlGaAs layers forms a semiconductor heterostructure with spatially varying bandgap profiles in the growth direction z. The bandgap profiles form a one-dimensional potential energy that an electron in the conduction band feels. Similarly, a hole in the valence band also feels a one-dimensional potential energy profile. The confinement potential in the z-direction leads to discrete energy levels. Within each energy level electrons and holes are free to move about in the xy plane. Therefore each quantum well energy level forms a *subband* of energies corresponding to the continuous spectrum of xy-plane k-vectors (Fig. 1.7a).

In the III-V family of semiconductors the valence band Bloch states are formed by hybridized atomic orbital states with p-symmetry ($l = 1$). Spin-orbit coupling splits the valence band into separate bands ($[J = 3/2, m_j = \pm 3/2]$, $[J = 3/2, m_j = \pm 1/2]$, $[J = 1/2]$) with different effective masses given by the curvature of the hole

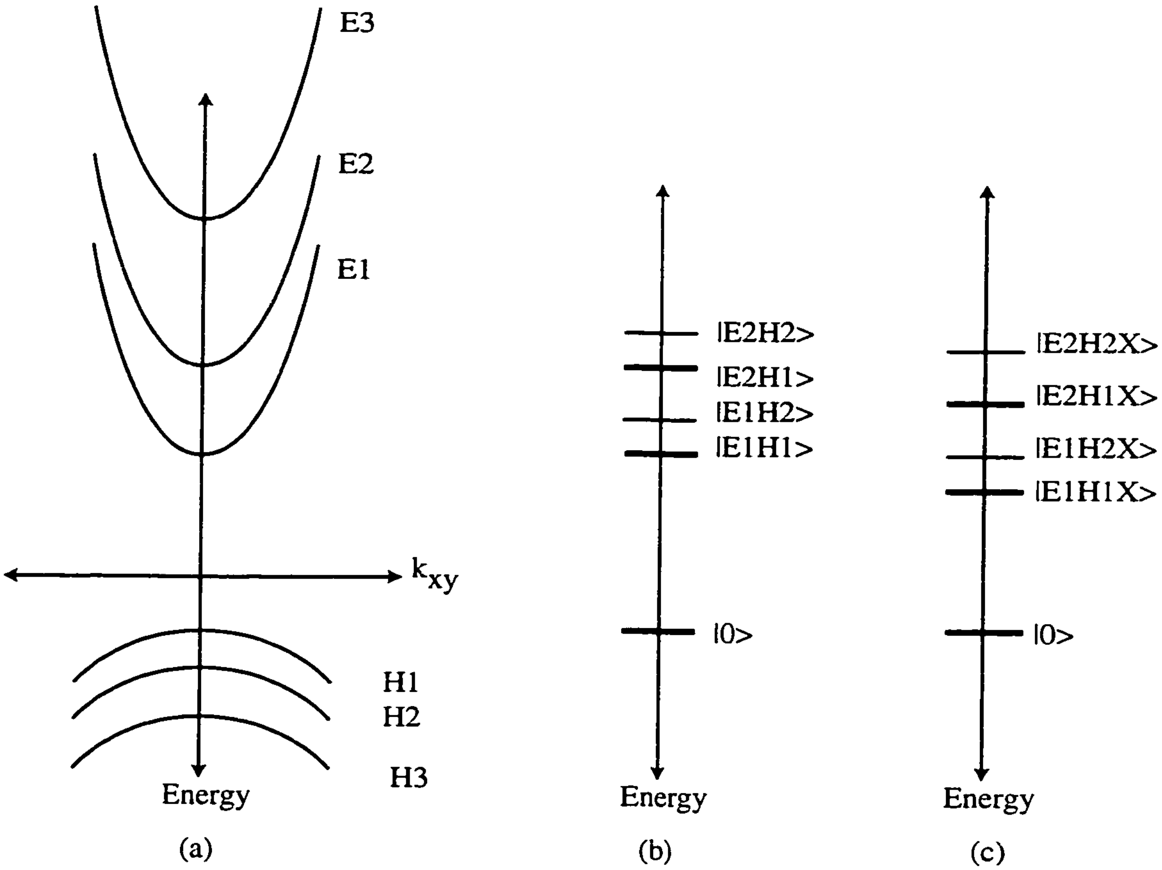

Figure 1.7: (a) xy-plane dispersion of electron (E_m) and hole (H_n) subbands. (b) $k_{xy} = 0$ energies of free electron-hole continuum subband E_mH_n. $|0\rangle$ is the vacuum ground state with no electrons or holes. A NIR photon couples the vacuum to an electron-hole state. A THz photon couples between electron-hole subbands. (c) Energies of the $1s$ exciton associated with each free electron hole subband. The binding energy makes the exciton lower in energy than its associated free electron hole continuum. Again, a NIR photon couples the vacuum to an exciton, while a THz photon couples between excitons states.

carrier	z mass	xy mass
electron	0.067	0.067
heavy-hole	0.340	0.115
light-hole	0.094	0.206

Table 1.1: Carrier masses in GaAs in units of m_0, the electron mass. The hole masses are based on the Luttinger parameters γ_1 and γ_2 (see Sec. 3.2). From [2]

dispersion relation at $k = 0$. The two $J = 3/2$ bands are called heavy-holes and light holes.

Heavy-holes and light-holes confined in the same quantum-well potential will have different subband energies due to their different masses. For symmetry reasons a curious effect called *mass reversal* occurs in which a heavy hole in the z- direction will be a light hole in the xy plane, and vice-versa (see Table 1.1). Following standard usage, we always label the hole according to the hole's mass in the z-direction. In an undoped quantum-well the ground state of the crystal is the *vacuum* state with no electrons or holes. A NIR photon can create an electron in conduction subband m and a hole in valence subband n (Fig. 1.7b). These are the free-particle electron-hole (e-h) states since the carriers are unconfined in the xy plane. They are labeled E_mHH_n and E_mLH_n for heavy-holes and light-holes, respectively. The label E_mH_n will be used when generically referring to both heavy and light holes.

1.5.2 Excitons

Since electrons are negatively charged while holes are positive, they experience a Coulomb interaction. Thus the correct e-h states include the Coulomb bound states, called excitons (Fig. 1.7c). They form a Ryderg series of bound states $1s, 2s, 2p, \ldots$ leading up to the free-particle e-h states. The exciton binding energy Ry^* in GaAs/AlGaAs quantum wells is on the order of 5-10 meV, with a Bohr radius

$\approx 100A$.

Since the overlap of electron and hole is greater in an exciton state than a free state, the interband oscillator strength is much greater. In addition, as they are lower in energy than the free states, excitons dominate the photoluminescence (PL) spectrum.

In the case of quantum wells less than the Bohr radius, there will be an exciton series associated with each free-particle subband $\mathrm{E}_m\mathrm{H}_n$. Thus, the ground state exciton can be labelled $\mathrm{E}_m\mathrm{H}_n\mathrm{X}$, with the "X" to distinguish it from the free-particle subband.

A detailed calculation of the exciton states is in Chapter 3 in the analysis of PL spectra.

1.5.3 Intersubband transitions

Light polarized in the z-direction can couple between electron or hole subbands. In doped quantum wells the *intersubband* transition has been and continues to be studied extensively, forming the basis for quantum-well infrared photodetectors, quantum-cascade lasers, and harmonic generators.

In undoped systems z-polarized light can couple between exciton states. Intersubband work in undoped systems has been more limited. Ehrenfreund and coworkers[10, 11, 12] have induced absorption of z-polarized light in undoped quantum wells by photogenerating excitons with a second laser beam.

A detailed calculation of the excitonic intersubband resonance is in Chapter 4 in the analysis of sideband excitation spectra.

1.6 Terahertz electro-optics background

Even-numbered THz optical sidebands $\omega_{sideband} = \omega_{NIR} + n\omega_{THz}$ where $n = \pm 2, 4, \ldots$ in quantum wells were first discovered by Cerne and Kono when studying the change in GaAs/AlGaAs excitonic photoluminescence induced by a strong THz field[13, 14]. Kono and Su exploited the process as a useful spectroscopic tool for studying the internal energy levels of GaAs/AlGaAs quantum-well excitons in high magnetic fields[15]. The generation of the $n = 2$ sideband was enhanced when $\hbar\omega_{THz}$ was resonant with magnetically-tuned energy levels in the excitons, specifically between $1s$-$2p+$ and $2s$-$2p-$ states. Using traditional linear absorption methods is impossible for spectroscopy of very dilute ($n \approx 10^{10}$ cm^{-2}) exciton systems.

In InGaAs/GaAs quantum wells, Nordstrom studied the relationship between even-numbered sideband generation and a related THz electro-optic effect, the excitonic dynamical Franz-Keldysh effect, in which the free-electron hole subband edge is blue-shifted by the pondermotive energy of the THz field[16].

An effort was then made to generate the odd-numbered sidebands $\omega_{sideband} = \omega_{NIR} + n\omega_{THz}$ where $n = 1, 3, 5, \ldots$. The magneto-exciton experiments used THz electric fields which were polarized parallel to the quantum well plane, where the exciton Hamiltonians have inversion-symmetry. For an inversion-symmetric potential, only even-numbered sidebands can be generated.

Phillips and Su developed the basic experimental techniques for coupling both z-polarized THz radiation into the device, while simultaneously exciting and collecting xy-polarized NIR light[17, 18]. Both even and odd sidebands were generated by breaking inversion symmetry in a coupled quantum well structure and polarizing the THz electric field in the growth direction. Details of these techniques are described in Chap. 2.

It is interesting to note that THz electro-optic effects can also be used to generate and detect terahertz fields using all-optical laser pulses. Zhang and coworkers generate THz pulses in bulk ZnTe crystals, and detect them with a phase-sensitive electro-optic sampling method in a second ZnTe crystal[19]. The mirror process was recently performed by Heyman, generating THz optical sidebands in ZnTe[20].

Chapter 2

Experimental Methods

The experiments in this dissertation involved the design and crystal growth of samples, their processing into measurable devices, optical characterization, and THz electro-optic modulation measurements. Detailed information for workers to repeat the experiments are contained in Appendices.

2.1 Sample Design

The samples in this study were grown by molecular beam epitaxy (MBE) on semi-insulating GaAs substrates by Jack Ko, Andrew Huntington, and Christoph Kadow, all from the Electrical Engineering Department at UCSB.

Several generations of samples had to be grown, processed, and tested to fine-tune the parameters and process for a workable sample which was used for most of the measurements reported in this dissertation. The final generation of samples consisted of four functionally distinct regions:

1. Active region containing the double-quantum wells.

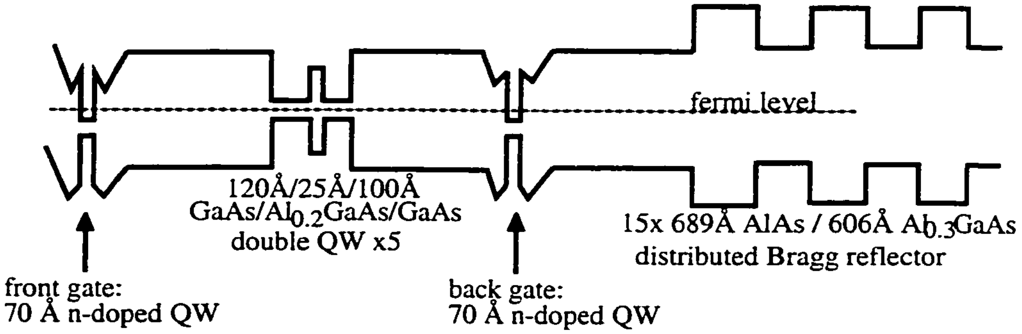

Figure 2.1: Sample band structure, containing frontgate, active region, backgate, and distributed Bragg reflector. Not to scale.

2. Distributed Bragg reflector for the NIR probe.
3. Backgate consisting of a narrow n-doped quantum-well.
4. Frontgate consisting of a narrow n-doped quantum-well.

The band diagram of the sample is shown in Fig. 2.1.

2.1.1 Active Region

The active region consisted 5 periods of double quantum well, each consisting of a 120 Å GaAs quantum well and a 100 Å GaAs quantum well separated by a 25 Å $Al_{0.2}Ga_{0.8}As$ tunnel barrier ($120/25 \times 0.2/100$). Each period is separated by a thick 300 Å $Al_{0.3}Ga_{0.7}As$ barrier so that neighboring DQWs are not interacting. I chose the number of periods to balance the need for more signal with the desire to keep the active region thin compared to the NIR wavelength. A thicker region would have more signal but is more difficult to model due to reabsorption, phase-matching, and screening effects.

The dimensions of the DQW were designed so that the two lowest-lying electron subbands were separated by ≈ 10 meV (≈ 2.4 THz) at flat-band. This is around the center of the range of high-quality operating frequencies of the THz source, the UCSB Free Electron Laser (FEL).

Within the 10 meV energy splitting constraint, the degree of asymmetry was designed to peak the strength of the sideband at flat-band conditions. If the asymmetry is too small, then the sideband is weak, and the tunnel barrier will be too thin to ensure consistent growth from well-to-well. If the asymmetry is a little too large, then the tunnel barrier will be too thick to couple the two wells.

2.1.2 Distributed Bragg reflector

A distributed Bragg reflector (DBR) is an stack of alternating high and low refractive index material with each period $1/4$-wavelength thick. It is simply a dielectric mirror. The passband, or region of high reflectivity, is determined by the index contrast between the high- and low-index material.

Directly grown into the sample by MBE, the DBR consisted of 15 periods of 689 Å AlAs and 606 Å $Al_{0.3}Ga_{0.7}As$. It had a low-temperature passband nearly centered on the low-temperature bandgap of the DQW, making it about 95% reflective for the NIR probe beam.

The DBR is necessary because the GaAs substrate is opaque to the NIR probe beam. In previous studies of even-numbered sidebands, I removed the substrate with a wet chemical etch. However in those cases the incident NIR and THz beams were collinear and polarized in the xy plane. To generate odd sidebands in these asymmetric quantum well systems it is necessary to polarize the THz field in the z-direction. However it is nearly impossible to efficiently couple z-polarized THz radiation into a sample consisting of only a free-standing epilayer. It is also difficult to process gates on substrate-free device.

2.1.3 Gates

To apply a DC electric field across the DQWs, the active region was sandwiched between two gates, a frontgate and a backgate. By applying a voltage between the frontgate and backgate I could tilt the DQW and voltage-tune the exciton states.

Each gate consisted of a 70 Å quantum well delta-doped with Si to create a high-mobility 2D electron gas with density $\approx 1\times10^{12}\,\mathrm{cm}^{-2}$. The gates are separated from the active region by 3000 Å $Al_{0.3}Ga_{0.7}As$ barriers. Since the gate quantum wells are narrow, their subband spacing is large and thus are both completely transparent to both the NIR probe and the THz field.

An ordinary metal Schottky frontgate would, of course, not have been transparent to the NIR probe. On some preliminary devices I evaporated nichrome semi-transparent Schottky gates. Their difficulty is twofold: they are lossy to both NIR and THz, and introduce a parasitic nonlinearity into the system since the the Schottky interface is a diode. However, for certain device geometries a semitransparent Schottky diode may be much easier to process, making it an option worth pursuing in the future.

Early generations of samples had the backgate *behind* the DBR. However, charge became trapped in the DBR, possibly in the X-valley conduction-band minima in the AlAs layers. Even with the backgate in front of the DBR it was necessary to separate the backgate from the DBR by at least 1000 Å, because the DBR acted as a great sponge for charge.

2.1.4 Other samples

I will also present some results from an earlier generation ungated DQW sample where the wells are more weakly coupled. It consisted of 25 periods of a 85 Å GaAs quantum well and a 75 Å GaAs quantum well separated by a 25 Å $Al_{0.3}Ga_{0.8}As$ tunnel barrier. I will refer to this sample as [85/25×0.3/75].

2.2 Device Fabrication

After MBE growth by collaborators, I processed the sample in the UCSB cleanroom facility. The purpose of processing is to isolate an active mesa, to make separate ohmic contacts to the front and back gates, and to facilitate efficient coupling of z-polarized THz radiation into the device.

The THz-coupling scheme largely determined the device geometry and process. Two coupling schemes led to two types of device geometry: a dielectric waveguide (Fig. 2.2) and an antenna-coupled device (Fig. 2.3).

The antenna-coupled devices suffered from signal-to-noise problems because of the small optical area of the mesas ($\approx 10\ \mu m^2$) and short integration times (see Sec 2.3). Thus the results presented in this disseration come from the waveguide-coupled devices. Details on the the antenna-coupled device processing and THz coupling are described in App. A.

All the metallization and etch patterns were defined using standard contact photolithography. First, I evaporated and annealed metal ohmic contacts to the frontgate. Then I defined a mesa with a combination dry- and wet- chemical etch. This is followed by evaporating and annealing a second set of ohmic contacts to the backgate.

To form the waveguide, the sample was then cleaved into a 1 mm wide strip, 8 mm long. I then cleaved a 400 μm-thick wafer of crystal sapphire substrate material

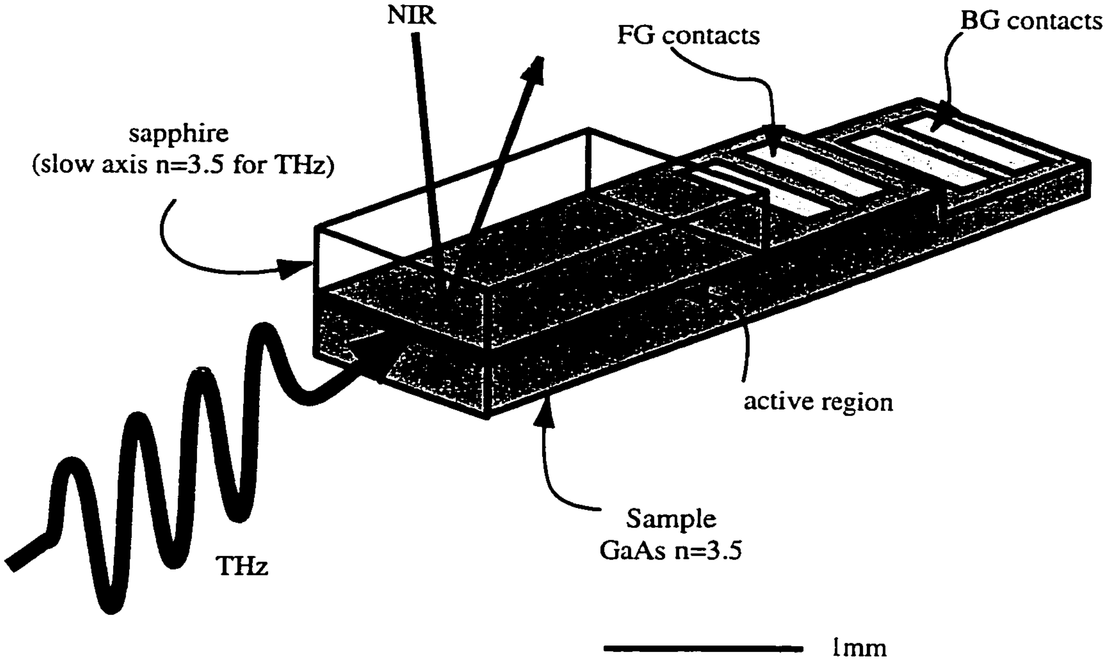

Figure 2.2: Processed waveguide device.

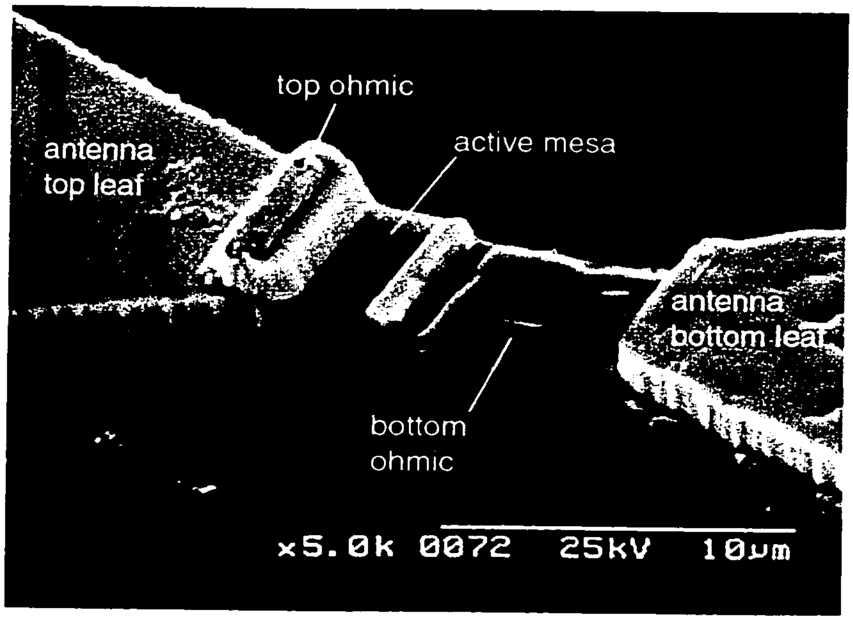

Figure 2.3: Antenna-coupled device with small active mesa in center. Antenna leafs extend for 500 μm. Details on device processing are in Appendix A.

into a 1×5 mm strip, oriented with the optically slow axis along the long dimension. The sapphire was mechanically pressed against the surface of the sample with a beryllium copper clip as shown in Fig. 2.2.

In the final process step the contacts are bonded by indium solder to Au wire.

At low temperature, sapphire is index-matched to GaAs and transparent at THz wavelengths. At the same time, sapphire is transparent to the NIR. Pressing the sapphire against the sample forms a rectangular dielectric waveguide with half of the waveguide defined by the sample substrate and the other half defined by the sapphire. The epilayer containing the active region lies in the middle of the waveguide.

Without the sapphire, the sample substrate itself forms the waveguide, with the active region next to the air interface. Thus, the THz field component polarized in the z-direction (that is, perpendicular to the interface) is very small. In fact, this is not a problem for measurements requiring low THz field intensities.

2.3 Measurement

This section describes the experimental setup, which is illustrated in Fig 2.4. Optical alignment procedure, detector electronics, and other sundry details are contained in App. B.

2.3.1 Cryostat and voltage bias

The device is mounted on the cold-finger of a closed-cycle cryostat and regulated at 21 K. The cleaved edge of the sample-sapphire waveguide devices stands free from the edge of the copper sample-mount.

The gate voltage is applied by a external voltage source via shielded twisted-pair cable.

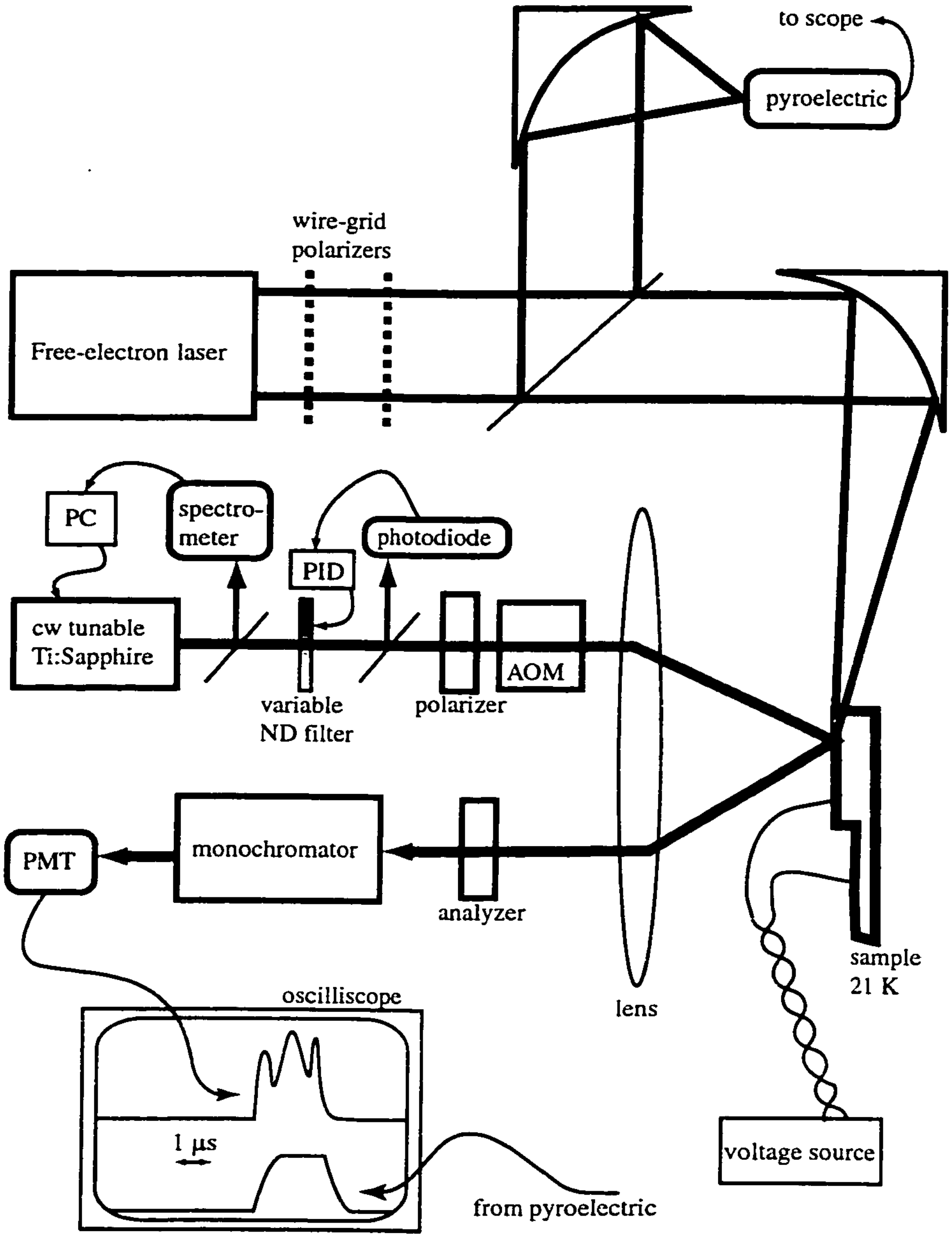

Figure 2.4: Experimental layout. The wiggles in the PMT oscilloscope trace is photon shot noise.

2.3.2 THz optics

The THz source is the FIR laser of the UCSB Free Electron Lasers (FEL) facility. It provides coherent THz laser radiation from 1-3.5 THz with peak power of $\approx 1 - 2$ kW. The radiation comes in pulses of 1-10 μs duration at a repetition rate of 0.75-2.5 Hz. While nominally continuously tunable, certain frequencies can operate at the higher powers, longer pulse durations, and higher repetition rates. Additionally, absorption by atmospheric water vapor necessitates operation within a water-vapor transmission window since I wanted to avoid the complications of doing the experiment in a vacuum or nitrogen-purged drybox.

The THz beam is 10 cm in diameter. It passes through a variable attenuator consisting of crossed wire-grid polarizers. About 5% is split off as a reference by a mylar beamsplitter and focused by a 90^o off-axis parabolic mirror onto a pyroelectric detector. The remainder is focused by a 90^o off-axis parabolic mirror (F/1) onto the cleaved edge of the waveguide device. The spot diameter is about 500μm.

2.3.3 NIR optics

The NIR source is a continuous-wave (cw) tunable Ti:sapphire (Ti:S) laser pumped by all lines of an Ar-ion laser. About 20% is split-off by a glass slide and sent to a spectrometer to measure the wavelength. Another 20% is split-off by a glass slide to a photodiode, which feedbacks to a motorized variable neutral-density (ND) filter to keep the intensity constant.

The NIR beam polarization is fixed vertical by a Glan-Taylor prism. The beam goes through an acousto-optic modulator (AOM) where it is chopped into ≈ 25 μs pulses which overlap the ≈ 5 μs FEL pulses. Chopping the NIR beam is necessary to prevent cw photoluminescence from saturating the detector.

The chopped beam is then focused by a lens (F/10) onto the sample at the same focal point as the THz beam. The NIR beam propagates perpendicular to the THz beam. After reflection losses by the lens, cryostat window, and sapphire, the incident power is $\approx$ 600 μW and the power density is $\approx$ 50 W/cm^2. The reflected beam, sidebands, and photoluminescence are collected by the same lens, and analyzed by a second polarizer. The reflected beam is dispersed by a 0.85 m Raman double-monochromator and sidebands detected by a photomultiplier tube (PMT). The double monochromator is vital in order to detect dim sidebands near the bright laser line.

2.3.4 Detection noise limits

The PMT output is amplified and digitized on an oscilloscope. The recorded sideband signal is the integrated PMT output during the FEL pulse minus the integrated PMT output before the FEL pulse. Simultaneously, the integrated output of the reference pyroelectric detector is recorded during power dependence scans.

Because of the FEL pulse timing, there is only a microsecond of actual integration time each second. This is a single-shot detection bandwidth of 1 MHz. The optical detection noise floor was limited by photon shot-noise. These constraints allowed for a single shot sideband sensitivity of about 1 nW.

Getting 100 ms of total integration time for a single data scan can involve gated averaging for most of the day. Thus, in addition to photon shot-noise, $1/f$ noise from long-term FEL and laboratory environmental drift is a significant noise source. Unfortunately, these are unavoidable short of a high repetition-rate FEL and major structural laboratory renovations.

2.3.5 Sideband measurements

The independently controlled experimental parameters are:

- gate bias (V_g),
- NIR laser frequency (ω_{NIR}),
- monochromator detection frequency (ω_{detect}),
- THz laser frequency (ω_{THz}),
- and THz power (E_{THz}).

I made several types of sideband measurements. For clarity they have distinct terms and I will describe them here:

- In a *sideband spectrum* scan, V_g, ω_{NIR}, ω_{THz}, and E_{THz} are kept constant. Meanwhile ω_{detect} is scanned.
- In a *sideband excitation* scan, V_g, ω_{THz}, and E_{THz} are kept constant. Meanwhile, ω_{NIR} and ω_{detect} are simultaneously scanned so that $\omega_{detect} = \omega_{NIR} + \omega_{THz}$.
- In a *sideband voltage* scan, V_g is scanned while all other parameters are kept constant so that $\omega_{detect} = \omega_{NIR} + \omega_{THz}$.
- In a *sideband power dependence* scan, E_{THz} is scanned while all other parameters are kept constant so that $\omega_{detect} = \omega_{NIR} + \omega_{THz}$.

2.3.6 CW measurements

In addition to the sideband measurements, I made several cw optical measurements to understand the excitonic states of the DQW.

For PL measurements, the collected light is dispersed by a 0.35 m grating monochromator and detected by an intensified charge-coupled device camera.

For absorption measurements, the setup is illustrated in Fig. 2.5. The NIR beam is split into a signal arm and reference arm by a Glan-Taylor prism. The signal arm is chopped at 1 kHz by an AOM, while the reference arm is chopped at around 300 Hz by a mechanical chopper.

The signal and reference are recombined in a beam-splitting cube and focused onto the sample. The signal arm is focused onto the mesa containing the active region. However, the reference arm is offset slightly so it is focused onto an etched region containing only the DBR.

Both signal and reference are detected by a single photodiode. The photodiode signal is sent to two lock-in amplifiers to separate signal from reference. To perform a scan the NIR laser is tuned in the bandgap where there is no absorption, and the signal and reference arms nulled. For a 300 ms integration time reflection changes of about 10^{-4} could be measured.

The reflection data collected cannot be strictly converted to strictly absorption. The measured "absorption" based on the reflection data is

$$\alpha_{exp} = 1 - \frac{R_0 + (1-\alpha)R_{DBR}}{R_0 + R_{DBR}} \tag{2.3.1}$$

where α is the actual absorption of the DQW region, R_{DBR} is the reflectivity of the DBR, and R_0 is the front-surface reflection. As $R_0 \rightarrow 0, \alpha_{exp} \rightarrow \alpha$. Clearly it is a good thing to minimize front-surface reflection. Evaporating a $\lambda/4$ layer of SrF_2 as an antireflection coating dropped R_0 from over 55% to $\approx$ 25%.

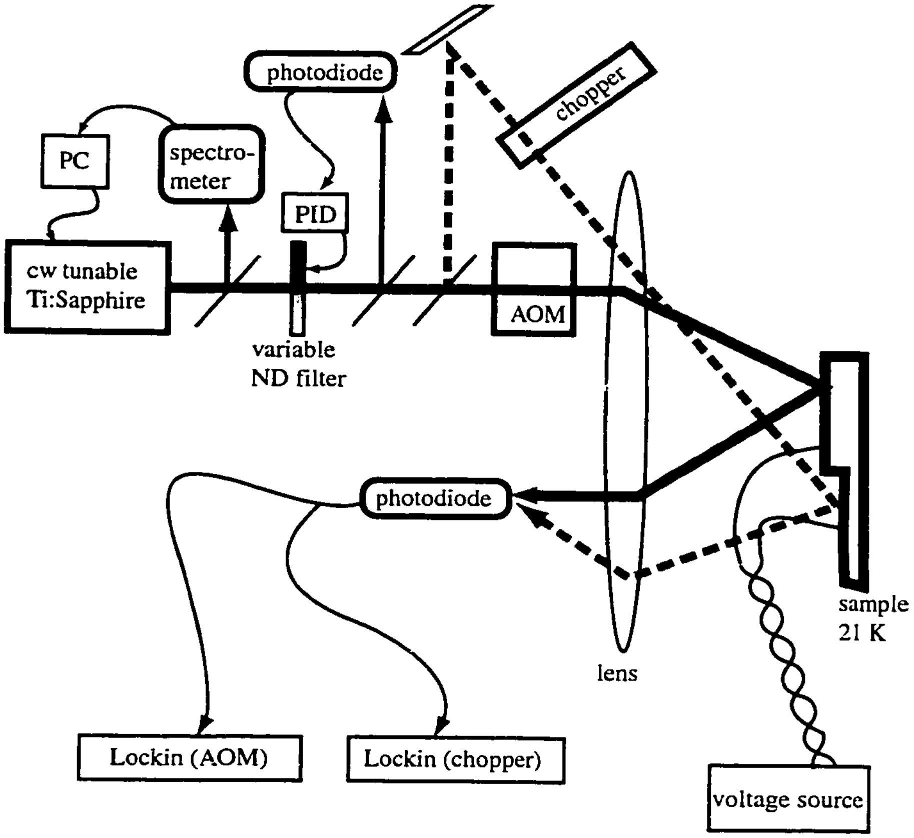

Figure 2.5: Experimental layout for reflection measurement. Reference arm is dotted line.

Chapter 3

Direct and indirect exciton tunnelling in tilted double quantum wells

To understand the results of the THz-NIR modulation study it is important to first understand the states of the DQW as a function of tilt using cw interband PL and absorption spectroscopy. The exciton states involve a rich interplay between Coulomb binding, tunnel-splitting, and quantum-confinement, as all of the energy scales are on order of $\approx$ 10 meV. These exciton states are both direct (electron and hole on the same side of the tunnel barrier) and indirect (electron and hole on opposite sides of the tunnel barrier). A DC voltage applied to the gates tilts the bands and tunes indirect excitons into tunnel resonance with direct excitons, resulting in a web of avoided crossings. The spectra are modelled in the effective-mass approximation with no free parameters.

This information is useful beyond the scope of the THz modulation experiments, as excitons in DQWs are of interest in a diverse array of experiments and applications, from Bose-Einstein condensation of excitons to linearly-tunable optical filters. Surprisingly, even the cw interband spectroscopy of DQW exciton states have only been studied in detail in the past few years, and then only in symmetric DQWs[21, 22, 23, 24, 25].

3.1 Experimental results

I measured the PL spectra and absorption spectra of the DQW at 21 K as a function of gate bias. The excitation frequency for the PL was 13000 cm^{-1}, well below the AlGaAs barriers. Typical PL and reflection spectra are presented in Figs. 3.1 and 3.2. The peak assignments were derived from the theory described in the next section.

While the reflection spectrum is sensitive to the excitons and their e-h continuum states, at the experimental temperature the PL is sensitive only to the exciton states. This is because the luminescence is Boltzman weighted to the low-energy states of a subband, which are the bound exciton states.

Fig. 3.3 shows the PL spectra as a function of gate bias (a PL voltage scan, or PLVS). Fig. 3.4 shows a waterfall plot of several reflection spectra at various gate biases. The electric field is just given by $V_g/8000$ Å, the distance between front and back gates.

The striking features of the PLVS are a set of peaks that change with gate bias which anticross with a set of peaks that stay relatively constant with gate bias. The result is a complicated maze of avoided crossings. Again, the excitonic peaks in absorption line up with the PL peaks, albeit on top of a large e-h continuum background.

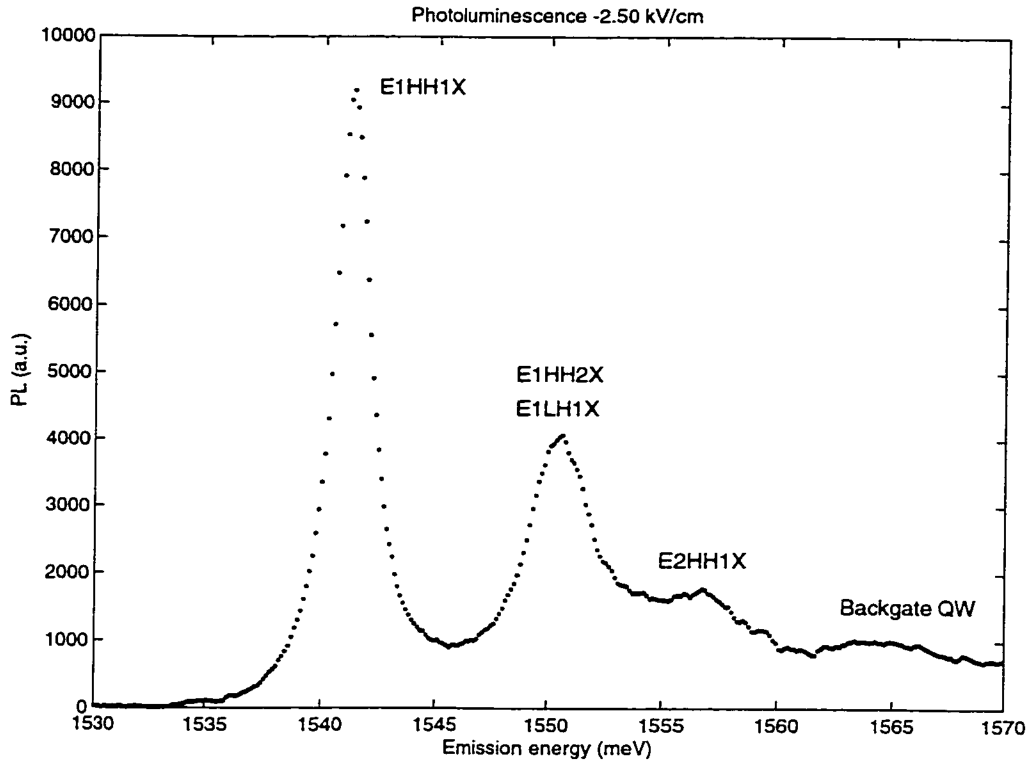

Figure 3.1: Typical photoluminescence. Peak assignments are from theory.

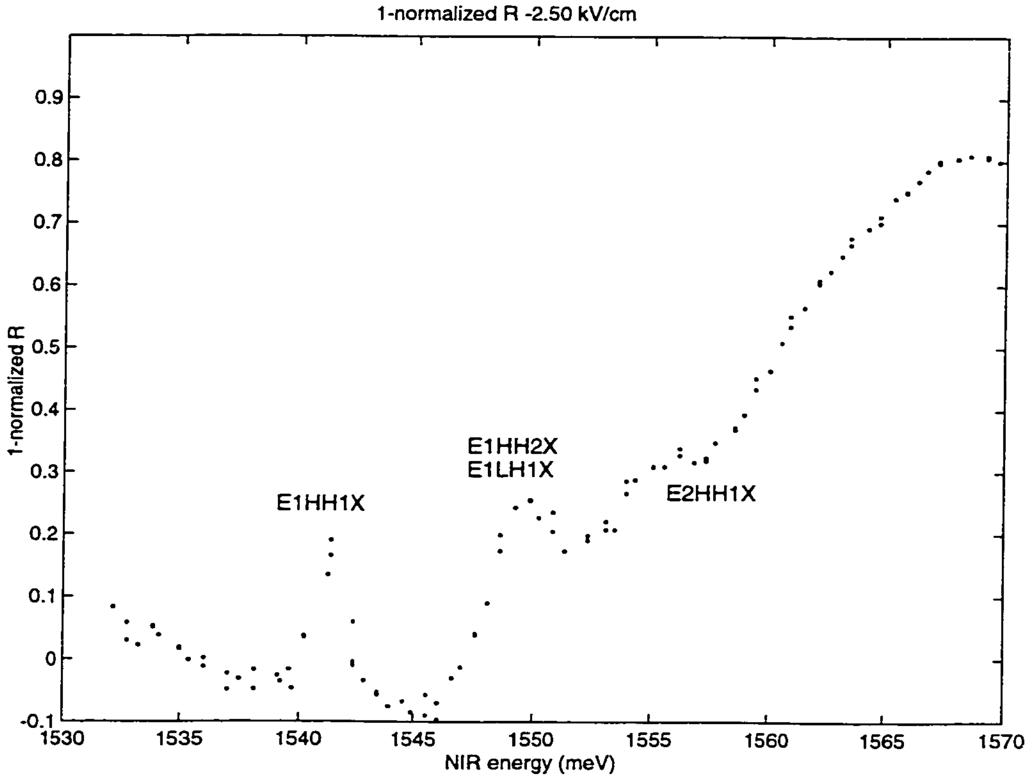

Figure 3.2: Typical normalized reflection spectrum. The quantity plotted is $1 - R_{DQW}/R_{DBR}$. The DQW and DBR arms are balanced at 1535 meV. Peak assignments are from theory.

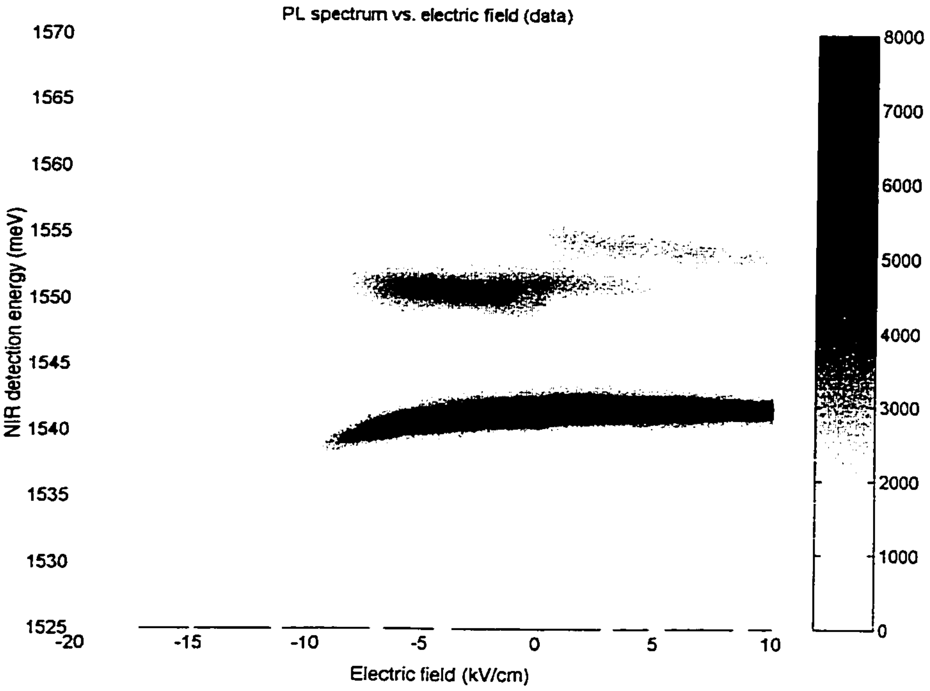

Figure 3.3: Photoluminescence spectra as a function of gate bias. The electric field is $V_g/8000$ Å, the distance between front and back gates.

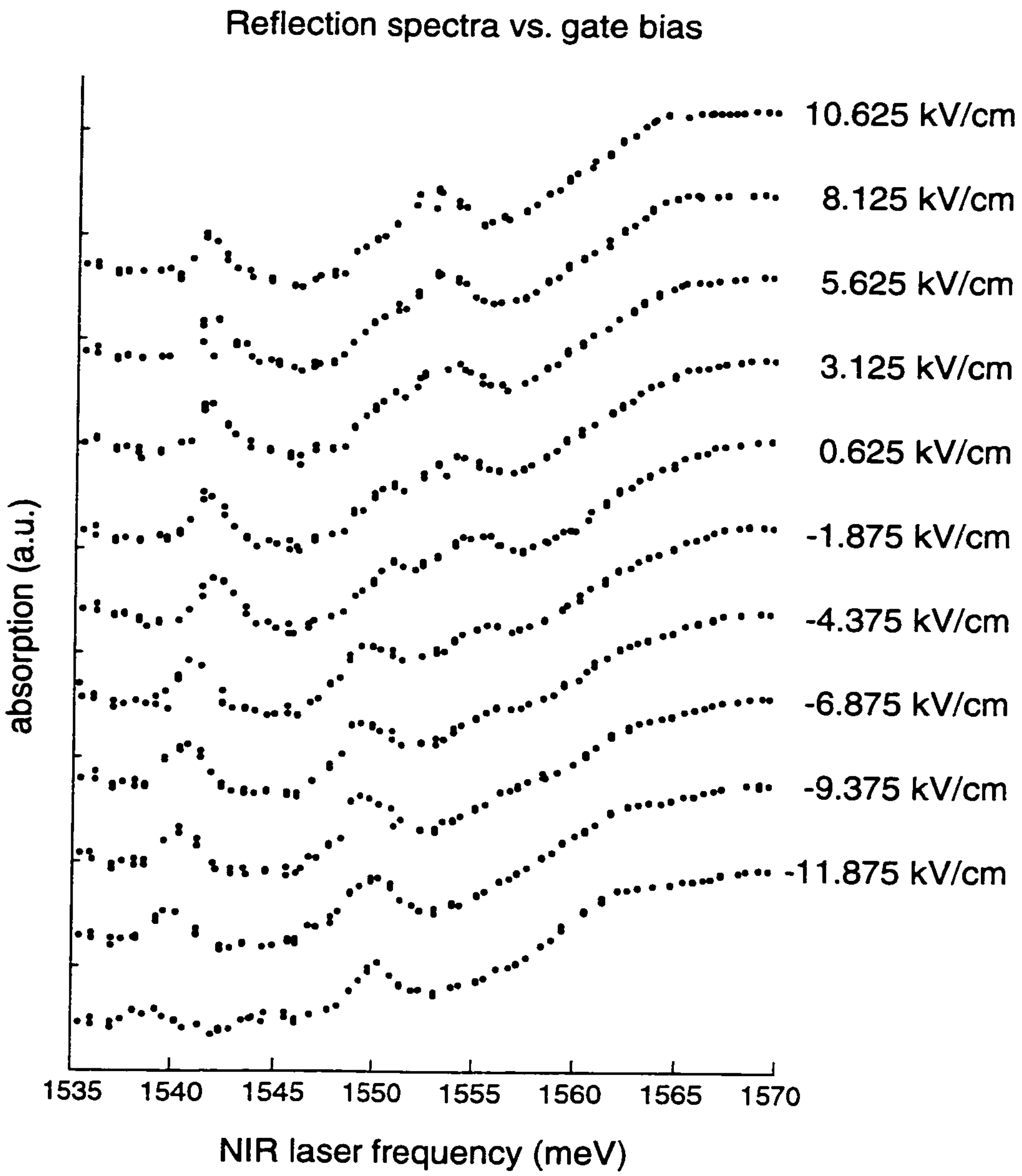

Figure 3.4: Reflection spectra as a function of gate bias.

3.2 Theory

3.2.1 Hamiltonian

The electron-hole Hamiltonian for an exciton in the DQW is [1]

$$H = H_z + H_{cm} + V_{eh} + E_{gap} \tag{3.2.1}$$

where H_z is given by

$$H_z = \frac{-\hbar^2}{2m_e}\frac{\partial^2}{\partial z_e^2} + V_e(z_e) + \frac{-\hbar^2}{2m_{h,z}}\frac{\partial^2}{\partial z_h^2} + V_h(z_h) \tag{3.2.2}$$

where z_e (z_h) is the z-component of the position for the electron (hole), m_e is the effective mass of the electron, $m_{h,z}$ is the effective mass of the hole in the z-direction, and V_e (V_h) is the quantum-well potential energy for the electron (hole), H_{cm} is the center-of-mass energy in the xy plane, V_{eh} is the electron-hole interaction energy, and E_{gap} is the bandgap.

The e-h center-of-mass energy is

$$H_{cm} = \frac{P_{xy}^2}{2(m_e + m_{h,xy})} \tag{3.2.3}$$

where P_{xy} is the center-of-mass momentum in the xy-plane, and $m_{h,xy}$ is the effective mass of the hole in the xy plane. Only excitons with $P_{xy} = 0$ can couple to a photon, so this part of the Hamiltonian can be ignored.

The e-h interaction Hamiltonian is

$$H_{eh} = \frac{-\hbar^2}{2\mu}\nabla_\rho^2 + \frac{1}{4\pi\epsilon_0\epsilon}\frac{e^2}{r} \tag{3.2.4}$$

where μ is the xy-plane reduced mass

$$\frac{1}{\mu} = \frac{1}{m_e} + \frac{1}{m_{h,xy}} \tag{3.2.5}$$

---

[1] The theory described in this section follows closely that of [26, 2]

r is the electron-hole separation

$$r = \sqrt{\rho^2 + (z_e - z_h)^2} \tag{3.2.6}$$

and ∇_ρ^2 is the cylindrical Laplacian operator:

$$\nabla_\rho^2 = \frac{1}{\rho}\frac{\partial}{\partial\rho}\left[\rho\frac{\partial}{\partial\rho}\right]$$

In general, (3.2.1) is not separable because of the explicit dependence of r on $z_e - z_h$ in (3.2.4) through (3.2.6). Therefore I solved for the $1s$ exciton states using a variational method with the trial wavefunction

$$\phi_{\mu\nu}(\rho, z_e, z_h) = N_{\mu\nu} f_\mu(z_e) g_\nu(z_h) \varphi_{\mu\nu}(\rho, |z_e - z_h|) \tag{3.2.7}$$

where $f_\mu(z_e)$ and $g_\nu(z_h)$) are the single-particle electron and hole solutions to (3.2.2), respectively. $\varphi_{\mu\nu}$ is the excitonic $1s$ wavefunction

$$\varphi_{\mu\nu} = exp\left(-\frac{r}{R_{\mu\nu}}\right) \tag{3.2.8}$$

where r is the electron-hole separation given by (3.2.6) and $R_{\mu\nu}$ is the excitonic Bohr radius. In general the Bohr radius (and thus the exciton binding energy) will vary with the electron subband index μ and hole subband index ν, because the average z-separation between electron and hole differs between subbands. This is especially true when an external electric field is applied to the confinement potentials $V_e(z_e)$ and $V_h(z_h)$.

The normalization constant $N_{\mu\nu}$ is given by

$$N_{\mu\nu} = \left[2\pi \int_{-\infty}^{\infty} dz_e \int_{-\infty}^{\infty} dz_h \int_0^{\infty} \phi_{\mu\nu}^2(\rho, z_e, z_h)\rho d\rho\right]^{-1/2} \tag{3.2.9}$$

3.2.2 Material parameters

The bandgap for $Al_xGa_{1-x}As$ is given in eV by

$$E_{gap} = 1.52 + 1.36x + 0.22x^2 \tag{3.2.10}$$

The conduction band offset is 0.65. The electron effective mass m_e is $0.067m_0$ where m_0 is the electron rest mass. Hole masses are given by Luttinger parameters:

$$\begin{gathered} \Gamma_1 = 6.790, \Gamma_2 = 1.924 \\ m_{hh,z} = m_0/(\Gamma_1 - 2\Gamma_2), m_{lh,z} = m_0/(\Gamma_1 + 2\Gamma_2) \\ m_{hh,xy} = m_0/(\Gamma_1 + \Gamma_2), m_{lh,xy} = m_0/(\Gamma_1 - \Gamma_2) \end{gathered} \tag{3.2.11}$$

3.2.3 Noninteracting e-h states and energies

The single-particle electron and hole wavefunctions $f_\mu(z_e)$ and $g_\nu(z_h)$ for each value of the applied electric field were obtained by numerically integrating (3.2.2).

Fig. 3.5 illustrates the effect of a tilt applied to the DQW. Electrons in the left well can tunnel-couple with electrons in the right well. Similarly, holes in opposite wells can come into tunnel resonance at a particular tilt. It is helpful to visualize the states as a continuous function of tilt as surface plots in Figs. 3.6, 3.7, and 3.8. The states are labeled in the order of their energies at the particular tilt. For example HH1 is the ground heavy-hole state, LH1 is the ground light-hole state, and E1 is the ground electron state.

At high electric fields the electron and light-hole states are localized in either left or right well, while at intermediate fields they tunnel between both left and right wells. Meanwhile heavy-holes, because of their greater mass, stay more localized in either the left- or the right-side well. Note also the alternating symmetry of the excited states.

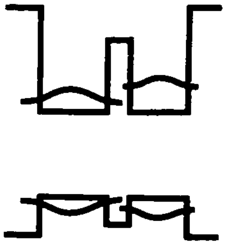

A) flat-band

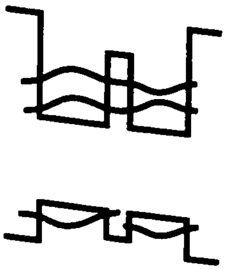

B) electron tunnel resonance

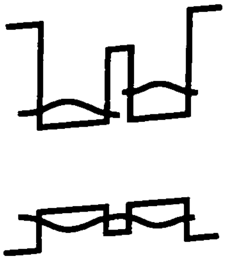

C) hole tunnel resonance

Figure 3.5: Electrons and holes in wells on opposite sides of the barrier can come into tunnel resonance at particular tilts.

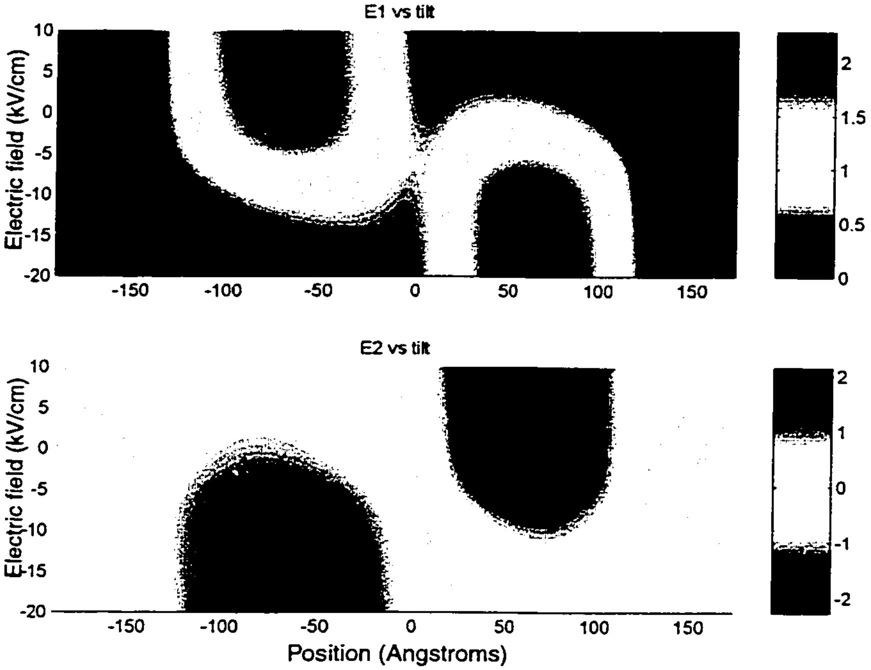

Figure 3.6: Free electron states $f(z_e)$ as a function of gate bias.

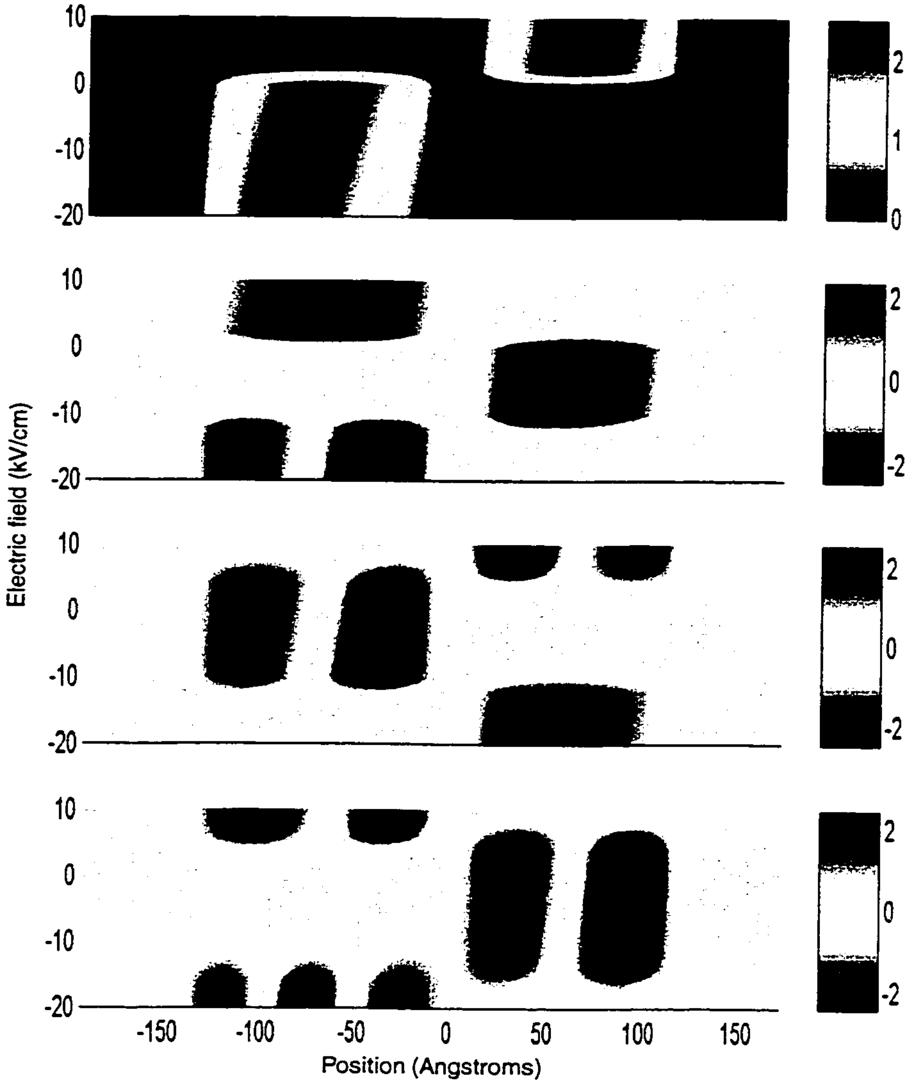

Figure 3.7: Free heavy-hole states $g_{hh}(z_{hh})$ as a function of gate bias.

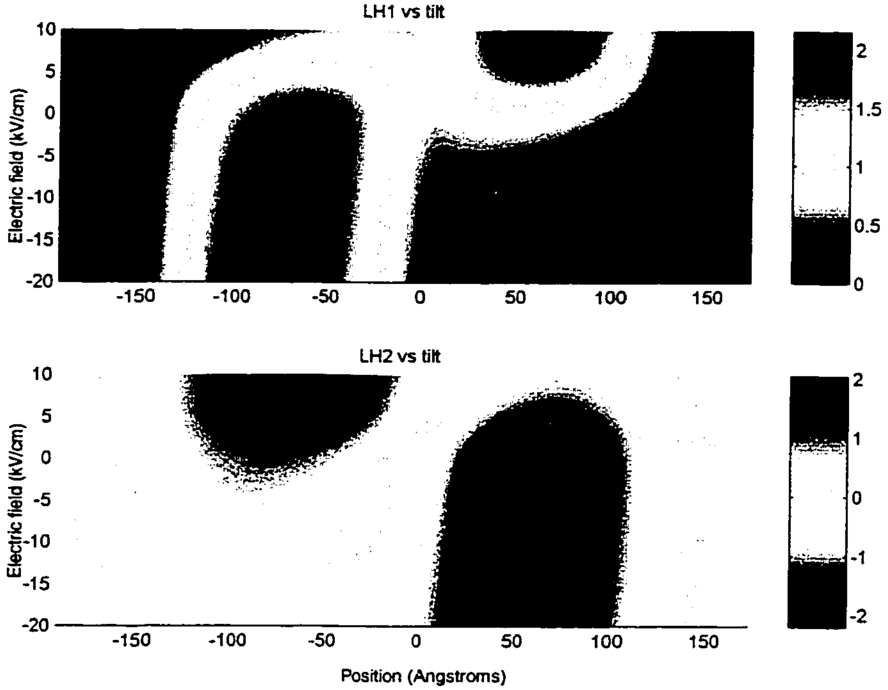

Figure 3.8: Free light-hole states $g_{lh}(z_{lh})$ as a function of gate bias.

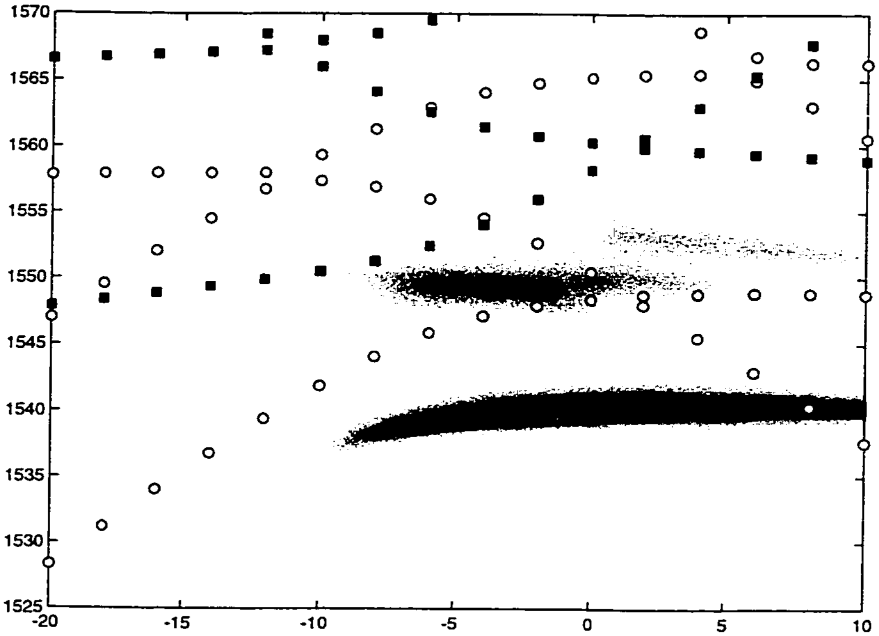

Figure 3.9: $k = 0$ energies of the free electron-heavy-hole states $E_\mu HH_\nu$ overlaid on the experimental PL. Blue circles are $E1HH_\nu$ while red squares are $E2HH_\nu$. The agreement is poor.

The energies of the two-particle state at xy-plane wavevector k are given in a parabolic effective-mass approximation as

$$\hbar\omega^{fr}_{\mu\nu}(k) = E^e_\mu + E^h_\nu + \frac{\hbar^2 k^2}{2m_e} + \frac{\hbar^2 k^2}{2m_{h,xy}} + E_{gap} \tag{3.2.12}$$

where E^e_μ (E^h_ν) is the $k = 0$ eigenenergy of electron subband f_μ (hole subband g_ν). The calculated $k = 0$ electron-heavy-hole pair energies are in Fig. 3.9. Note that the avoided crossings do not match those of the experimental PL data.

3.2.4 Exciton states and energies

The exciton states $\phi_{\mu\nu}$ were solved by numerically minimizing the expectation value of the e-h interaction energy H_{eh} (3.2.4) with the Bohr radius $R_{\mu\nu}$ as the variational parameter. A typical plot of $\langle H_{eh} \rangle$ vs. R is shown in Fig. 3.10. The minimum gives the exciton binding energy $E_{\mu\nu}^{bind}$.

A plot of binding energy vs. tilt of the various e-h pairs is given Figs. 3.11-3.13. Note the strong dependence on applied electric field and subband indices.

The total exciton energy is given by

$$\hbar\omega_{\mu\nu} = E_{\mu}^{e} + E_{\nu}^{h} + E_{\mu\nu}^{bind} + E_{gap} \tag{3.2.13}$$

A plot of the heavy-hole exciton energies is overlayed with the experimental PL data in Fig. 3.14. A similar plot for light-hole excitons is in Fig. 3.15. The agreement of peak positions is very good, especially considering that there are *no fitting parameters.*

3.2.5 Direct and indirect excitons

A intuitive qualitative understanding of the exciton states can be best obtained in a delocalized basis. In such a basis we ignore tunnel-coupling and consider electrons and holes localized to either the left- or the right-side well. Label these states EL, HL, ER, HR. Then we can construct excitons from pairs corresponding to all the pairs of electrons and holes. The *direct* excitons correspond to electrons and holes in the same side (ELHL, ERHR), while *indirect* excitons correspond to electrons and holes on opposite sides (ELHR, ERHL).

Now, by applying an electric field, we tilt the potential energy as in Fig 3.16b. Thus, the ELHR exciton gets higher in energy while the HRHL gets lower in energy. Meanwhile the direct exciton energies change only to second-order.

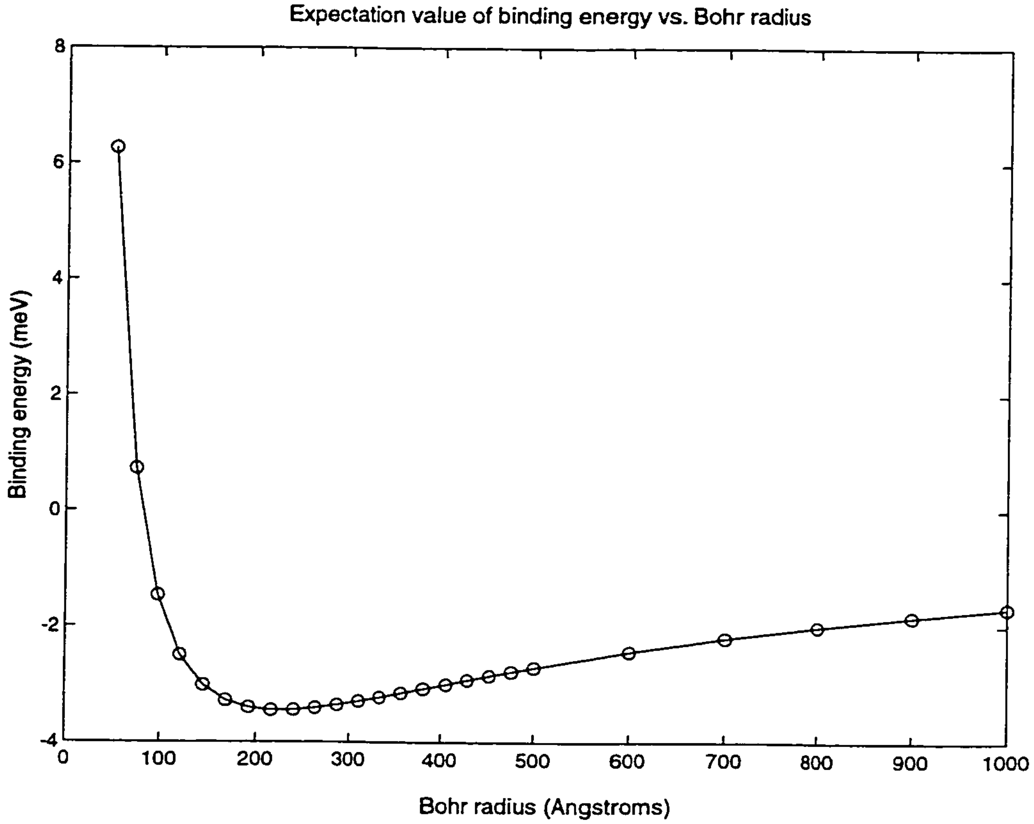

Figure 3.10: Expectation value of the binding energy E_{eh} vs. Bohr radius R for E1H1 at -20 kV/cm.

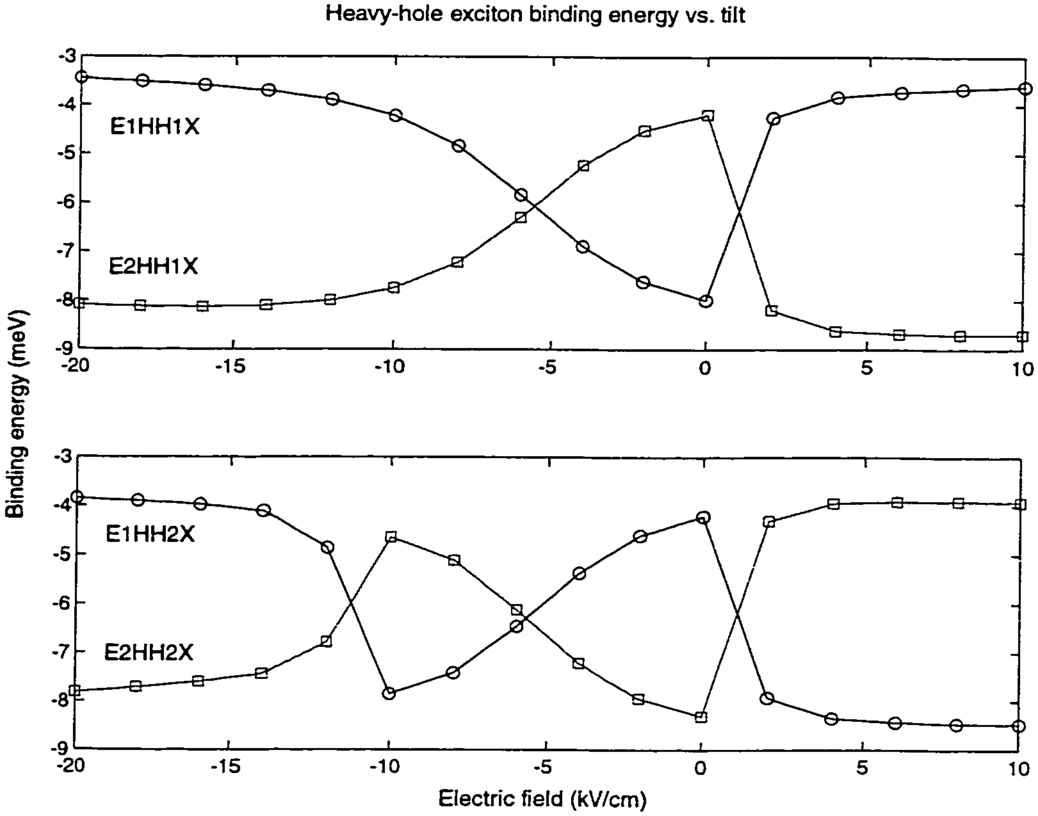

Figure 3.11: Heavy-hole exciton binding energy vs. tilt for $E_\mu HH_1$ and $E_\mu HH_2$.

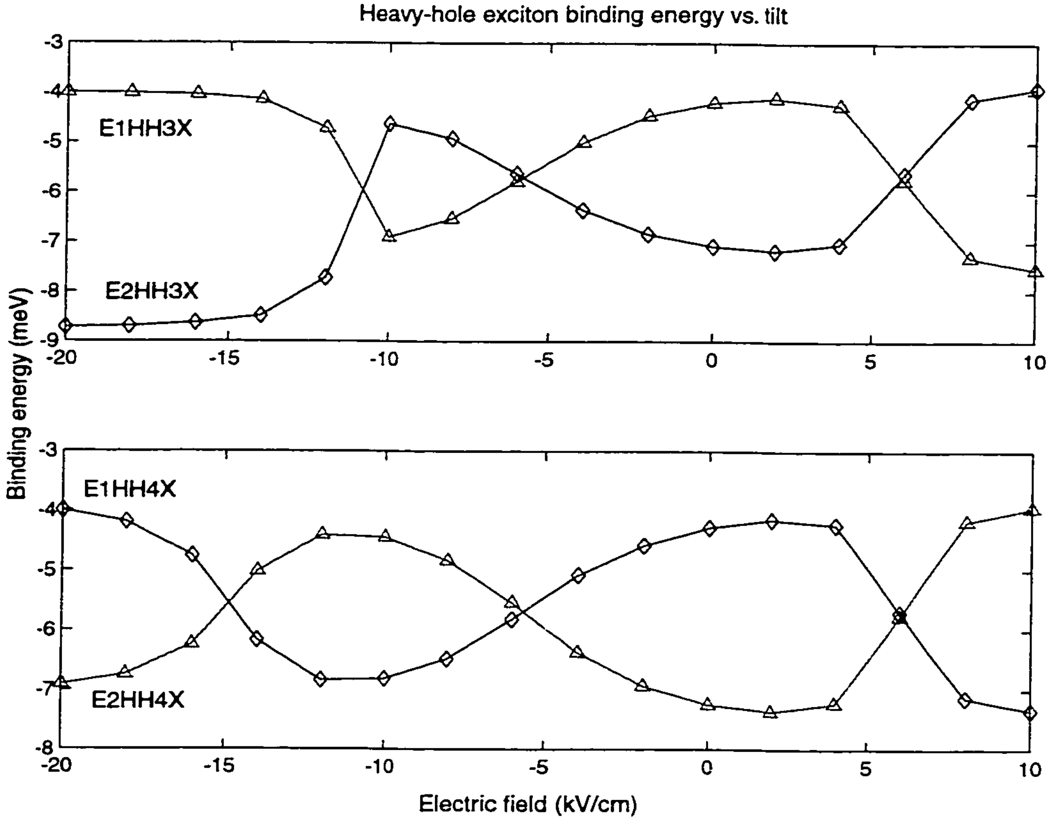

Figure 3.12: Heavy-hole exciton binding energy vs. tilt for $E_{\mu}HH_1$ and $E_{\mu}HH_2$.

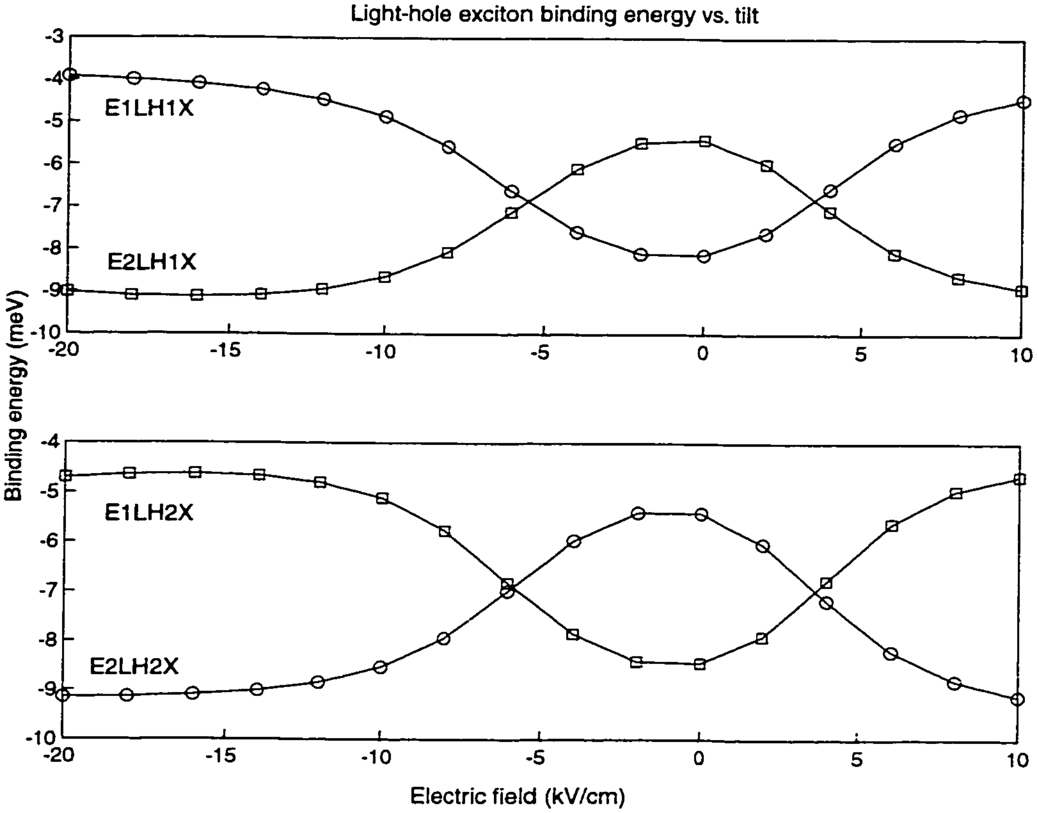

Figure 3.13: Light-hole exciton binding energy vs. tilt for $E_\mu HH_1$ and $E_\mu HH_2$.

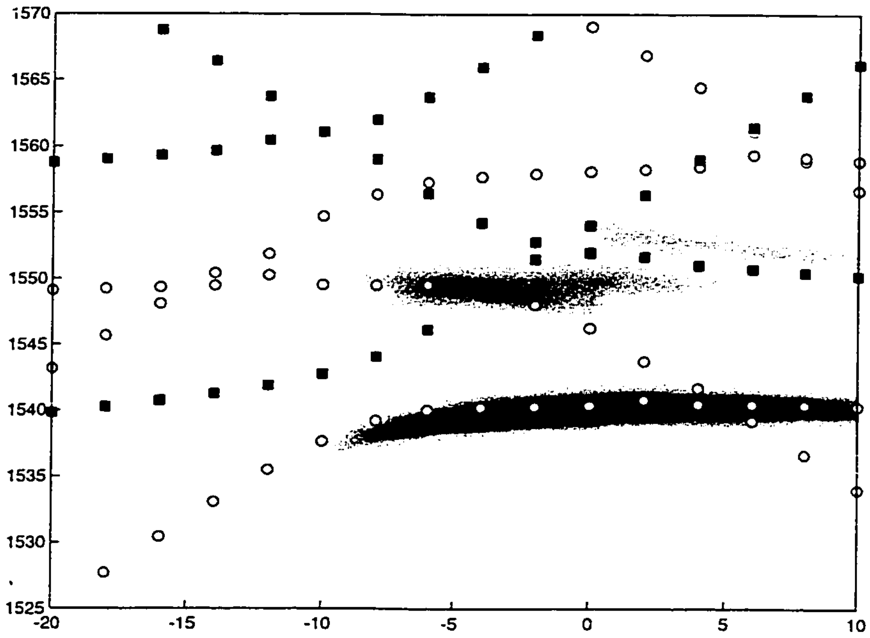

Figure 3.14: Calculated $E_\mu HH_\nu$ heavy-hole exciton energies overlaid on experimental PL. There are no fitting parameters.

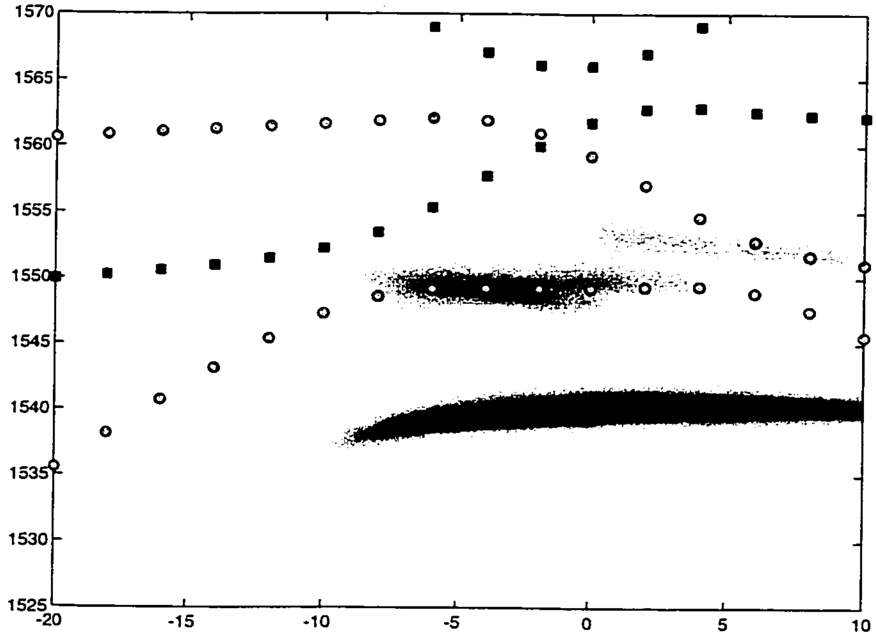

Figure 3.15: Calculated $E_\mu LH_\nu$ light-hole exciton energies overlaid on experimental PL. There are no fitting parameters.

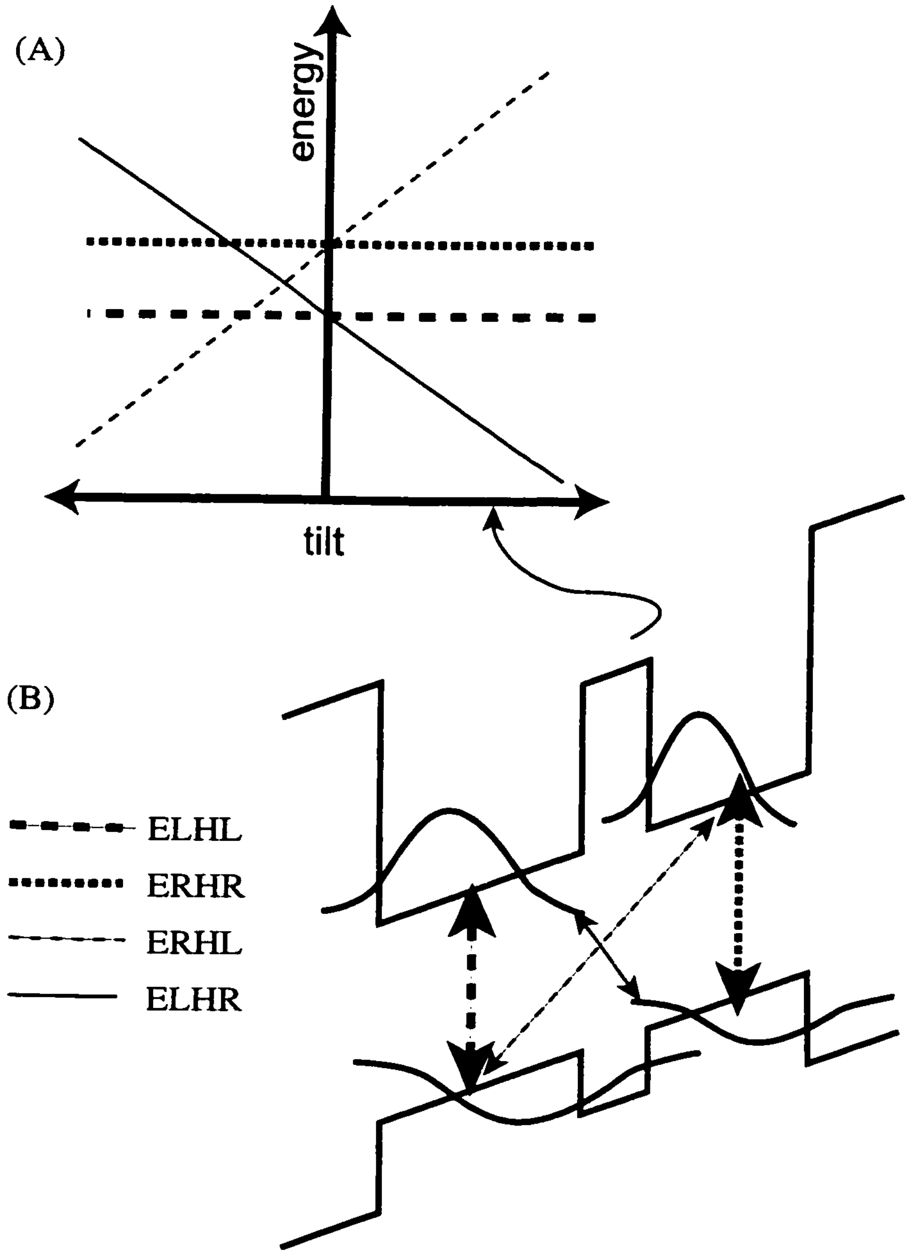

Figure 3.16: Direct and indirect excitons tune with tilt.

Schematically plotting the exciton energies vs. tilt in Fig 3.16a, we see that indirect excitons tune with tilt and cross with direct excitons. Now if we turn on the tunnel-coupling, the indirect excitons will tunnel-couple with direct excitons, resulting in anticrossings.

3.2.6 Linear susceptibility

For x-polarized light, the strength of an interband transition from the vacuum state $|0\rangle$ to a particular exciton $|\phi_{\mu\nu}\rangle$ is proportional to the exciton interband dipole moment

$$\langle\phi_{\mu\nu}|ex|0\rangle = F_{\mu\nu}X_{cv} \tag{3.2.14}$$

where $X_{cv} = \langle\Psi_c|ex|\Psi_v\rangle$ is the dipole moment between the conduction band Bloch function Ψ_c and the valence band Bloch function Ψ_v. $F_{\mu\nu}$ is the electron-hole overlap integral

$$\begin{aligned} F_{\mu\nu} &= \int \phi_{\mu\nu}(\rho = 0, z_e = z, z_h = z)dz \\ &= N_{\mu\nu}\int f_\mu(z)g_\nu(z)dz \end{aligned} \tag{3.2.15}$$

The linear interband susceptibility for excitons in an undoped quantum well is given by

$$\chi^{(1)}_{ex}(\omega) = \frac{N_0X^2_{cv}}{\epsilon_0\hbar}\sum_{\mu,\nu}\frac{F^2_{\mu\nu}}{\omega_{\mu\nu} - \omega - i\gamma_{\mu\nu}} \tag{3.2.16}$$

where $\hbar\omega_{\mu\nu}$ is the exciton energy, $\gamma_{\mu\nu}$ is a phenomenological linewidth, and N_0 is the density of the filled valence band. The strength of absorption and emission from excitons is proportional to $|\text{Im}\chi^{(1)}_{ex}(\omega)|^2$, plotted vs. tilt in Fig. chi1x. Again, the agreement with PL data is very good, considering that the only free parameter is a single linewidth $\gamma = 1.5$ meV.

As I pointed out earlier, the PL samples the exciton states while absorption is also sensitive to the e-h continuum states. Therefore, a direct comparison with the

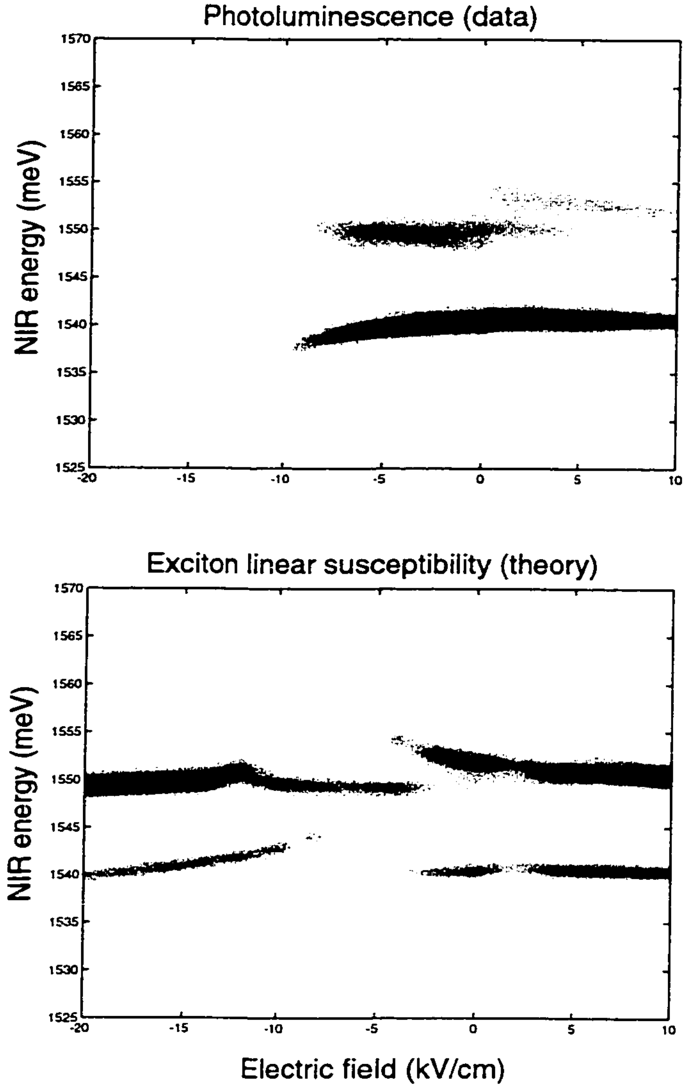

Figure 3.17: TOP: Photoluminescence data. BOTTOM: $|\mathrm{Im}\ \chi^{(1)}|$ for excitons.

absorption spectra is not very good in an exciton-only model. To include the free e-h continuum states, the additional term must be added:

$$\chi_{fr}^{(1)}(\omega) = \frac{1}{N_{\mu\nu}^2}\frac{N_0 X_{cv}^2}{\epsilon_0 \hbar}\sum_{\mu,\nu}\int_0^\infty \frac{F_{\mu\nu}^2}{\omega_{\mu\nu}^{fr}(k) - \omega - i\gamma} k dk \tag{3.2.17}$$

Here I used the same linewidth γ as for excitons. Also note that the interband oscillator strength is weaker by a factor of $N_{\mu\nu}$, the normalization constant for the exciton wavefunction. The total linear susceptibility is the sum of the contribution from excitons and free electron-hole states.

$$\chi^{(1)} = \chi_{ex}^{(1)} + \chi_{fr}^{(1)} \tag{3.2.18}$$

The calculated $|\mathrm{Im}\chi^{(1)}(\omega)|^2$ is plotted vs. absorption data for various tilts V_g in Fig 3.18. The agreement is good. Exact quantitative agreement suffers because largely because of front surface reflection, as described in Sec. 2.3.5. Additionally, many-body Coulomb interactions between free electrons and holes are not included.

3.2.7 A comment on intersubband and valence-band mixing

In this model, for simplicity, I ignored Coulomb mixing between subbands. This is actually only justified when the subband level separation is greater than the exciton binding energy[24], which is not the case near level crossings. Therefore some avoided crossings will be underestimated.

I also ignored valence-band mixing between heavy and light-holes. I actually did perform a calculation incorporating a valence-band mixing effect. Its effect on the energy levels was small ($\approx$ 2 meV). Including it in the calculation of exciton states would be complicated since the effective-mass approximation would be invalid.

This is not to say that that valence-band mixing is unimportant. Indeed, when I excited PL with a circularly-polarized pump, the flat-band luminescence has no

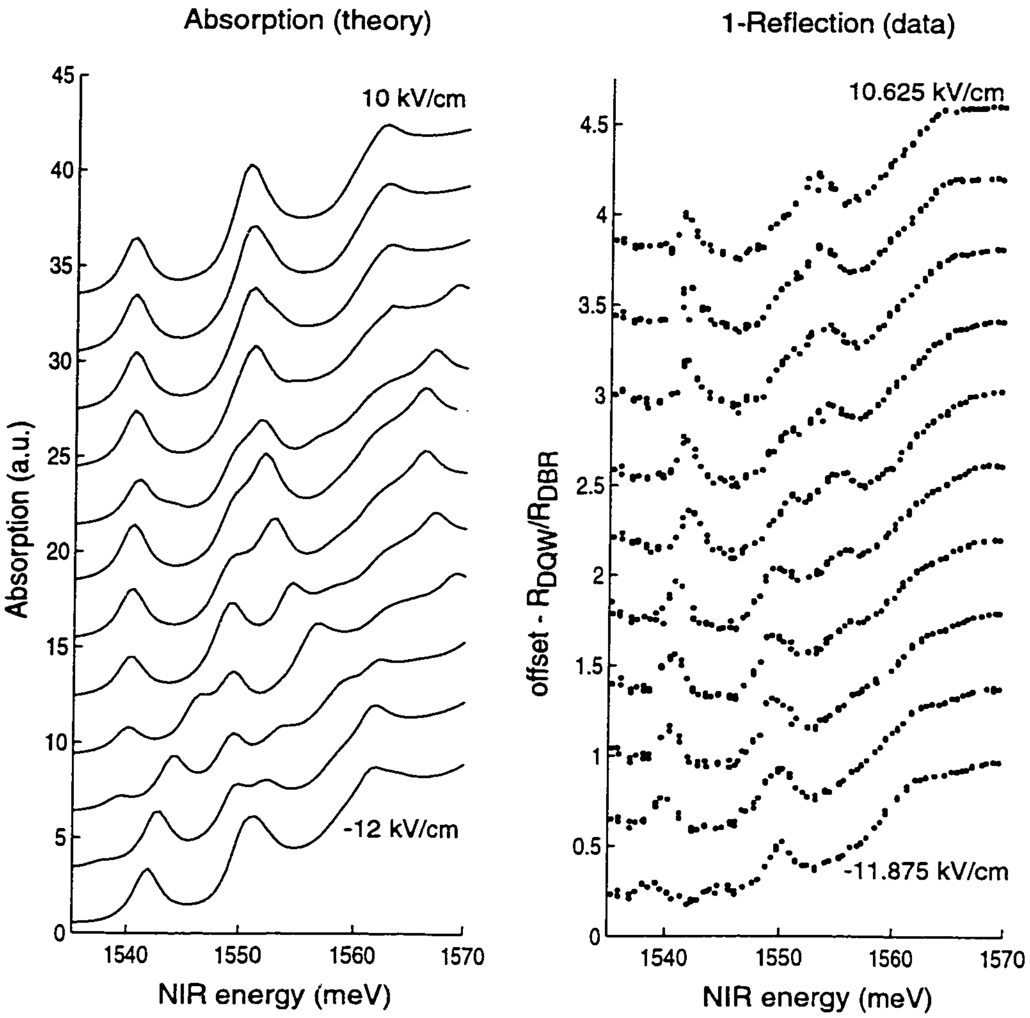

Figure 3.18: LEFT: Theoretical $|\mathrm{Im}\ \chi^{(1)}|$ for excitons and free electrons and holes. Normalized reflection data $(1 - R_{DQW}/R_{DBR})$.

particular circular polarization dependence on detection wavelength. It is likely that light and heavy-hole excitons in this DQW system are heavily mixed by tunneling, in contrast to a weakly-coupled DQW and conventional square quantum wells.

In this experiment however, none of the laser fields couple to a spin degree of freedom, so the fact that our exciton state labelling of heavy- and light-hole excitons is not quite correct is acceptable.

Chapter 4

THz-NIR modulation by excitonic intersubband excitation

Driving the DQW exciton states described the in the previous chapter with a THz electric field of frequency ω_{THz} polarized in the z-direction causes the interband index of refraction to be modulated at ω_{THz}. This manifests itself as terahertz optical sidebands on a weak NIR probe. I studied in detail the resonance properties of the sideband generation as functions of ω_{THz}, ω_{NIR}, and V_{gate} in a regime where the sideband is proportional to the THz intensity.

The resonance measurements are modelled by a second-order nonlinear susceptibility with no fitting parameters based on the states calculated in Sec. 3.2. The resonance conditions can be best understood as the THz field inducing a virtual excitonic intersubband transition. This represents the first detailed spectroscopic study of the excitonic intersubband transition in double quantum wells.

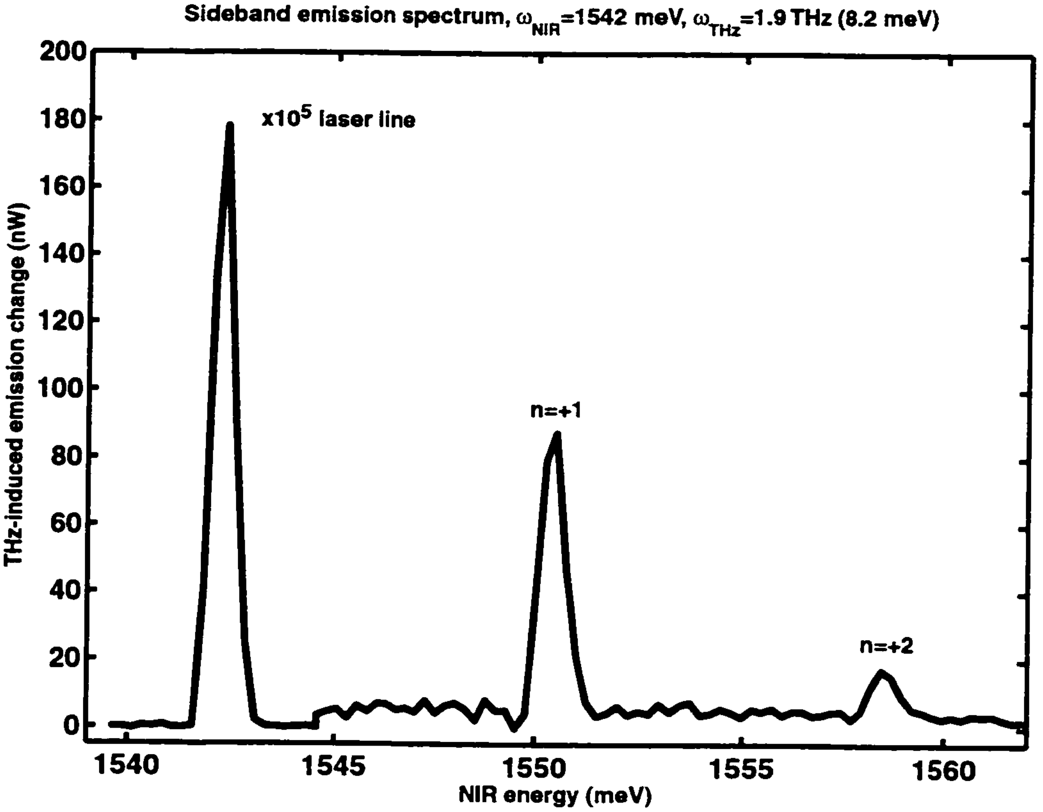

Figure 4.1: $n > 0$ sideband spectrum.

4.1 Experimental results

The results presented in this section are for sideband spectrum scans, sideband excitation scans, and sideband voltage scans as described in Sec. 2.3.5. The waveguide device has no sapphire. As mentioned before in Sec. 2.3.5, in this geometry the THz field at the active DQW region is weak because the epilayer is at the air-semiconductor interface of the dielectric waveguide.

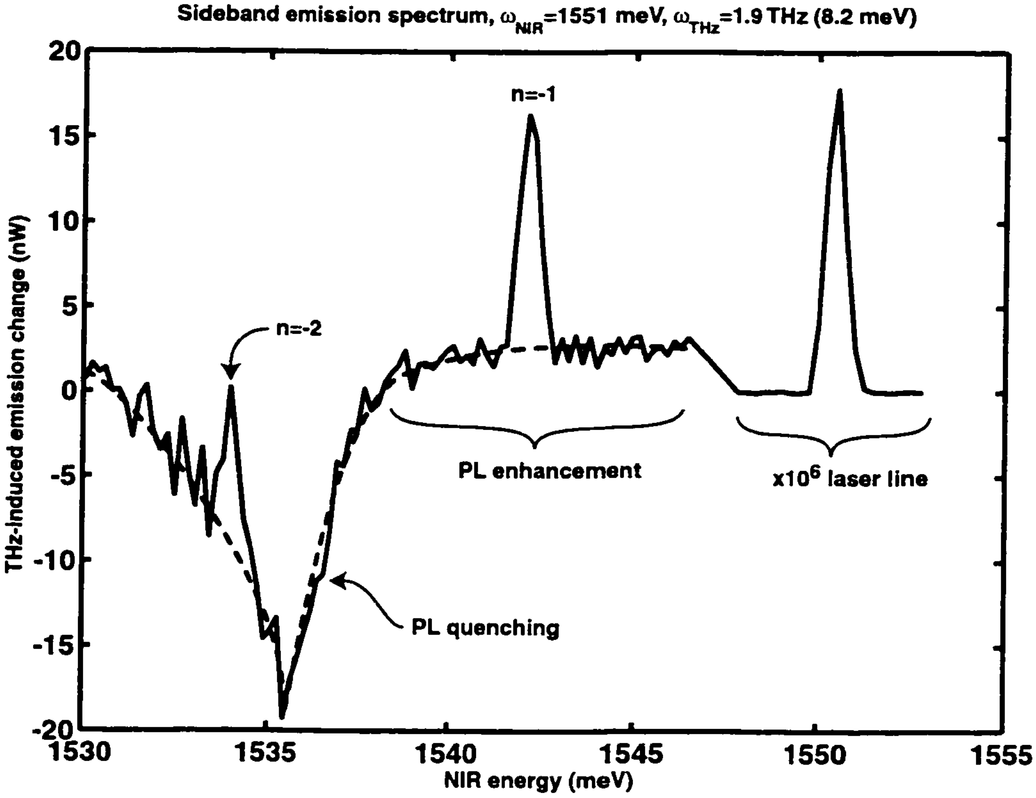

Figure 4.2: $n < 0$ sideband spectrum.

A typical $n > 0$ sideband spectrum is shown in Fig. 4.1. A $n < 0$ sideband spectrum is shown in Fig 4.2. Note that the resonant conditions for negative and positive sidebands are different. Although I could measure the $n = -1$ sideband, its analysis was complicated by background PL which appears below the pump laser line. The PL is quenched by an xy-polarized component of the THz field. Indeed, the sideband tends to be maximized as the PL quenching is minimized. Nonetheless, since background PL is negligible several THz above the laser line it made the most sense to focus the experiments on the positive sideband.

Some sideband excitation scans for a weakly coupled, ungated DQW sample (75/25×0.3/85) are shown in Fig. 4.3. The bandgap as measured by absorption is indicated by the arrow.

The sideband always had the same linear and circular polarization state as the incident NIR beam. They were detectable only when the THz radiation had a linear polarization component normal to the QW and occured even when $\hbar\omega_{NIR}$ was less than the bandgap as seen in the leftmost peak of Fig. 4.3b. These selection rules show that the sidebands originate from virtual transitions which absorb neither energy nor momentum from the optical fields and do not depend on presence of real carriers.

The sideband excitation scan for the strongly-coupled gated DQW (100/12×0.2/120) at $V_g = 0$ V and $\omega_{THz} = 2.5$ THz is shown in Fig. 4.4. The sideband voltage scan at with $\omega_{NIR} = 1546$ meV and $\omega_{THz} = 2.5$ THz is shown in Fig. 4.5. The distinct peaks are labelled with excitonic transition assignments derived from the theory described in the next section. Clearly to understand the full resonant structure of the sideband generation process at each THz frequency I must measure the sideband as a continuous function of both ω_{NIR} and V_g to generate a 2-d sideband map. (Ideally ω_{THz} could be swept continuously but this is not feasible using the FEL.)

By taking a sideband voltage scan at each ω_{NIR} I measured the sideband maps

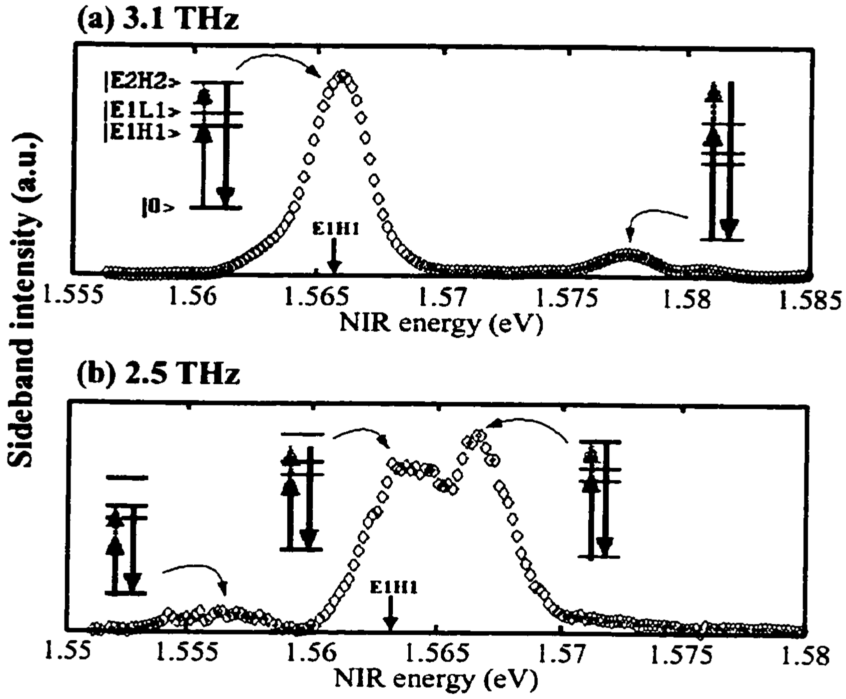

Figure 4.3: Sideband excitation scan for sample [75/25×0.3/85] at $V_g = 0$ V and $\omega_{THz} = 3.1$ THz.

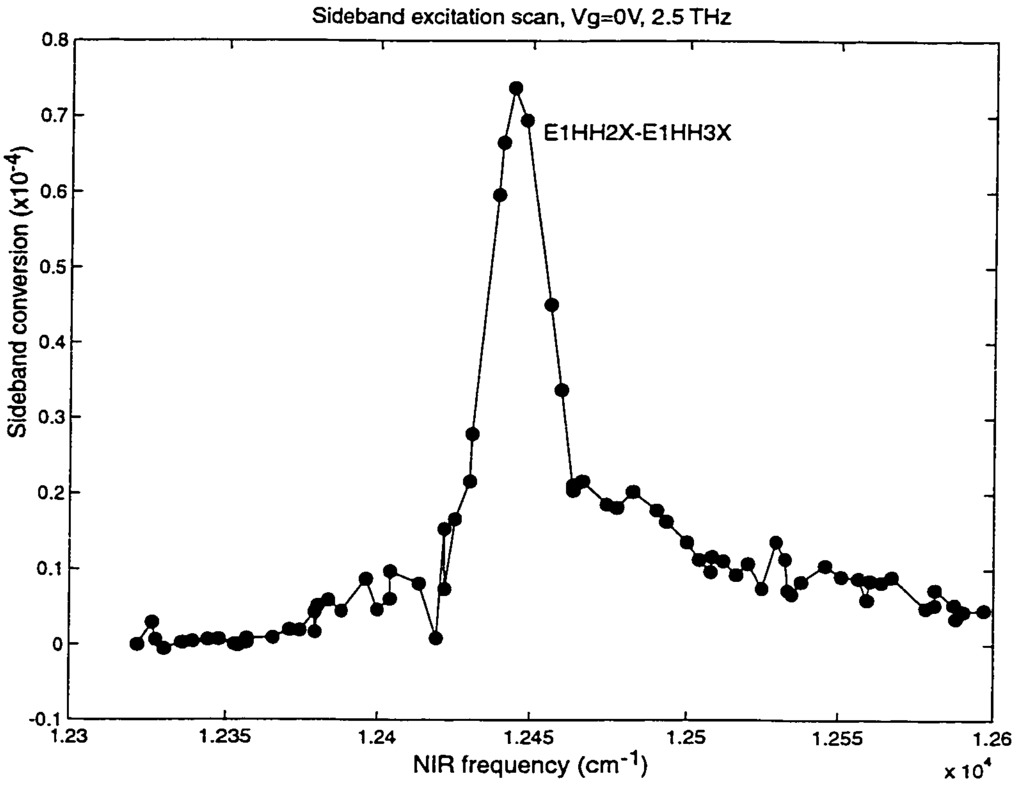

Figure 4.4: Sideband excitation scan at $V_g = 0$ V and $\omega_{THz} = 2.5$ THz (8.2 meV). Peak assignments are derived from theory.

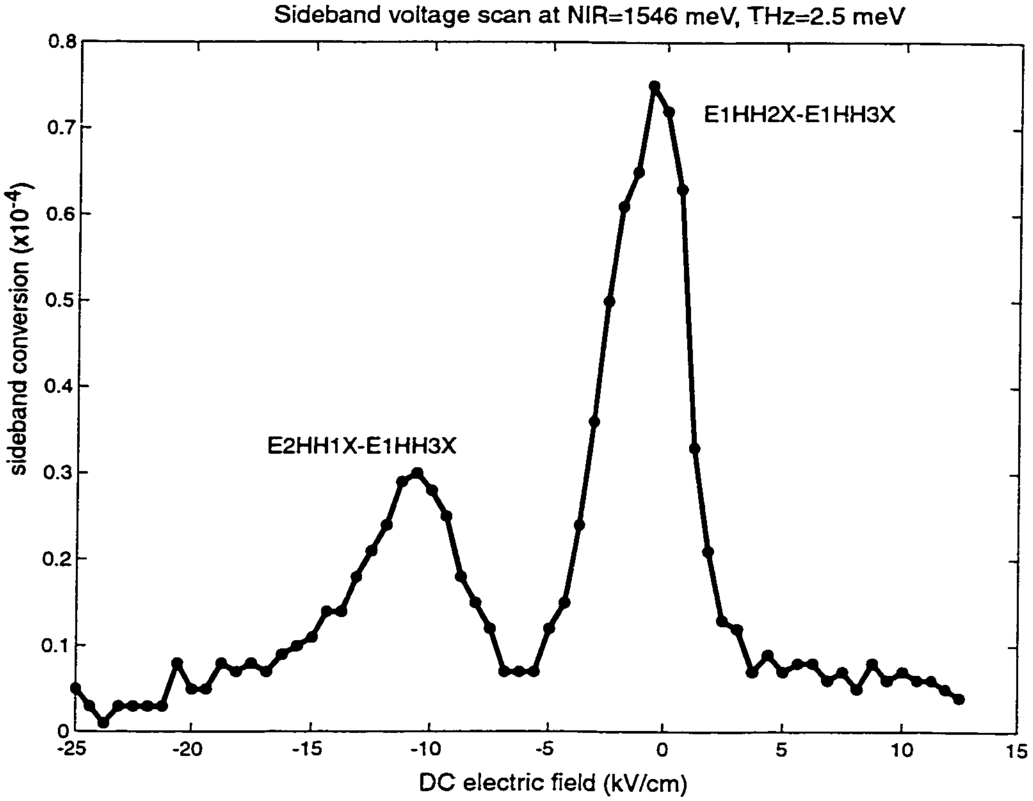

Figure 4.5: Sideband voltage scan at $\omega_{NIR} = 1546$ meV and $\omega_{THz} = 2.5$ THz (8.2 meV). Peak assignments are derived from theory.

shown in Figs. 4.6-4.8 at ω_{THz} =2.5 THz, 2.0 THz, and 1.9 THz (10.4 meV, 8.2 meV, 6.2 meV). The peaks in the sideband emission occur when the NIR field is resonant with an exciton and the THz field resonantly couples two excitons. Again, some of the distinct features are labelled with excitonic transition assignments derived from the theory described in the next section.

4.2 Theory

4.2.1 Virtual transitions

Because of the measured selection rules and power dependence, the THz modulation of the NIR probe which leads to sideband generation can be best understood as a parametric three-wave mixing process in which the THz field mixes with the NIR field via an optical nonlinearity to produce the sideband field. In a *parametric* nonlinear optical process Fig. 4.9a. the initial and final states are the same[27]. The intermediate photon transitions exist occur only for a short time within the Heisenberg uncertainty limit, $\Delta t \approx \hbar/\Delta E$ where ΔE is the detuning of the photon energy from the level spacings in the system[28]. These are called *virtual transitions* and the dotted lines are *virtual states* .

The initial state need not be lower than the virtual states, as illustrated in Fig. 4.9b,c. The strength of the different processes are weighted by the populations of the different initial states. However, since the DQW is undoped, there is only one possible initial state, which is the vacuum with no electrons and holes. From the vacuum, the NIR field creates a virtual exciton, which undergoes a THz intersubband virtual transition, then emits a sideband upon its annihilation.

I emphasize the idea of virtual transitions here because it is important to note that the THz modulation is *not* due to the actual motion of real carriers at THz fre-

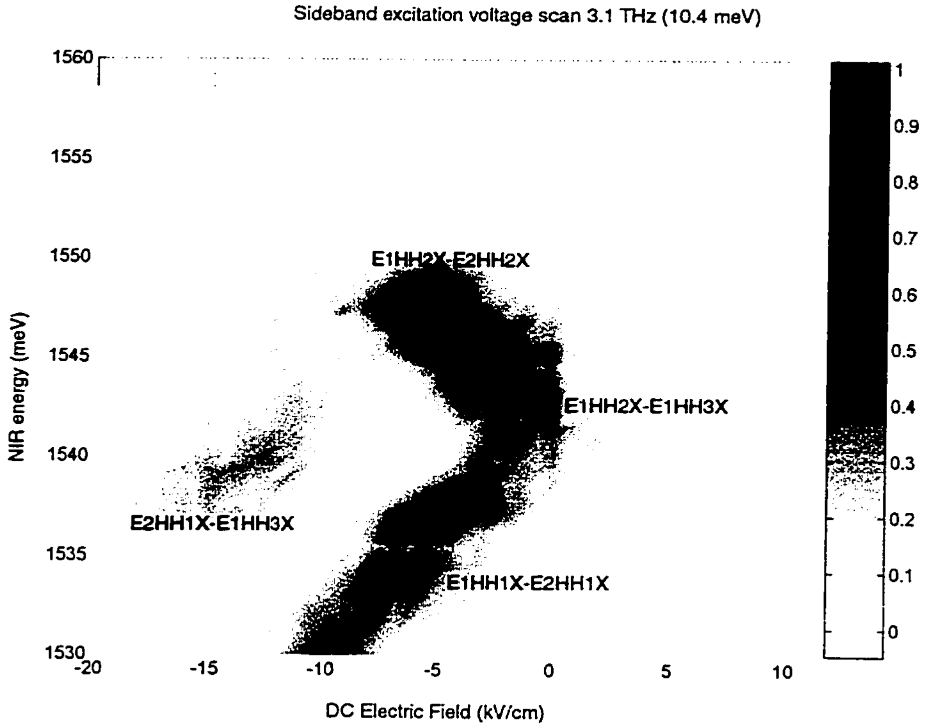

Figure 4.6: Sideband excitation voltage scan at $\omega_{THz} = 3.1$ THz (10.4 meV).

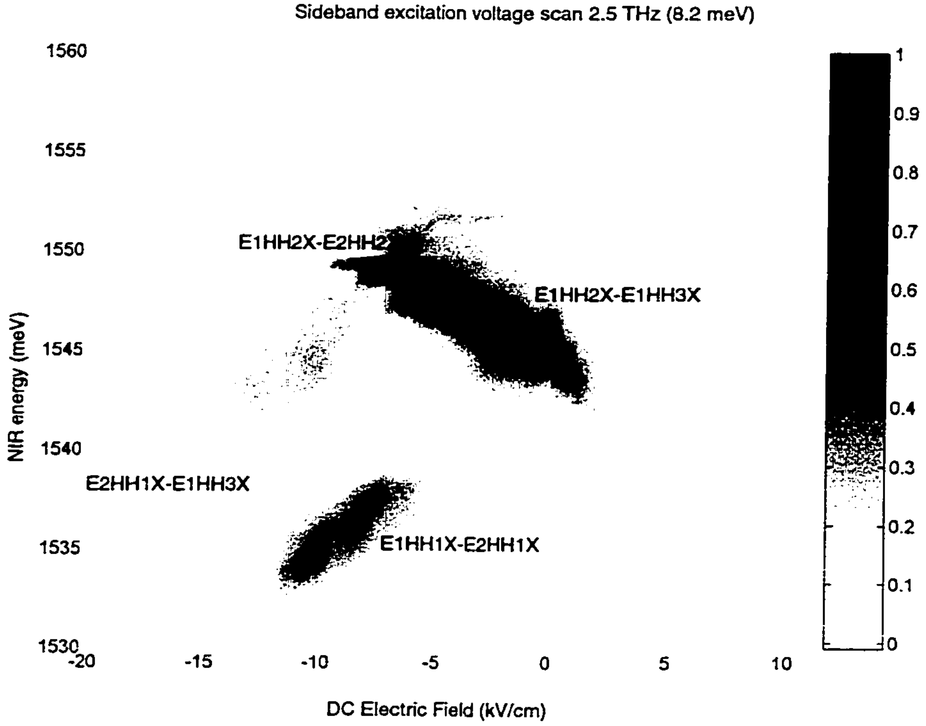

Figure 4.7: Sideband excitation voltage scan at $\omega_{THz} = 2.5$ THz (8.2 meV).

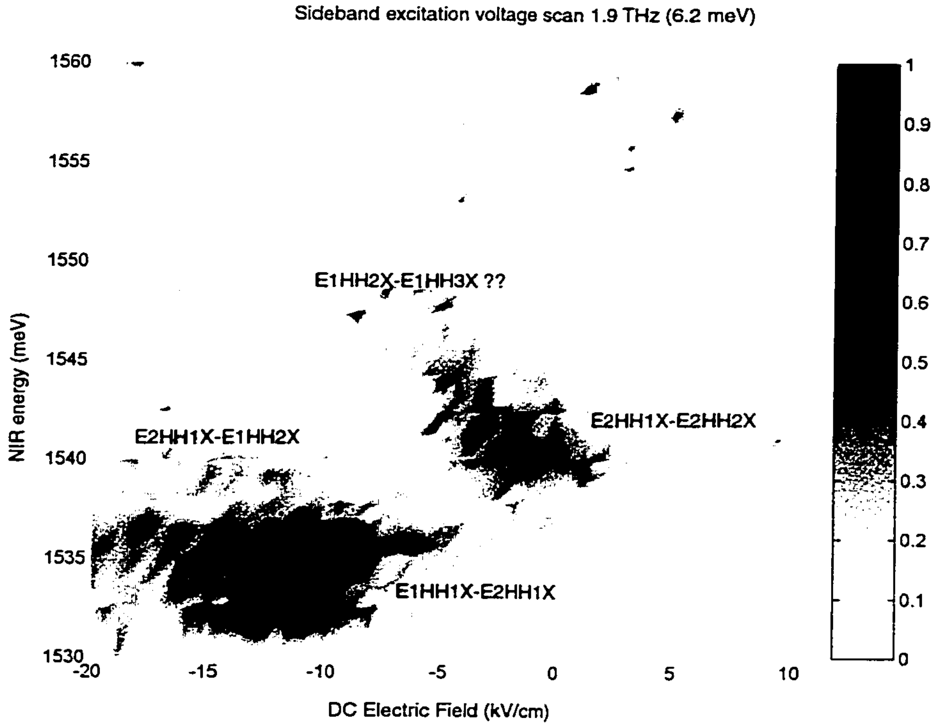

Figure 4.8: Sideband excitation voltage scan at $\omega_{THz} = 1.9$ THz (6.2 meV). The question marks label a resonance predicted by theory that did not appear in the data.

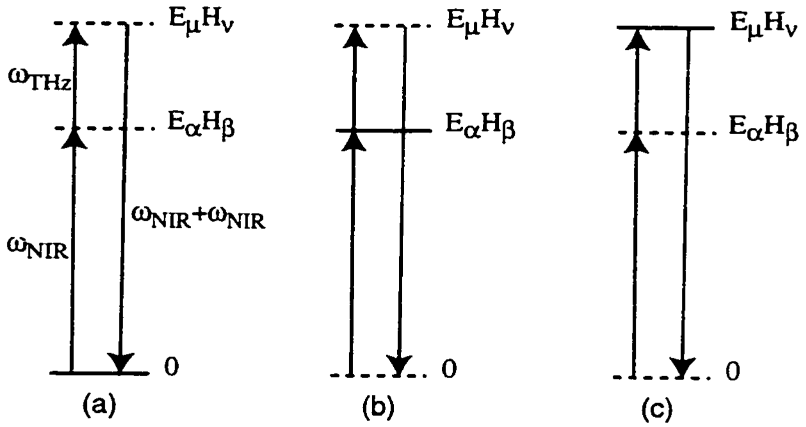

Figure 4.9: Virtual transitions. The initial state need not be lower than the virtual states (b,c). The strength of the individual contributions from (a-c) are determined by the relative populations of the real states. In our undoped system only (a) contributes to the sideband.

quencies. There have been numerous studies of THz nonlinear optical processes in doped semiconductors where electrons actually slosh about, such as THz harmonic generation and THz Bloch oscillation. In our undoped case, we start out with no carriers. The deed is done instantaneously, leaving us back to the initial ground state with no carriers.

Of course there are some real carriers present due to some absorption of the NIR beam. But the population can be made arbitrarily small by using a low intensity. Indeed, at the experimental excitation intensity ≈ 50 W/cm^2, the maximum carrier density is 10^9 cm^2 (based on a exciton recombination time of 300 ps), and there was a sideband even when the ω_{NIR} was below the band gap. Clearly the only significant population in the system is that of the filled valence band.

4.2.2 Nonlinear susceptibility I: excitons only

The macroscopic polarization of the quantum well in response to the total applied E-fields $E = E_{THz} + E_{NIR}$ can given by the Taylor expansion

$$P = \epsilon_0 \chi^{(1)} E + \epsilon_0 \chi^{(2)} E^2 + \epsilon_0 \chi^{(3)} E^3 + ... \tag{4.2.1}$$

near $E = 0$, that is, for weak optical fields. The linear susceptibility $\chi^{(1)}$ was calculated in Sec. 3.2. The three-wave mixing component is described by the second-order nonlinear optical susceptibility tensor $\chi^{(2)}(\omega_{THz} + \omega_{NIR}; \omega_{THz}, \omega_{NIR})$ which can be calculated by solving for the $\omega_{THz} + \omega_{NIR}$ frequency component of the dipole expectation value $e\langle r(t) \rangle$, where

$$\vec{r} = \vec{r}_e - \vec{r}_h$$

and $\vec{r}_e$ ($\vec{r}_h$) is the vector position operator for the electron (hole). The time-dependent Hamiltonian including optical fields is

$$H = H_0 + e\vec{r} \cdot (\vec{E}_{THz} \cos \omega_{THz} t + \vec{E}_{NIR} \cos \omega_{NIR} t) \tag{4.2.2}$$

where H_0 is the exciton Hamiltonian (3.2.1). Since the THz field is z-polarized while the NIR field is x-polarized, $\vec{E}_{THz} = E_{THz} \hat{z}$ and $\vec{E}_{NIR} = E_{NIR} \hat{x}$. Therefore (4.2.2) becomes

$$H = H_0 + e(z_e - z_h) E_{THz} \cos \omega_{THz} t + e(x_e - x_h) E_{NIR} \cos \omega_{NIR} t \tag{4.2.3}$$

Note that the optical fields only couple to the *relative* motion of the electron and hole, not the center-of-mass. Second-order time-dependent perturbation theory in the rotating wave approximation (RWA) readily leads to the following expression for the $\chi^{(2)}$:

$$\chi^{(2)}_{ex}(\omega_{THz} + \omega_{NIR}; \omega_{THz}, \omega_{NIR}) =$$

$$\frac{N_0}{\epsilon_0 \hbar^2} \sum_{\alpha\beta} \sum_{\mu\nu} \frac{F_{\alpha\beta} F_{\mu\nu} \mu_{\alpha\beta\mu\nu}}{[(\omega_{\alpha\beta} - \omega_{NIR} - \omega_{THz}) - i\gamma_{\alpha\beta}][(\omega_{\mu\nu} - \omega_{NIR}) - i\gamma_\mu \nu]} \tag{4.2.4}$$

Where $F_{\alpha\beta}$ ($F_{\mu\nu}$) is the oscillator strength and $\hbar\omega_{\alpha\beta}$ ($\hbar\omega_{\mu\nu}$) is the energy for the $\mathrm{E}_\alpha\mathrm{H}_\beta\mathrm{X}$ ($\mathrm{E}_\mu\mathrm{H}_\nu\mathrm{X}$) exciton state. The γ term is the same phenomenological linewidth used to calculate $\chi^{(1)}$.

4.2.3 Excitonic intersubband dipole

The term $\mu_{\alpha\beta\mu\nu}$ is the $(z_e - z_h)$ dipole moment between excitons $\mathrm{E}_\alpha\mathrm{H}_\beta\mathrm{X}$ and $\mathrm{E}_\mu\mathrm{H}_\nu\mathrm{X}$ and is given by

$$\mu_{\alpha\beta\mu\nu} = 2\pi \int dz_e \int dz_h \int \rho d\rho \phi_{\alpha\beta}(\rho, z_e, z_h)(z_e - z_h)\phi_{\mu\nu}(\rho, z_e, z_h) \tag{4.2.5}$$

where ϕ is the exciton wavefunction (3.2.7) solved in Chapter 3.

It is important to realize that $\mu_{\alpha\beta\mu\nu}$ is not the conventional intersubband dipole moment (see Fig. 4.10). For example, in a n-doped quantum well, z-polarized light couples to the electron intersubband dipole moment

$$\mu = \int f_\alpha(z_e) z_e f_\mu(z_e) dz_e \tag{4.2.6}$$

where f is the single-particle electron wavefunction solution to (3.2.2). Rather, $\mu_{\alpha\beta\mu\nu}$ is an *excitonic intersubband dipole*, since it couples the *excitons* associated with two electron-hole subbands.

The resonance conditions are illustrated in Fig 4.11. If either the $\hbar\omega_{sideband}$ or the $\hbar\omega_{NIR}$ is equal to the interband exciton energy, then the mixing is resonantly enhanced. A double-resonance condition occurs when $\hbar\omega_{NIR}$ is resonant with the interband exciton energy and $\hbar\omega_{THz}$ is resonant with the excitonic intersubband transition.

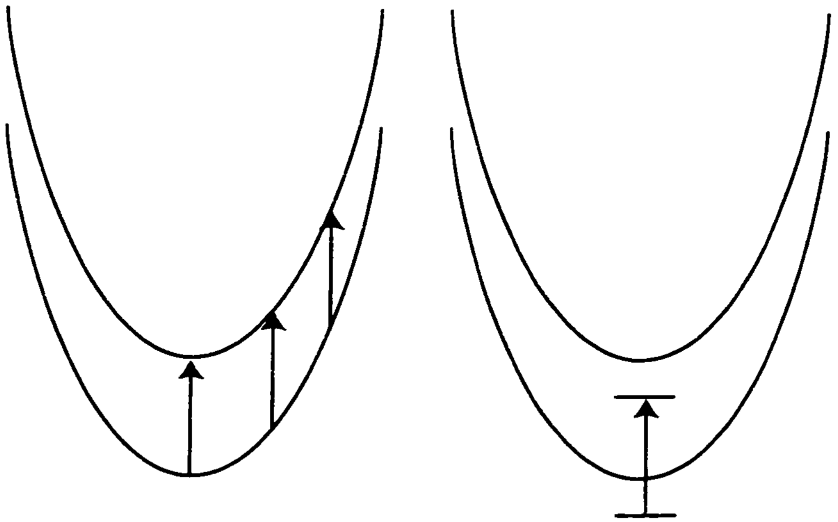

Figure 4.10: LEFT: The free electron intersubband transition. RIGHT: The excitonic intersubband transition.

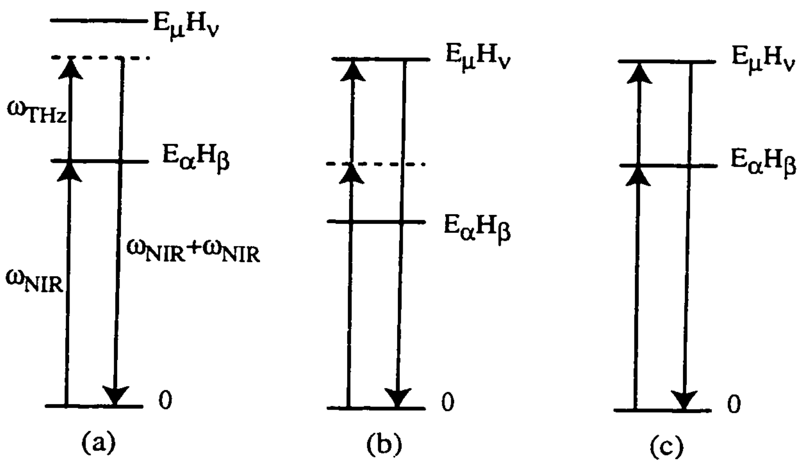

Figure 4.11: The two single-resonance conditions (a,b) are equally strong poles. The double-resonance (c) corresponds to a resonant excitonic intersubband condition.

4.2.4 Exciton theory vs. experiment

I numerically calculated $\chi_{ex}^{(2)}$ as a function of ω_{NIR}, ω_{THz}, and V_g at the same values as the experimental scans. The values of $\left|\chi_{ex}^{(2)}\right|^2$ are shown in Figs. 4.12, 4.13, and 4.14.

Although there are clear discrepancies, the simple exciton model captures most of the features in the experiment and illuminates the physical processes involved in the THz modulation of the NIR beam. In particular, the $\chi^{(2)}$ calculation allows us to assign the features with specific excitonic intersubband transition labels. The peak assignments were obtained by running the calculation with different states omitted, until the peak disappeared. So if E1HH1X and E2HH1X are omitted, and the peak in the $\chi^{(2)}$ disappears, then I labelled the peak E1HH1X-E2HH1X.

For closer comparison between theory and data, see Figs. 4.15,4.16.

4.2.5 Limitations of an excitonic theory

The disagreements between theory and data are probably due to states not accounted for in the model. Recall that the only states that are included in this model are the ground $1s$ exciton states for each subband $\mathrm{E}_\mu\mathrm{H}_\nu$. For each subband there is a spectrum of optically-active excited exciton states which are ignored. While the variational technique used in Chapter 3 was succesful in calculating the ground state $1s$ exciton wavefunctions, it is difficult to apply for excited states.

In addition, the form of the trial $1s$ wavefunction φ may not be adequate to accurately calculate the excitonic intersubband dipole μ. Recall that $\varphi_{\mu\nu} = \exp\left[\frac{-r}{R_{\mu\nu}}\right]$, which is spherically symmetric. Other workers[26] have used nonspherically-symmetric trial wavefunctions such as

$$\psi = \exp\left[-\sqrt{\rho^2 + \kappa(z_e - z_h)^2}/R\right] \qquad (4.2.7)$$

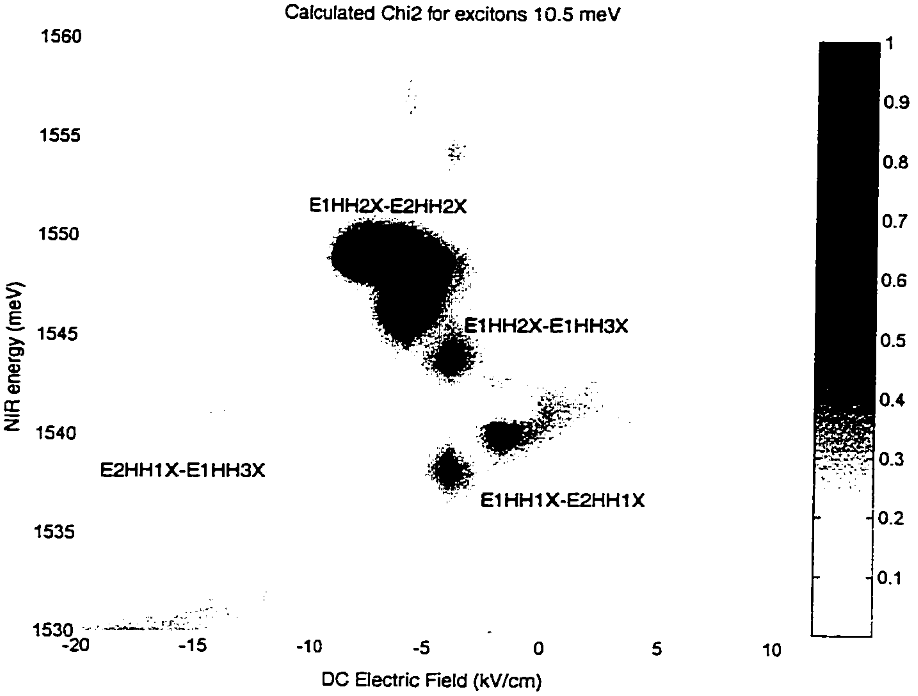

Figure 4.12: Excitonic theory $\omega_{THz} = 3.1$ THz. There are no fit parameters.

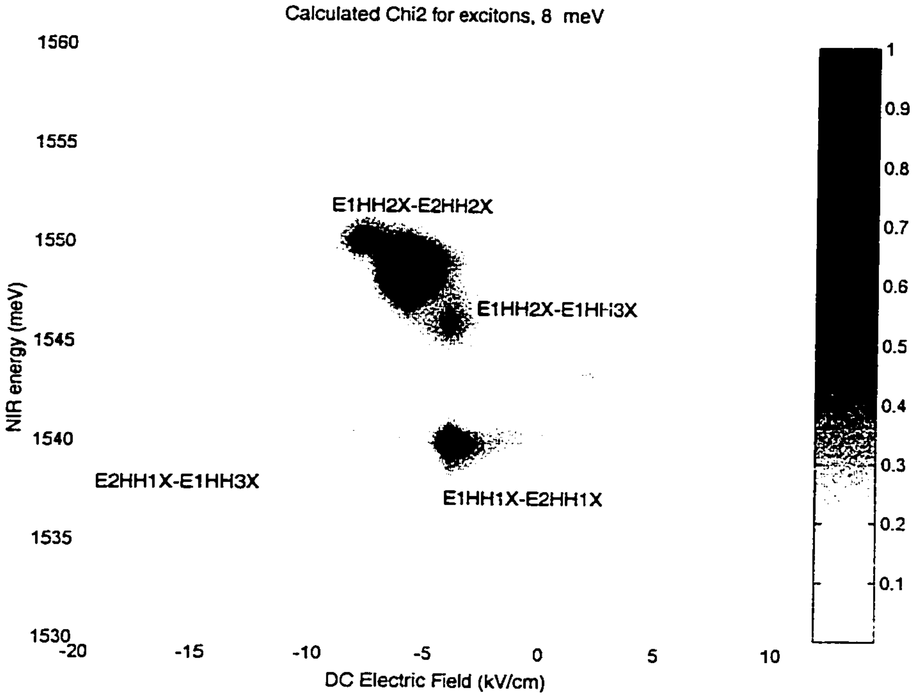

Figure 4.13: Excitonic theory $\omega_{THz} = 2.5$ THz. There are no fit parameters.

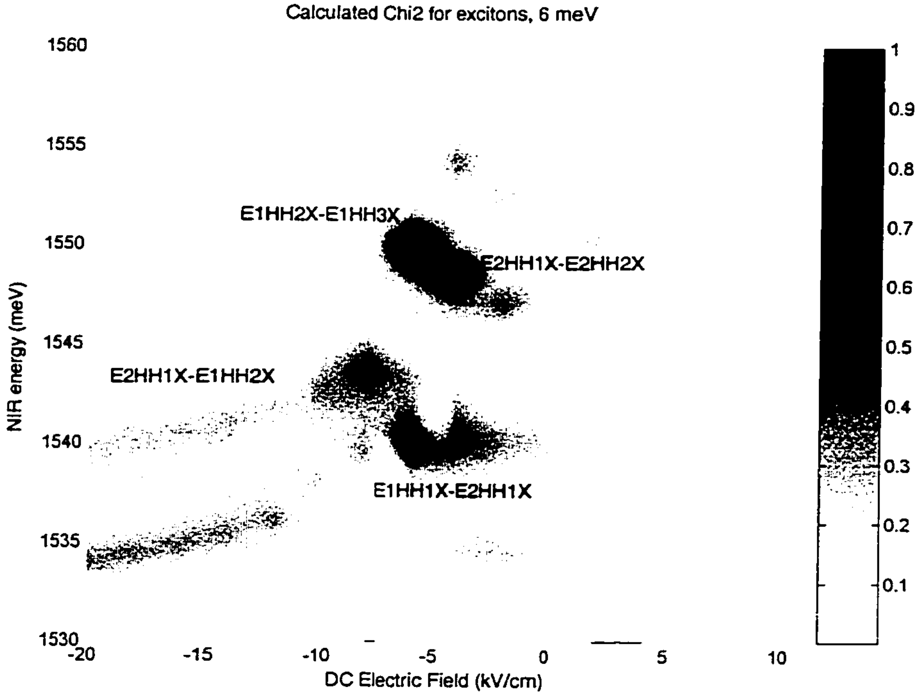

Figure 4.14: Excitonic theory $\omega_{THz} = 1.9$ THz. There are no fit parameters.

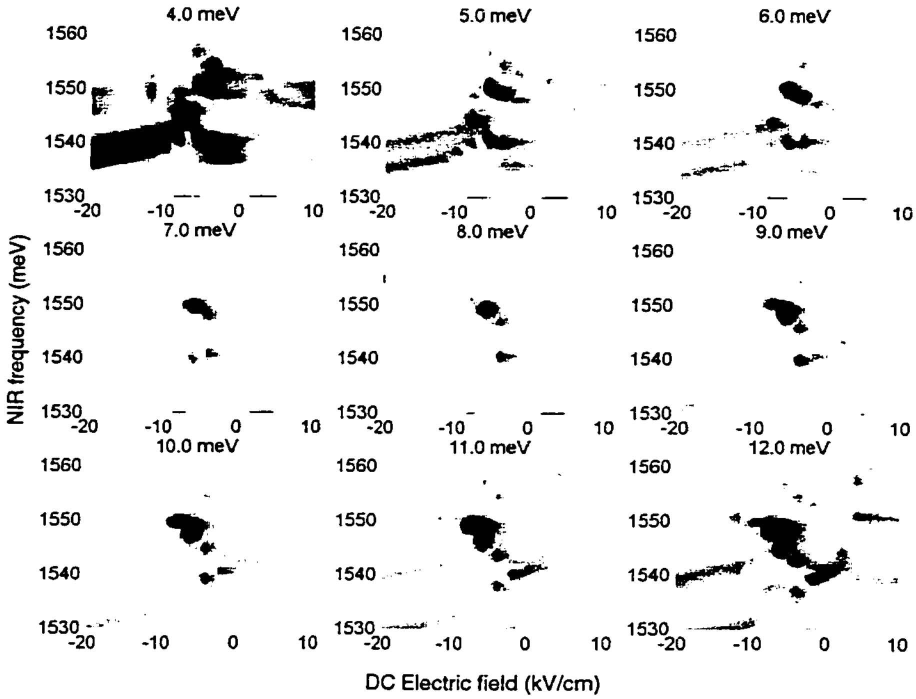

Figure 4.15: Excitonic theory, various ω_{THz}. There are no fit parameters

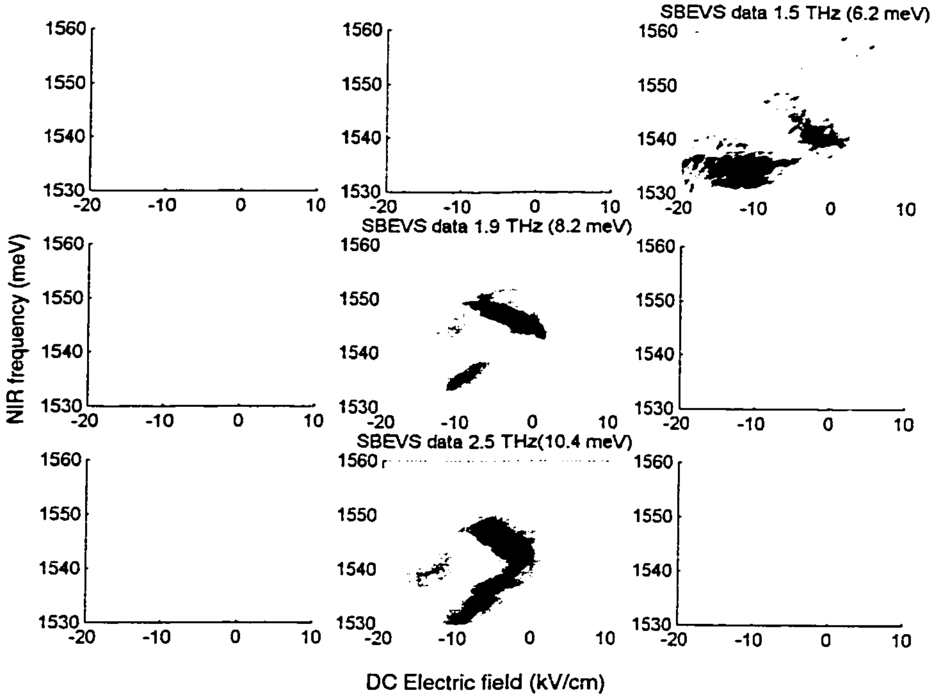

Figure 4.16: Sideband voltage excitation data.

with multiple variational parameters κ and R. Of course the variational calculation becomes more computationally difficult with additional parameters.

It will be very interesting to see how further refinements to the excitonic theory affect the quantitative agreement with experiment. At this point such an involved calculation is outside the scope of this experimental dissertation.

The most glaring omission in the pure exciton theory are the free electron-hole states. Their effect is examined in the next section.

4.2.6 Nonlinear susceptibility II: continuum

The discrete terms in summation expression (4.2.4) are not valid for the continuum of free electron-hole states. Including them in the nonlinear susceptibility requires an additional term integrating over the xy-plane k-space of electrons and holes[28]:

$$\chi_{fr}^{(2)}(\omega_{THz}+\omega_{NIR};\omega_{THz},\omega_{NIR}) =$$

$$\frac{1}{N_{\mu\nu}^2}\frac{N_0}{\epsilon_0\hbar^2}\sum_{\alpha\beta}\sum_{\mu\nu}\int_0^\infty \frac{F_{\alpha\beta}F_{\mu\nu}\mu_{\alpha\beta\mu\nu}^{fr}kdk}{[(\omega_{\alpha\beta}^{fr}(k)-\omega_{NIR}-\omega_{THz})-i\gamma_{\alpha\beta}][(\omega_{\mu\nu}^{fr}(k)-\omega_{NIR})-i\gamma_{\mu}\nu]} \tag{4.2.8}$$

where $\mu_{\alpha\beta\mu\nu}^{fr}$ is the $(z_e - z_h)$ dipole moment between subbands $\mathrm{E}_\alpha\mathrm{H}_\beta$ and $\mathrm{E}_\mu\mathrm{H}_\nu$ and is given by

$$e\langle E_\alpha H_\beta|(z_e - z_h)|E_\mu H_\nu\rangle$$

$$= e\langle E_\alpha|z_e|E_\mu\rangle\langle H_\beta|H_\nu\rangle - e\langle H_\beta|z_h|H_\nu\rangle\langle E_\alpha|E_\mu\rangle$$

$$= \int_{-\infty}^{\infty} f_\alpha(z)zf_\mu(z)dz\int_{-\infty}^{\infty} g_\beta(z)g_\nu(z)dz - \int_{-\infty}^{\infty} g_\beta(z)zg_\nu(z)dz\int_{-\infty}^{\infty} f_\alpha(z)f_\mu(z)dz \tag{4.2.9}$$

since z_e acts only on electrons and z_h acts only on holes. The free electron-hole intersuband dipole is just the sum of the electron and hole intersubband dipoles weighted by the hole and electron overlaps, respectively.

4.2.7 Continuum theory vs. experiment

I numerically calculated $\chi^{(2)}$ as a function of ω_{NIR}, ω_{THz}, and V_g at the same values as the experimental scans. The values of $\left|\chi^{(2)}_{fr}\right|^2$ are shown in Figs. 4.17, 4.18, and 4.19.

The purely excitonic theory is in far better agreement than the continuum theory. The peaks positions in the continuum theory as a function of ω_{THz} do not even qualitatively compare to the data. The linewidths predicted in the continuum theory are very broad, which is not surprising. The peaks in the data are quite narrow, which is the feature that motivated the excitonic analysis in the first place!

Clearly, excitonic effects dominate the THz-NIR mixing. It is possible that the free electron-hole states do not contribute to the mixing at all! However, it will be very interesting to see how including Coulomb correlations between free electrons and holes affect the quantitative agreement with experiment. Again, such an involved calculation is outside the scope of this experimental dissertation.

Figure 4.17: Continuum theory $\omega_{THz} = 3.1$ THz.

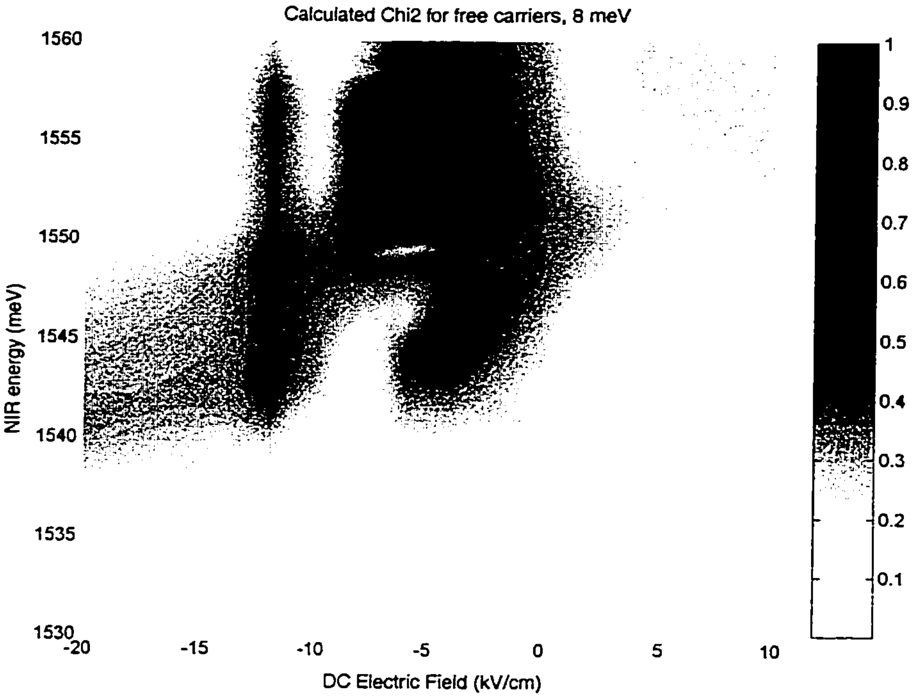

Figure 4.18: Continuum theory $\omega_{THz} = 2.5$ THz.

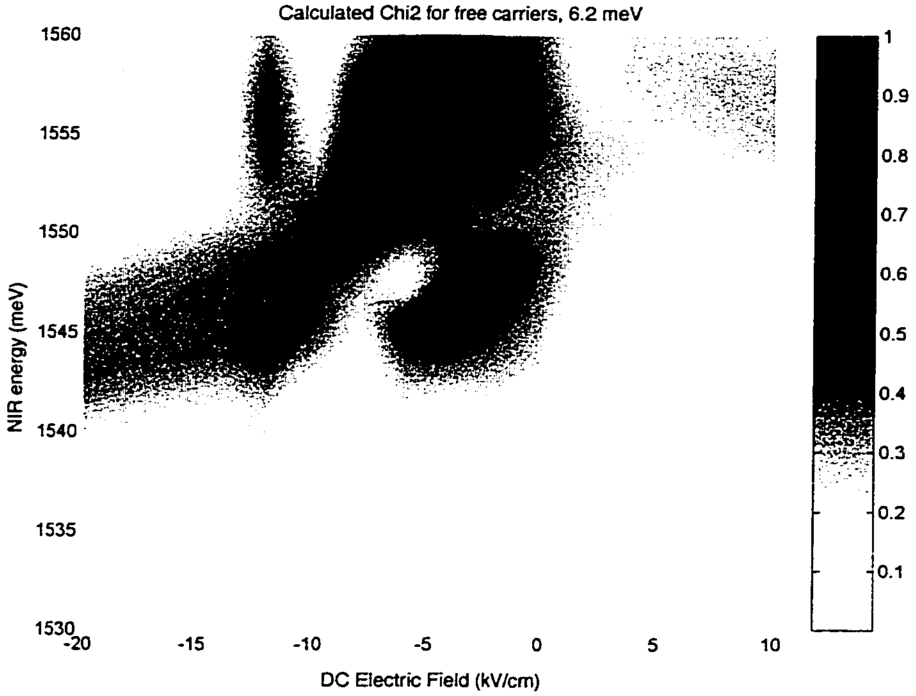

Figure 4.19: Continuum theory $\omega_{THz} = 1.9$ THz.

Chapter 5

Nonperturbative THz nonlinear optics of DQW excitons

Driving an DQW excitonic intersubband resonance with a THz electric field of frequency ω_{THz} generates terahertz optical sidebands $\omega = \omega_{THz} + \omega_{NIR}$ on a weak NIR probe. The previous chapter described resonance measurements in a regime where THz field was a weak perturbation on the exciton states.

At high terahertz intensities, the electric dipole energy which couples two excitons is comparable to the photon energy. In this strong-field regime the sideband intensity displayed an unusual non-monotonic dependence on the THz field strength. The oscillating refractive index which gives rise to the sidebands may be understood by the formation of *Floquet states*, which oscillate with the same periodicity as the driving terahertz field.

5.1 Experimental results

As I explained in the introduction, a major basic physics perk for studying the THz field strength dependence of sideband generation in quantum wells is the chance to experimentally probe the effect of a very strong resonant laser field on a quantum system. There is a rich body of theoretical predictions on the effect of strong THz fields on the *bound* states of a quantum well. These predictions include shifts and splittings in absorption lines as well as non-monotonic power dependences of nonlinear mixing.

Monitoring changes in absorption features turns out to be a sub-optimal method for probing strong-field physics in intersubband excitations. Absorption shifts which are less than the linewidth are difficult to resolve within a 1 MHz measurement bandwidth. Components of the THz field lying in the xy-plane can cause shifts which complicate analysis. Indeed, the strongest sidebands were observed when THz-induced changes in PL were minimized.

On the other hand, the $n = 1$ sideband is an ideal probe. It is a zero-background measurement in two respects: there is no sideband when the THz pulse is not present, and there is no contribution to the sideband from any THz polarization component which is not in the z-direction.

The experiments described in the previous chapter were performed on a waveguide device with no sapphire. As described in Sec 2.3.5, in this configuration the sidebands are generated a weak evanescent THz field near the air-semiconductor interface. In addition the THz intensity was attenuated by about $1/2$ of full available power.

The THz power can be continuously varied by a pair of wire-grid polarizers. A typical THz power dependence of the $n = 1$ and $n = 2$ sidebands is shown in Fig. 5.1. The $n = 1$ sideband is linearly dependent on THz power while the $n = 2$ has a

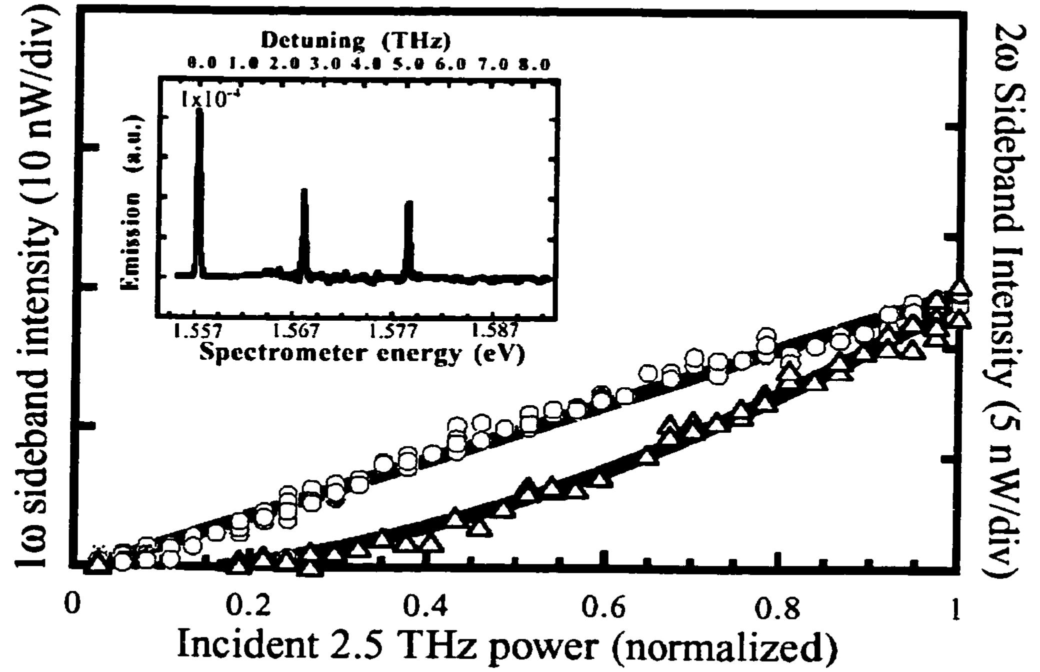

Figure 5.1: Low field strength THz power dependence of $n = 1$ and $n = 2$ sidebands.

quadratic dependence. This agrees with previous studies and is consistent with the nonlinear susceptibility model described in the previous chapter.

The THz electric field strength at the active region can be increased using the waveguide device with sapphire pressed on the front surface. This places the active region in the center of the square dielectric waveguide, as described in Sec. 2.3.5.

Fig. 5.2 shows a series of sideband voltage scans at a several NIR frequencies at full THz power (1 kW). Note that the sideband voltage scans are not sensitive to ω_{NIR} near the peak NIR frequency. This is because at this particular resonance (E2HH2-E2HH3 at -1.25 kV/cm), the effect of the DC voltage is to tune the lower exciton state $|1\rangle$ while the upper state $|1\rangle$remains relatively unchanged. (see Fig.

5.3). Thus the sideband is always resonant with an exciton at a particular ω_{NIR} and ω_{THz}, the resonance condition illustrated in Fig. 4.11b. Changing the electric field at this point tunes the excitonic intersubband transition into resonance with the THz field.

By sitting at the peak NIR frequency for E2HH2-E2HH3 and varying the DC gate voltage we can take THz power dependence scans at various THz detunings $E_2 - E_1 - \hbar\omega_{THz}$ where E_2 (E_1) is the energy of the upper (lower) exciton state. The results are shown in Fig. 5.4. The most striking feature is the nonmonotonic dependence of the sideband on THz power near the resonant voltage. As the detuning is varied, so does the curvature of the power dependence. A corollary is that the sideband intensity always saturates.

5.2 Theory

The power dependence cannot be explained by a nonlinear susceptibility, which is inherently a low-field theory because it relies on a Taylor expansion about the field strength ([27]). Saturation effects[29] in a nonlinear susceptibility can only come about when contributions from the virtual transitions illustrated in Fig. 4.9b,c are comparable to that of Fig. 4.9a. However the populations of excited states $|1\rangle$ or $|2\rangle$ are never significant compared with $|0\rangle$ in our undoped sample and weak NIR beam. Therefore a nonlinear susceptibility can only predict a strictly linear power dependence.

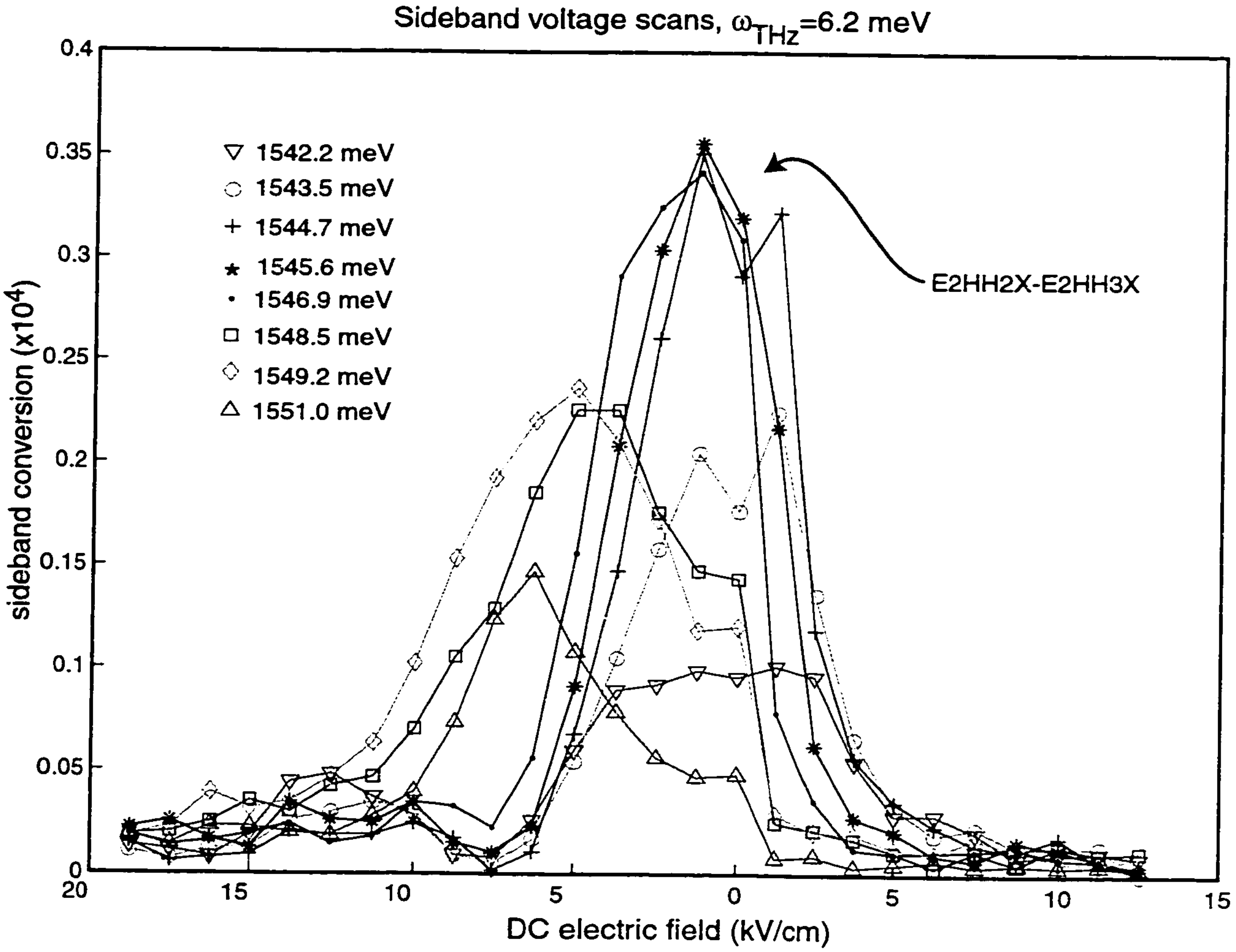

Figure 5.2: Sideband voltage scans at a series of NIR frequencies at full THz power for ω_{THz}=1.9 THz (6.2 meV). Near the labeled resonance E2HH2-E2HH3 the sideband becomes relatively insensitive to the exact ω_{NIR}.

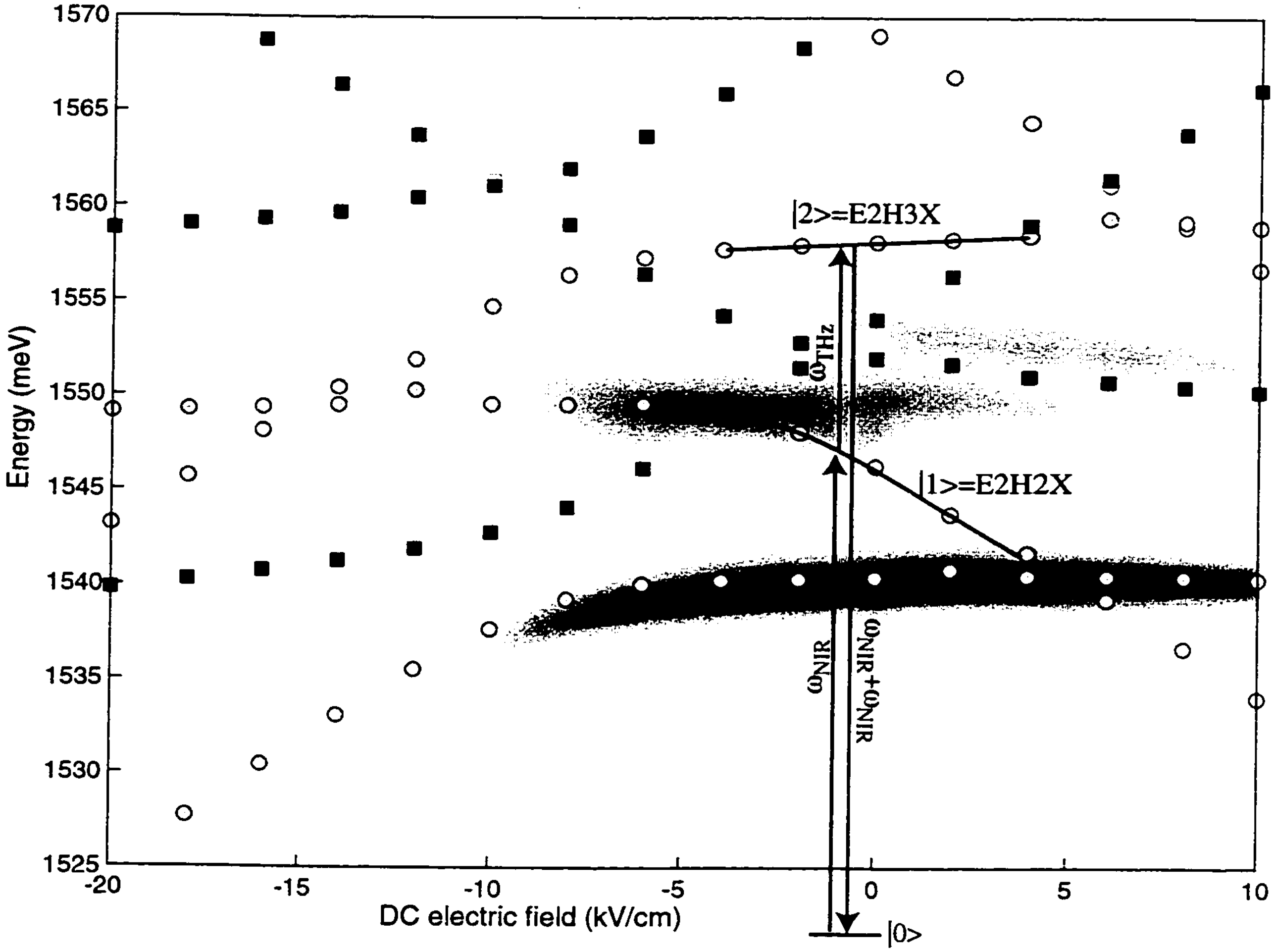

Figure 5.3: Figure 3.14 annotated to illustrate the effect of the electric field near the E2HH2-E2HH3 resonance around -1.25 kV/cm. The DC field linearly tunes E2HH2 while E2HH3 remains constant. Thus the sideband is always resonant with an exciton at a particular ω_{NIR} and ω_{THz}. Changing the electric field at this point tunes the excitonic intersubband transition into resonance with the THz field.

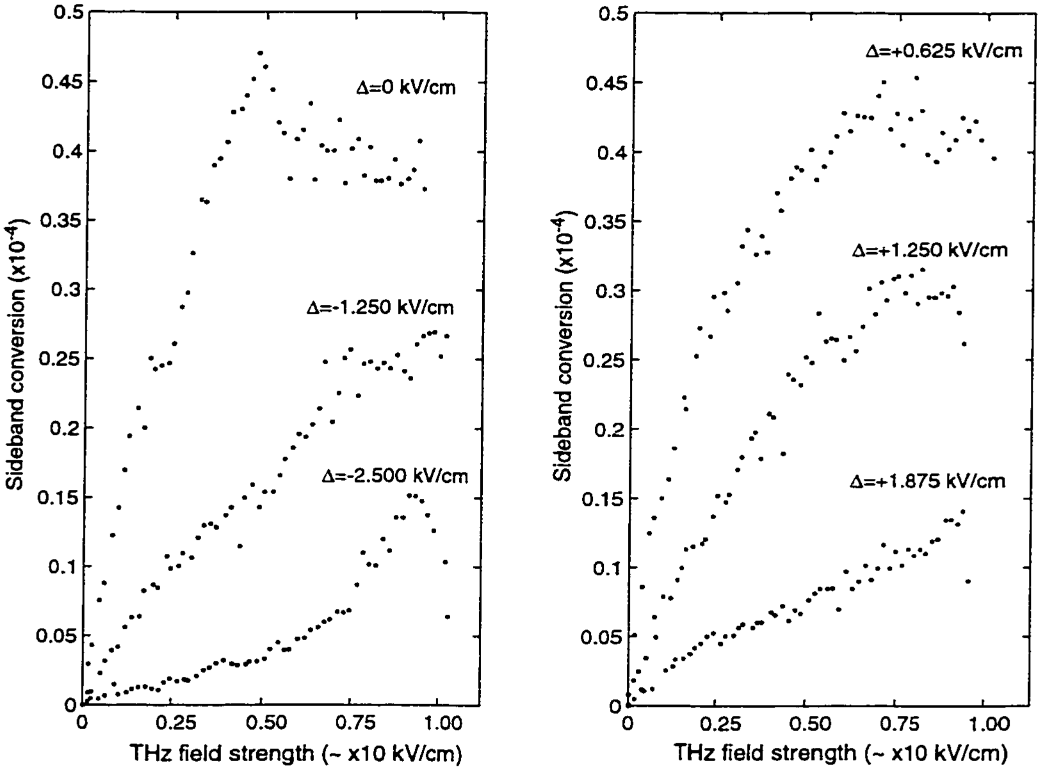

Figure 5.4: THz power dependence of $n = 1$ sideband at various DC electric field detunings from the double-resonance condition illustrated in Fig. 5.3. ω_{NIR}=1545 meV. The estimate of the THz electric field strength is only accurate to within a factor of 2.

5.2.1 Floquet formalism

Consider a stationary Hamiltonian H_0 with eigenstates $\phi_\alpha(z)e^{-iE_\alpha t/\hbar}$, driven by a time-periodic interaction so that the total Hamiltonian is

$$H = H_0 + \mu \cdot \cos\omega t \tag{5.2.1}$$

where μ is the interaction operator. The solutions to the Schrodinger equation for the time-periodic Hamiltonian have the form[30]

$$\varphi_i(z,t) = e^{-i\epsilon_i t/\hbar} u_i(z,t) \tag{5.2.2}$$

$$u(z,t) = u(z, t + \frac{2\pi}{\omega}) \tag{5.2.3}$$

where $u_i(z,t)$ has the same periodicity as the driving frequency and and ϵ_i is called the *quasienergy*. The states $\varphi_i(z,t)$ are called *Floquet states* and are mathematically analogous to Bloch states for a spatially-periodic Hamiltonian. Meanwhile the quasienergies are analogous to the crystal momenta of Bloch theory.

The spatial-dependence of the wavefunction $\varphi_i(z,t)$ can be expanded in terms of the original eigenstates $\phi_\alpha(z)$, and the time-dependence can be Fourier-expanded

$$\varphi_i(z,t) = e^{-i\epsilon_i t/\hbar} \sum_{\alpha,n} c^i_{\alpha,n} e^{-in\omega t} \phi_\alpha(z) \tag{5.2.4}$$

The coefficients[1] $c^i_{\alpha,n}$ are what will determine the part of the index of refraction which will oscillate at particular multiples of ω. Solving for these coefficients is the key to understanding the power dependence of the sideband. It is interesting to note that Floquet coefficients are closely related to the photon-assisted tunneling sidebands which appear in the irradiated current-voltage curves in superconducting weak-link junctions and double quantum wells.

---

[1] The expansion is not unique. Note that the substitution $\epsilon_i \to \epsilon_i + l\hbar\omega$, $c^i_{\alpha,n} \to c^i_{\alpha,n+l}$ results in the same Floquet state. A particular expansion is called the lth-photon representation, where the $l = 0$ representation is defined such that as $\mu \to 0$, $\epsilon_i \to E_i$, and $c^i_{i,0} \to 1$. We always use the 0-photon representation.

The time-dependent Schrodinger equation can be cast in the form

$$Fw_i(z,t) = \epsilon_i w_i(z,t) \tag{5.2.5}$$

where F is the *Floquet operator*

$$F = H - i\hbar\frac{\partial}{\partial t} \tag{5.2.6}$$

The Floquet operator can be written as a matrix of the form[7]

$$F = \begin{pmatrix} \ddots & [\mu] & 0 & 0 & 0 & 0 & 0 \\ \mu & [H_0]-2\hbar\omega & [\mu] & 0 & 0 & 0 & 0 \\ 0 & [\mu] & [H_0]-\hbar\omega & [\mu] & 0 & 0 & 0 \\ 0 & 0 & [\mu] & [H_0] & [\mu] & 0 & 0 \\ 0 & 0 & 0 & [\mu] & [H_0]+\hbar\omega & [\mu] & 0 \\ 0 & 0 & 0 & 0 & [\mu] & [H_0]+2\hbar\omega & [\mu] \\ 0 & 0 & 0 & 0 & 0 & [\mu] & \ddots \end{pmatrix} \tag{5.2.7}$$

where $[H_0]$ and $[\mu]$ are matrix representations of the operators H_0 and μ in the $|\phi_\alpha\rangle$ basis. In practice the Floquet matrix must be truncated up to $\pm N$ photons. N can be made arbitrarily large for an arbitrarily precise result at high field strengths. The complete solution to the Schrodinger equation for a time-periodic Hamiltonian just reduces to finding the eigenvalues and eigenvectors of the Floquet matrix (5.2.7). Other than the $\pm N$ truncation the solution involves no perturbation or rotating-wave approximations. For the calculations in this chapter we use $N = 16$ photons.

5.2.2 Three-state toy model

I try to capture the qualitative features of the sideband power dependence with a toy three-state system. The Hamiltonian H_0 has eigenstates $\phi_0(x,z)$, $\phi_1(x,z)$, and $\phi_2(x, z)$ with eigenenergies $E_0 = 0$, E_1, and E_2, respectively. The two upper states $\phi_1(x, z)$ and $\phi_2(x, z)$ are coupled by the z-dipole operator. The two upper states $\phi_1(x, z)$ and $\phi_2(x, z)$ are coupled to the ground state by the x-dipole operator. Finally, a DC electric field applied in the z-direction linearly tunes only the highest state. Therefore, the x and z matrices are

$$z = \begin{pmatrix} 0 & 0 & 0 \\ 0 & 0 & z_{12} \\ 0 & z_{21} & z_{22} \end{pmatrix}$$

$$x = \begin{pmatrix} 0 & x_{01} & x_{02} \\ x_{10} & 0 & 0 \\ x_{20} & 0 & 0 \end{pmatrix}$$

All the nonzero terms $x_{\alpha\beta} = \langle\phi_\alpha|x|\phi_\beta\rangle$ and $z_{\alpha\beta} = \langle\phi_\alpha|z|\phi_\beta\rangle$ are set equal to unity. The Hamiltonian is

$$H = H_0 + zE_\omega \cos\omega t + x\lambda E_\Omega \cos\Omega t \tag{5.2.8}$$

where E_ω represents the strong THz electric field strength and E_Ω represents the weak NIR electric field. The strategy for solving the two-frequency system goes like this: The Hamiltonian will be solved nonperturbatively with Floquet states for $\lambda = 0$, while the weak probe is added later using time-dependent perturbation theory.

The Floquet solutions are labeled $\varphi_i(x, z, t)$ with $i = 0, 1, 2$, and expanded as in (5.2.4). Their expansions are explicitly expressed for clarity:

$$\begin{aligned} \varphi_0(x, z, t) &= \phi_0(x, z) \\ \varphi_1(x, z, t) &= e^{i\epsilon_1 t/\hbar} \sum_n e^{-in\omega t}[c^1_{1,n}\phi_1(x, z) + c^1_{2,n}\phi_2(x, z)] \\ \varphi_2(x, z, t) &= e^{i\epsilon_2 t/\hbar} \sum_n e^{-in\omega t}[c^2_{1,n}\phi_1(x, z) + c^2_{2,n}\phi_2(x, z)] \end{aligned}$$

The ground state $\phi_0(x, z)$ is not coupled by the the strong field to the 2-d subspace spanned by $|\phi_1\rangle$ and $|\phi_2\rangle$. Therefore the coefficients for the Floquet state $\varphi_0(x, z, t)$ vanish except $c^0_{0,0} = 1$. In otherwords, the ground vacuum state remains untouched by the intense THz field.

5.2.3 Weak perturbative probe

I used 1st-order time-dependent perturbation theory to calculate the dipole response to the Floquet states to the weak NIR probe. The state of the system with both driving fields $\psi(x, z, t)$ can be expanded in terms of the Floquet states $\varphi_i(x, z, t)$ to first order:

$$\psi(x, z, t) = \psi^{(0)} + \lambda\psi^{(1)} \tag{5.2.9}$$

where

$$\psi^{(0)}(x, z, t) = \varphi_0(x, z, t) \tag{5.2.10}$$

$$\psi^{(1)}(x, z, t) = E_\Omega e^{-i\Omega t} \sum_{i=1}^{2} \frac{\langle\varphi_i|x|\varphi_0\rangle}{\epsilon_i - \hbar\Omega} \varphi_i(x, z, t) \tag{5.2.11}$$

The polarization is proportional to the expectation value of the dipole

$$\begin{aligned} \langle\psi|x|\psi\rangle &= \langle\psi^{(0)}|x|\psi^{(1)}\rangle + \langle\psi^{(1)}|x|\psi^{(0)}\rangle \\ &= E_\Omega e^{-i\Omega t} \sum_{i=1}^{2} \frac{\langle\varphi_0|x|\varphi_i\rangle\langle\varphi_i|x|\varphi_0\rangle}{\epsilon_i - \hbar\Omega} + E_\Omega e^{+i\Omega t} \sum_{i=1}^{2} \frac{\langle\varphi_0|x|\varphi_i\rangle\langle\varphi_i|x|\varphi_0\rangle}{\epsilon_i + \hbar\Omega} \end{aligned} \tag{5.2.12}$$

Here we discard second-order terms. The second term is an anti-resonant contribution which we can also safely discard.

The form of the last expression is exactly the same as that for the linear susceptibility of an undriven system, except that the states φ_i are oscillating Floquet states instead of stationary states. Explicitly expanding the Floquet states in the dipole expectation values,

$$\langle\varphi_0|x|\varphi_i\rangle = e^{-i\epsilon_i t/\hbar} \sum_{n,\alpha} c^i_{n,\alpha} e^{-in\omega t} x_{0\alpha} \ . \tag{5.2.13}$$

Substituting (5.2.13) into (5.2.12), remembering to take complex conjugates, gives us the final expression for the polarization:

$$x(t) = E_{\Omega} e^{-i\Omega t} \sum_{i=1}^{2} \sum_{\substack{n,\alpha \\ m,\beta}} \frac{c^i_{n,\alpha} c^i_{m,\beta} e^{-i(n-m)\omega t} x_{0\beta} x_{\alpha 0}}{\epsilon_i - \hbar\Omega} \tag{5.2.14}$$

The $+1\omega$ sideband is given by the Fourier component of $x(t)$ oscillating at the frequency $\Omega+1\omega$. Also, for the resonant condition illustrated in Fig. 5.3, $\hbar\omega \approx \epsilon_1$, so we keep only the $i = 1$ term in the sum. This condition is satisfied when $n - m = 1$. Thus we obtain an expression for the sideband polarization

$$x_{sideband}(t) = \frac{E_{\Omega} e^{-i(\Omega+\omega)t}}{\epsilon_1 - \hbar\Omega} \sum_{n,\alpha,\beta} c^1_{n+1,\alpha} c^1_{n,\beta} x_{0\beta} x_{\alpha 0} \tag{5.2.15}$$

The intensity of the sideband is proportional to $x^2_{sideband}$. This is plotted vs. field strength for various detunings in Figs. 5.5 and 5.6. The detuning parameter d is just the level spacing normalized by the strong-field photon energy.

$$d = \frac{E2 - E1}{\hbar\omega} \tag{5.2.16}$$

5.3 Final discussion

It is remarkable that such a mindlessly simple toy model can capture the shapes of resonant power dependence of this complicated experiment up to field strengths of around $d \approx 1$. However I never was able to reach a field intensity to cause the sideband to disappear, which is a striking prediction of the theory.

I devoted a large amount of time pushing the experimental upper bound on the THz field strength. The dotted line is an estimate of what was reachable using the waveguide device. The goal of the antenna-coupled device was to push the field strengths well past a free-space diffraction limit by coupling the THz field into a

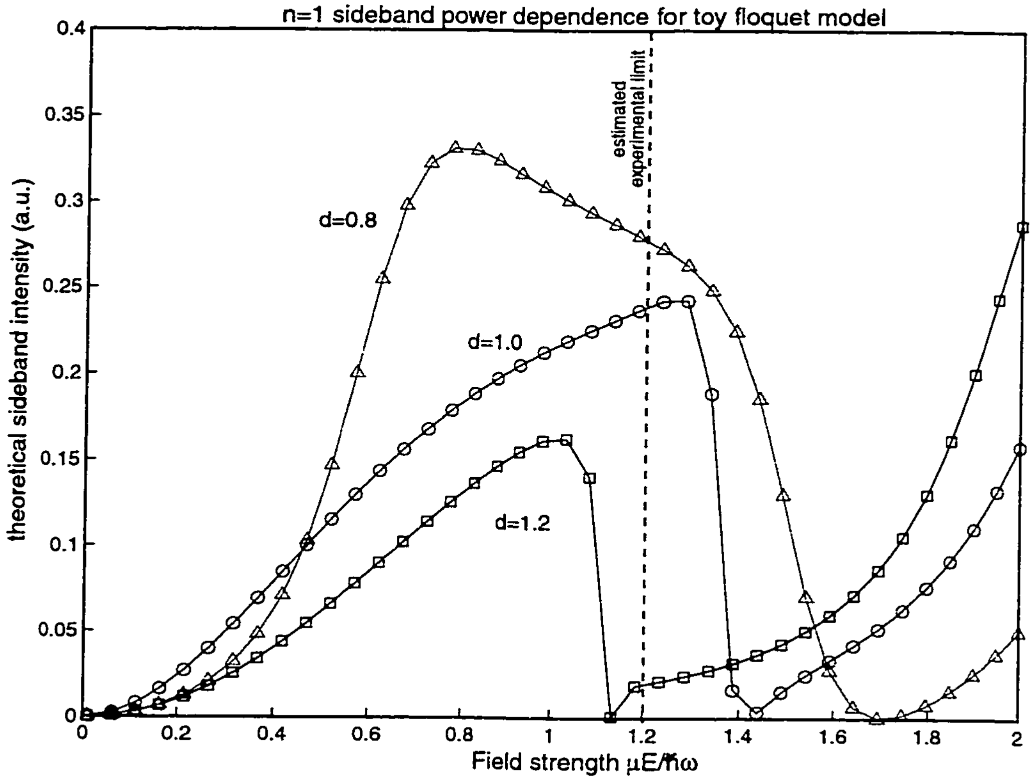

Figure 5.5: Sidebands calculated by evaluating (5.2.15) at various detuning parameters $d = \frac{E2-E1}{\hbar\omega} = 0.8, 1.0, 1.2$. Compare the results of this simplistic toy 3-level model with the experimental results of Fig. 5.4a.

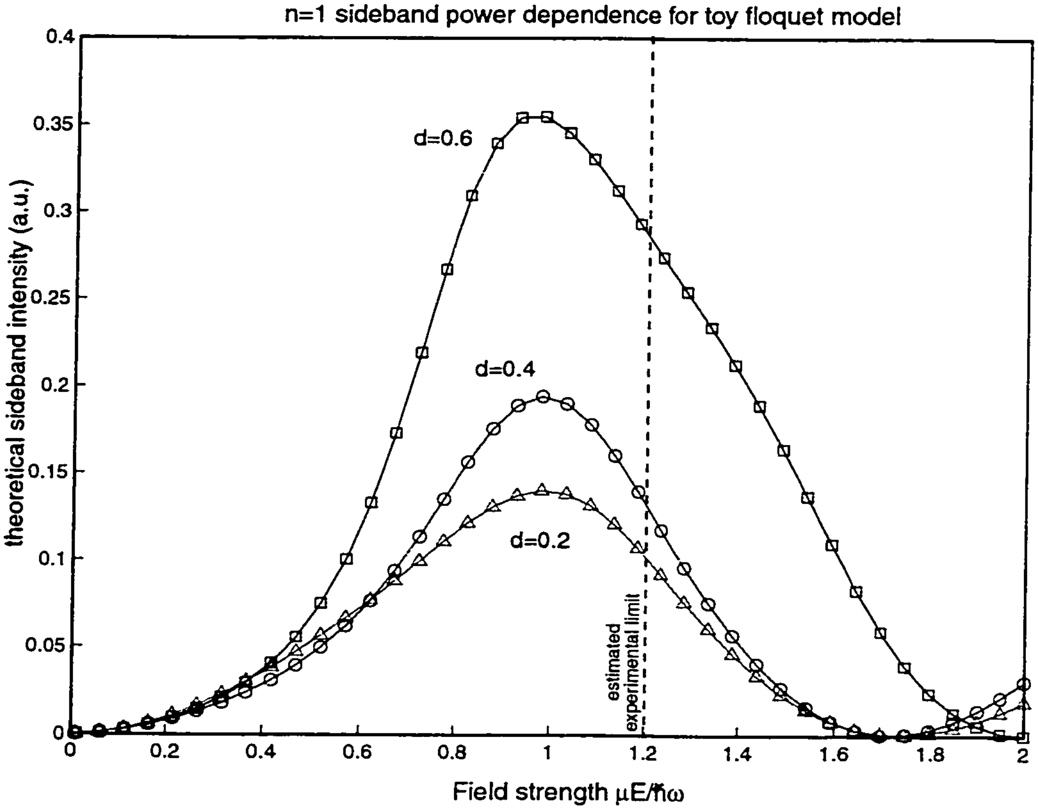

Figure 5.6: Sidebands calculated by evaluating (5.2.15) at various detuning parameters $d = \frac{E2-E1}{\hbar\omega} = 0.2, 0.4, 0.6$. Compare the results of this simplistic toy 3-level model with the experimental results of Fig. 5.4b.

small mesa via an antenna. Unfortunately there is a tradeoff between THz field strength and NIR signal, as the smaller the device, the greater the THz field, and weaker the NIR signal. For the size mesas that would improve field strength, the sideband signal was to weak to provide useful results.

It is dubious that a 3-state simplification is entirely valid because there is a spaghetti of other exciton states as well as a continuum that may provide significant off-resonant contributions. But I hope that the point has been made: to understand nonlinear optical behavior in a strong-field regime requires some formalism, such as Floquet theory, to address the role of heavily dressed states.

Chapter 6

Conclusion

6.1 Summary

In this dissertation I described experiments and theory of the exciton states of a tilted asymmetric double-quantum well. The states involve a rich interplay of quantum-confinement, tunnelling, and Coulomb-binding all occuring at energy scales of around 10 meV. I then drove these exciton states by terahertz laser fields to excite *excitonic* intersubband transitions. This process modulated a weak NIR probe beam via optical nonlinearities at terahertz frequencies, generating terahertz optical sidebands on the NIR probe. The result was a unique nonlinear spectroscopic study of excitons and their subband states and coupling strengths. Finally, I studied the effects of a very strong THz field on the NIR modulation efficiency, and related it to the dressing of excitons by the oscillating THz field.

6.2 Technological impact, future directions

6.2.1 Wavelength division multiplexing

As I mentioned earlier in the introduction, all-optical wavelength switching technologies may potentially benefit from studying techniques of generating terahertz optical sidebands on a NIR carrier. While maximal modulation efficiency was not the main goal of my devices, they were a useful testbed for examining the potential benefits and limitations of exploiting the large optical nonlinearities in asymmetric double-quantum wells for photonic applications.

However, the modulation depth is small ($\approx 10^{-4}$) because the active region is very thin. This could be dealt with by copropagating the THz and NIR beams in a ridge waveguide structure. For switching applications a weak sideband is not inherently bad because the signal contained in the sideband could easily be amplified in a later stage.

6.2.2 Terahertz optical parametric oscillator

A tantalizing potential application comes from the $n = -1$ sideband. This is a difference-frequency mixing process, which means that a NIR photon is converted to a THz photon. In otherwords, during a resonance condition for the $n = -1$ sideband the THz field experiences *gain* . Within a high-Q THz cavity, a $n = -1$ sideband could be used as a THz optical parametric oscillator with a NIR pump. The sideband would merely be the discarded idler beam. Currently there are efforts underway to fabricate THz photonic band-gap cavities, which if integrated with THz electro-optic effects could prove very interesting indeed.

6.2.3 Strong-field limits to THz lasers

Strong-field effects, while fascinating from a physics perspective, are basically a hinderance from a technological standpoint. Of course, experimentally to achieve a such intense fields I focused down a kilowatts of THz power from a free-electron laser, an unlikely prospect in any practical device. But such field strengths could still easily be reached inside the cavity of a laser. At optical wavelengths these effects are not a problem but down in the THz the dressing of carefully bandgap-engineered states could place limits on the efficiency of a THz laser.

6.2.4 Quantum chaos

The work I have describe has been in undoped structures. An obvious question arises: what do the sidebands do in doped structures? During some of the experiments I did the sideband measurements while simultaneously irradiating the sample with third color laser (632 nm) to optically "dope" the device. The result was rather startling, as the sideband was completely quenched at very low intensity of the doping laser. Properly pursuing this avenue of measurement required a second tunable laser, and probably would lead to not much. It is likely that this effect is due merely to carrier absorption in the DBR layer, rendering it nonreflective. Such is the usual reality of doing exploratory device physics: trudging through the 80% which is mundane.

Far from being mundane is the exciting possibility of detecting an intersubband polarization in a doped quantum well via the emission of an optical sideband. There have been some predictions[31, 32] of a period-doubling bifurcating route to chaos in the intersubband emission of a THz-driven doped double quantum well similar to the ones studied in this dissertation. This would manifest itself as the emission of sidebands at frequencies $\omega_{NIR} + \frac{1}{2^n}\omega_{THz}$.

Bibliography

[1] B. Mukherjee. *Optical Communication Networks*. McGraw-Hill, N.Y., 1997.

[2] Y. Takahashi, Y. Kato, S. Kano, S. Fukatsu, Y. Shiraki, R. Ito. The effect of electric field on the excitonic states in coupled quantum well structures. *J. App. Phys.*, 76(4):2299, 1994.

[3] F. Capasso. Coupled Quantum Well Semiconductors with Giant Electric Field Tunable Nonlinear Optical Properties in the Infrared. *IEEE J. of Quantum Electronics*, 30(5):1313, 1999.

[4] K.A.H. van Leeuwen, G. v. Oppen, S. Renwick, J.B. Bowlin, P.M. Koch, R.V. Jensen, O. Rath, D. Richards, J.G. Leoplod. Microwave Ionization of Hydrogen Atoms: Experiment versus Classical Dynamics. *Phys. Rev. Lett*, 55(21):2231, 1985.

[5] A. Haffmans, R. Blumel, P.M. Koch, L. Sirko. Prediction of a New Peak in Two-Frequency Microwave Ionization of Excited Hydrogen Atoms. *Phys. Rev. Lett*, 73(2):248, 1994.

[6] K. Johnsen, A.-P. Jauho. Quasienergy Spectroscopy of Excitons. *Phys. Rev. Lett*, 83(6):1207, 1999.

[7] T. Fromherz. Floquet States and intersubband absorption in strongly driven double quantum wells. *Phys. Rev. B*, 56(8):4772, 1997.

[8] G. Bastard. *Wave mechanics applied to semiconductor heterostructures*. Les Editions de Physique, Les Ulis Cedex, France, 1988.

[9] P.Y. Yu, M. Cardona. *Fundamentals of Semiconductors*. Springer, N.Y., 1996.

[10] M. Olszakier, E. Ehrenfreund, E. Cohen, J. Bajaj, G.J. Sullivan. Photoinduced Intersubband Absorption in Undoped Multi-Quantum-Well Structures. *Phys. Rev. Lett*, 62(25):2997, 1989.

[11] R. Duer, I. Shrichman, D. Gershoni, E. Ehrenfreund. Momentum Redistribution Times of Resonantly Photogenerated 2D Excitons. *Phys. Rev. Lett*, 78(20):3919, 1997.

[12] I. Shtrichman, U. Mizrahi, D. Gershoni, E. Ehrenfreund, K.D. Maranowski, A.C. Gossard. Dynamics of carriers in resonantly excited quantum-well lasers studied by intersubband absorption. *App. Phys. Lett.*, 76(21):2988, 2000.

[13] J. Cerne, J. Kono, T. Inoshita, M. Sherwin, M. Sundaram, A.C. Gossard. Near-infrared sideband generation induced by intense far-infrared radiation in GaAs quantum wells. *App. Phys. Lett.*, 70(26):3543, 1997.

[14] J. Cerne, J. Kono, M.S. Sherwin, M. Sundaram, A.C. Gossard, G.E.W. Bauer. Terahertz Dynamics of Excitons in GaAs/AlGaAs Quantum Wells. *Phys. Rev. Lett*, 77(6):1131, 1996.

[15] J. Kono, M.Y. Su, T. Inoshita, T. Noda, M.S. Sherwin, S.J. Allen, H. Sakaki. Resonant Terahertz Optical Sideband Generation from Confined Magnetoexcitons. *Phys. Rev. Lett*, 79(9):1758, 1997.

[16] K.B. Nordstrom, K. Johnsen, S.J. Allen, A.-P. Jauho, B. Birnir, J. Kono, T. Noda, H. Akiyama, H. Sakaki. Excitonic Dynamical Franz-Keldysh Effect. *Phys. Rev. Lett*, 81(2):457, 1998.

[17] C. Phillips, M.Y. Su, M.S. Sherwin, J. Ko, L. Coldren. Generation of First-Order Terahertz Optical Sidebands in Asymmetric Coupled Quantum Wells. *App. Phys. Lett.*, 75(9):2728, 1999.

[18] M.Y. Su, C. Phillips, J. Ko, L. Coldren, M.S. Sherwin. Odd terahertz optical sidebands from asymmetric excitonic intersubband excitation. *Physica B*, 272:438, 1999.

[19] Q. Wu, T.D. Hewitt, X.C. Zhang. Two-dimensional electro-optic imaging of terahertz beams. *App. Phys. Lett.*, 69(8):1026, 1996.

[20] J. Heymann. Terahertz optical sidebands from ZnTe. The experiments were recently performed using the FEL and a HeNe.

[21] M. Bayer, V.B. Timofeev, F. Faller, T. Gutbrod, A. Forchel. Direct and indirect in coupled GaAs/AlGaAs double quantum wells separated by AlAs barriers. *Phys. Rev. B*, 54(12):8799, 1996.

[22] L.V. Butov, A. Zrenner, G. Abstreiter, A.B. Petinova, K. Eberl. Direct and indirect magnetoexcitons in symmetric InGaAs/GaAs coupled quantum wells. *Phys. Rev. B*, 52(16):12153, 1995.

[23] J. Soubusta, R. Grill, P. Hlidek, M. Zvara, L. Smrcka, S. Malzer, W. Geselbrecht, G. H. Dohler. Excitonic photoluminescence in symmetric coupled double quatum wells subject to an external electric field. *Phys. Rev. B*, 60(11):7740, 1999.

[24] T. Westgaard, Q.X. Zhao, B.O. Fimland, K. Johannessen, L. Johnsen. Optical properties of excitons in GaAs/AlGaAs symmetric double quantum wells. *Phys. Rev. B*, 45(4):1784, 1992.

[25] V.V. Krivolapchuk, E.S. Moskalenko, A.L. Zhmodikov, T.S. Cheng, C.T. Foxon. Manifestation of collective properties of spatially indirect excitons in GaAs/AlGaAs asymmetric double quantum wells. *Physics of the Solid State*, 41(2):291, 1999.

[26] T. Kamizato, M. Matsuura. Excitons in double quantum wells. *Phys. Rev. B*, 40(12):8378, 1989.

[27] R. Boyd. *Nonlinear optics*. Academic Press, San Diego, 1992.

[28] Neogi et al. Interband Nonlinear Optical Generation in Presence of Intersubband Light in Asymmetric Quantum Wells. *IEEE J. of Quantum Electronics*, 32(4):701, 1996.

[29] J.N. Heyman, K. Craig, B. Galdrikian, M.S. Sherwin, K. Campan, P.F. Hopkins, S. Fafard, A.C. Gossard. Resonant Harmonic Generation and Dynamic Screening in a Double Quantum Well. *Phys. Rev. Lett*, 72(14):2183, 1997.

[30] J.H. Shirley. Solution of the Shrodinger Equation for a Hamiltonian Periodic in Time. *Phys. Rev.*, 138:979, 1965.

[31] A.A. Batista, B. Birnir, M.S. Sherwin. Subharmonic generation in a driven asymmetric quantum well. *Phys. Rev. B*, 61(22):15108, 2000.

[32] B. Galdrikian, B. Birnir. Period doubling and strange atrractors in quantum wells. *Phys. Rev. Lett*, 76(18):3308, 1996.

Appendix A

Processing

The following is a recipe I developed for processing the antenna-coupled device depicted in Fig 2.3. The waveguide-coupled device process is nearly identical except it has no top leaf metallization and involves an additional cleave procedure, which I will describe.

A.1 Photolithography

The *bilayer photoresist* recipe is: spin OCG825 at 4000 rpm 45 s. softbake 95C 60s. flood expose 3s. spin AZ4110 at 4000 rpm. softbake 95C 60s. expose 8s. develop 1:4 AZ400K:H2O 60s.

The *regular photoresist* recipe is to skip the OCG825 step.

For small features use the right-side Suss mask aligner, and bring your own high-power microscope objective. Use the alignment marks on the mask and progressively zoom in. The final alignment steps align with the features.

A.2 Cleaning

The *full cleaning* recipe is: 60s hot acetone, 60s hot methanol, 60s hot isopropanol, 60s hot DI, 10s DI rinse under faucet.

The *quick cleaning* recipe is: 60s hot acetone, 60s hot isopropanol, 10s DI rinse under faucet.

A.3 Cleavage

Cleave 5x5 mm chips. (5x8 for waveguide). One will be sacrificial. Full clean if necessary.

A.4 Frontgate metallization

Bilayer resist, photolith. E-beam#3, evaporate 50/350/850/200/2000 ÅNi/Ge/Au/Pt/Au. Liftoff in acetone. Full clean. Anneal in RTA 410C 30s with 1 atm forming gas. Test for ohmicity.

A.5 Mesa etch

Regular resist, photolith. Make sure mesa overlaps with frontgate.

Clean RIE#5 chamber, 10min 30 mT 30 sccm Cl_2 300 W.

O2 descum 15", 300mT 100W. Load sacrificial etch calibration chip RIE#5. Dry etch 0.7/10.0 sccm Cl2/SiCl4 3:15. unload directly into DI. Dektak, determine etch rate to be between 300 and 1000 Åof the backgate quantum well.

Clean RIE#5 chamber. Load remaining chips. While pumping down, prepare wet etch: 100/2/10 DI/H2PO3/H2O2 stir 240 rpm. Dry etch. Unload into DI. Blow dry. Wet etch dip 3s to remove passivation layer. Quick clean. Dektak to make sure you didn't punch through backgate.

A.6 Backgate metallization

Bilayer resist, photolith. Make sure backgate butts up against mesa (unecessary for waveguide device.) prepare 1:5 HCl/DI solution. 5 s dip to remove oxide, immediately load E-beam#3 and pump down. angle evaporate using angle jig I made to shadow mask a gap between the mesa and the backgate. (angle unnecessary for waveguide device.) evaporate 50/350/850/200/2000 ÅNi/Ge/Au/Pt/Au. liftoff in acetone. full clean. anneal in RTA 410C 30s with 1 atm forming gas. Test for ohmicity.

(After this step for the waveguide device you may skip to the AR coating deposition.)

A.7 Isolation etch

Regular resist, photolith. O2 descum 15". clean RIE#5 chamber, 10min 30 mT 10 sccm Cl2. RIE#5, 0.7/10 $Cl_2/SiCl_4$ for 1 min to punch through backgate. Unload into DI, Blow dry. Quick clean.

A.8 Antenna metallization

Bilayer resist, photolith. Ebeam#3, Ti/Au 50/10000. liftoff in acetone. full clean.

A.9 AR coating

Bilayer resist, photolith. crush SrF2 into a closed thermal evaporator boat. evaporate $\lambda/4$ coating. liftoff in acetone. full clean.

A.10 Cleaving waveguide

Cleaving 1mm×8mm strips on 500-μm thick wafers is somewhat tricky. Here is my technique: Under a stereo microscope, place the chip on graph paper. carefully carve out a nice nick on the front side 1 mm from edge. Flip over the chip. Using a glass stirring rod, place the rod along the desired cleave. The glass rod will magnify the graph paper to make precise alignment easy. press evenly on the glass rod, and the cleave should be clean. Yield is about 80% with practice.

A.11 Cleaving sapphire

Under the stereo microscope scribe a deep scratch the full length of the cleave with a burly fiber-optic scribe. Flip over and press hard. Yield is about 25% but sapphire is aplenty. The sapphire should be 1mm×4mm. Be sure to cleave the right direction, so the slow-axis is along the direction of the THz propagation.

A.12 Forming sapphire-semiconductor waveguide

This must be done in the class 100 cleanroom. Do a full clean of both the chips and the sapphire. Blow dry. GE varnish the chip to the sample mount. With tweezers mount the sapphire onto the chip with the berrylium copper clip, and screw it down hard. A head-mounted jeweler's magnifier is helpful. You will need many iterations to get it lined up right.

A.13 Bonding

Scrape indium clean with a scalpel. Under a stereo microscope, using sharp tweezers and a scalpel, cut a tiny blob if indium and grab with tweezers. Using the tweezers and a dental tool, press the indium onto the gold pad. Using a dull pair of tweezers and a very sharp wire cutter, cut a long length of 10 μm gold wire. While holding the far end with tweezers press the wire into the indium pad. Trim. Repeat for other side.

Appendix B

Experimental

This appendix contains some experimental details to help workers who wish to repeat the experiments.

B.1 Alignment procedure

In order to properly align the large THz focus using off-axis parabolics to the focus of a second and third laser spot and then align it to a device, you have to be able to independently move the THz focus, NIR focus, and device. Also you need to be able to move the cryostat completely out of the focus region in order to properly focus and align the two laser beams using Foucault's razor-blade technique of evaluating focus and aberration.

B.1.1 Aligning the alignment laser

The FEL cavity has a visible alignment laser beam expanded and aligned with the cavity. There are several alignment marks inside the beamline in the accelerator room to align the visible laser with the 60 μm hole which couples out the THz

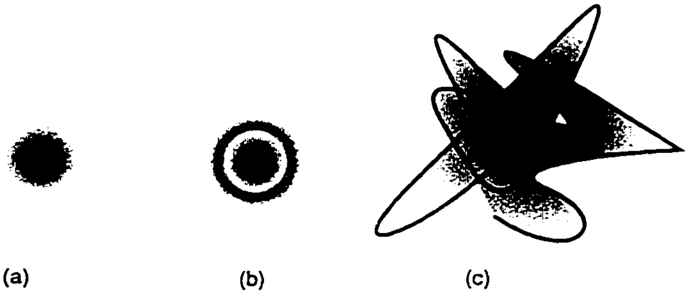

Figure B.1: (a) Good spot at focus. (b) Best acheivable spot if beam is clipped. (c) If the spot looks like a Kandinsky then you need to adjust for astigmatism.

radiation. This process requires two people because the mirrors are far from the alignment marks. After entering the user lab's optical transport the optical table is more than 15 m away. By the time the visible reaches the table it has travelled a lever arm of over 30 m. I have found that the visible alignment laser will easily focus to within ten microns of the actual THz focus.

B.1.2 Off-axis parabolic astigmatism

Avoiding clipping the large 10 cm beam by whatever flat mirrors are used to steer the THz beam. This requires flat mirrors at least 15 cm wide.

Move the cryostat out of the way of the focus.

The first step is to do the gross adjustment for the astigmatism of the off-axis parabola. This is done by tweaking the angles of both the parabolic mirror mount and the flat mirror just before the parabolic until near the focus the spot is circular as seen through a magnifying glass (Fig. B.1). This is a difficult and time-consuming process. For smaller parabolics it is inevitable to clip the beam. Then the focus will not be Gaussian, rather it will have a radial profile like a sinh function, with a central spot and a ring around it. Make sure that both are symmetric.

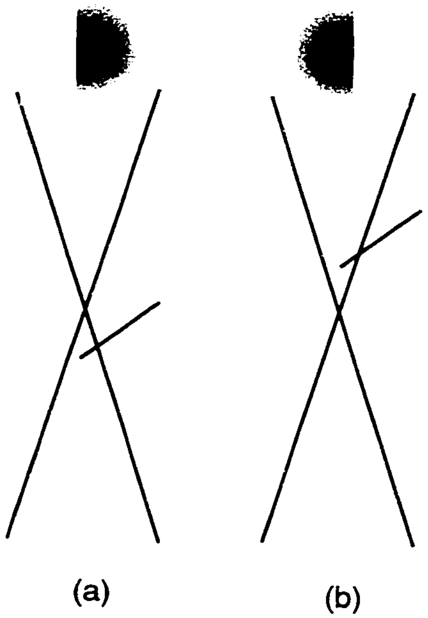

Figure B.2: Foucault's method for finding the focus. Razor blade in front (rear) of focus clips left (right) side of far-field projection.

B.1.3 Finding the THz focus

The focus is found using a variant on Foucault's razor-blade technique of finding the focus and evaluating aberations by positioning on an xy-stage a razor-blade diagonal to both the THz and NIR beams. Position a screen to view the far field pattern well past the focus. Repeatedly push the razor-blade in and out of the way of the beam. If the razor blade is closer to (farther from) the parabolic than the focus, then the left (right) side of the far-field projection will dissappear (see Fig. B.2). Within the waist the entire far-field pattern will morph away all at once. Find the center of the waist with the razor blade. Take note of the micrometer postions.

B.1.4 Align the NIR focus

Of course, it is assumed that the laser and AO modulator have all been aligned at this point.

Adjust the NIR beam to a more visible wavelength, say 13000 cm^{-1}, and attenuate to 1 mW. The focusing lens should be an achromatic doublet to minimize chromatic and spherical aberrations. It should be large as it is used for both focusing and collection. It should be mounted on a xyz stage, which is mounted on a removable kinematic mount.

Remove the lens, and move the razor-blade away. The elevation of the NIR needs to be brought level to the same rough elevation as the focus of the THz. After vertical levelling, position the razor blade back to the focus position. Steer the unfocused, collimated NIR beam to clip the edge of the razor-blade. Two steering mirrors and ruler or marked cardboard works well.

Put the lens back into place. Rough align it so that the beam passes through the middle of the lens vertically, and off center by around a cm horizontally. Rotate the xyz stage so that one axis is parallel to the NIR beam. Now do the Foucault test with the NIR beam, except don't move the razor blade, move the lens so that the NIR focus moves in and out of the way of the razor. This will align the focus of the NIR with the focus of the THz on all the horizontal axes.

Finally, using a strip of index card, place it along the NIR beam as it focuses, so that you see a stripe of light on the card. Looking through a magnifying glass, align the vertical position of the NIR stripe with the THz focus.

B.1.5 Aligning the waveguide

If the waveguide has sapphire, it is easy to align, since the sapphire will glow with the color of the alignment laser. Also, the sample will just be parallel to the

THz beam.

If the waveguide does not have sapphire, then the device needs to be positioned at an angle so that part of the field is incident on the front surface of the sample.

The final alignment must be done by rastering the crysotat translation and rotation stage axes to find the sideband. Since even at the peak sideband intensity when well-aligned and on resonance the single-shot signal-to-noise ratio is only 100 or so, the initial stages of signal hunting and peaking involve averaging many FEL pulses for each micrometer position.

B.2 Dispersion, and detection, electronics

The workhorse detector is a side-on multialkali PMT (Hamamatsu R6356) run at room temperature. The dynode chain is biased at 1000V by a SRS 325 through a balun. The signal is a voltage on a 1 kOhm shunt resistor, which is sent through a balun to an Stanford SR560 voltage preamplifier where it is inverted and multiplied by 10 in low-noise mode. Then the signal goes to an HP digitizing scope for capture.

The PMT is mounted on a 0.85m SPEX double monochrometer with two 11 cm 1800g/mm gratings. Rejection of the laser line at the sideband wavelength is over 10^{1}0. High resolution is more of a nuisance than help, so for sideband scans all four slits are opened to 1 mm.

The PL spectra are taken with a TE-cooled intensified CCD camera (Princeton Instruments ST135). It is mounted on a 0.35m Acton monochrometer with a 5cm 1200g/mm grating.

The reflection data are taken with a large-area 10-mm square Si photodiode at room temperature in photoconductive mode with a 10 kOhm shunt resistor. An identical photodiode is used to for the error signal in a PID feedback loop used to control the Ti:S intensity with a gradient neutral density filter on a motorized translation stage.

The collected light is sent to dispersive instruments by SMA connectorized 0.22 NA optical fiber with 365 μm thick cores (ThorLabs FG-365-LER).

The THz reference detector is a 5mm diameter $LiTaO_3$ pyroelectric detector with charge-sensitive preamp (Molectron P1-35) with 3 MHz of unity-gain bandwidth.

B.2.1 Grounding

The experiment is necessarily spread out over two optical tables, with dispersive instruments, detectors, and scope on one table, and lasers, cryostat and biasing electronics on another. This with FEL trigger signals and computer controls from across the lab, grounding and noise pickup up to a few MHz are always issues. All instruments on individual tables have their third prongs disconnected, and their cases connected by grounding straps to a single ground point in a star topology. Trigger lines and GPIB cables that run between tables are opto-isolated. The only signal line that runs from the main optical table to the dispersion table is the pyro-electric detector, which is isolated from the laser table and derives its ground from the dispersive table.